COLLECTIVE DYNAMICS IN FLOWING SUSPENSIONS OF SWIMMING MICRO-ORGANISMS

BY

AMIR ALIZADEH PAHLAVAN

THESIS

Submitted in partial fulfillment of the requirements
for the degree of Master of Science in Theoretical and Applied Mechanics
in the Graduate College of the
University of Illinois at Urbana-Champaign, 2010

Urbana, Illinois

Adviser:

Assistant Professor David Saintillan

Abstract

Micro-organisms first appeared on earth about 3.8 billion years ago and can be found almost everywhere now. In terms of number and biomass, they in fact constitute the majority of terrestrial life and despite their tiny size play a vital role in a wide variety of phenomena. Although there has been a long history of studying characteristics of individual bacteria, their large-scale collective motions have just recently received attention from scientists. It has been reported that, as concentration of such systems increases beyond a threshold, complex correlated dynamics on length scales much larger than the size of individual bacteria can be observed. It has recently been suggested that these correlated motions can be explained in terms of hydrodynamic interactions between particles. Although different types of swimmers use a wide variety of different mechanisms, universal features exist in their associated hydrodynamics. In particular, as they swim they exert a force dipole on the fluid; this force induces a disturbance flow in the fluid, the characteristics of which are universal in the far field. This universality allows the development of mean-field theories to describe such suspensions over length scales much larger than the particle dimensions.

In this work, we make use of a recently developed kinetic model to investigate pattern formation in a dilute suspension of swimming micro-organisms in the presence of an external shear flow. Doing so allows us to simulate more realistic situations where ambient flow is present, as in oceans where motility could influence bacterial ecology and the role of bacteria in oceanic biogeochemistry. Moreover, we can investigate their rheological properties, which have recently been reported to show unexpected behaviors.

In the first part of this work, we investigate the effect of shear flow on the flow structures using a linear stability analysis and three-dimensional numerical simulations. The external shear flow is found to dampen the instabilities that occur in these suspensions by controlling the orientation of the particles. We demonstrate that the rate of damping is direction-dependent: it is fastest in the flow direction, but slowest the direction perpendicular to the shear plane. Consequently, transitions from three- to two- to one-dimensional instabilities are observed to occur, as shear rate increases, and above a certain shear rate the instabilities disappear altogether. The density patterns and flow structures that arise at long times in the suspensions are also analyzed from the numerical simulations using standard techniques from the literature

on turbulent flows. The imposed shear flow is found to have an effect on both density patterns and flow structures, which typically align with the extensional axis of the external flow. The disturbance flows in the simulations are shown to exhibit similarities with turbulent flows, and in particular two of the seemingly universal characteristics of turbulent flows also occur, namely: (i) the alignment of the vorticity vector with the intermediate strain-rate eigenvector, and (ii) the bias of Q–R plots toward second and fourth quadrants, corresponding to stable focus/stretching and unstable node/saddle/saddle topologies, respectively. However, the flows described herein also differ significantly from turbulent flows owing to the strong predominance of large scales, as exemplified by the very rapid decay of the kinetic energy spectrum, an effect further enhanced after the transitions to two- and one-dimensional instabilities.

Then, we move on to investigate the effect of hydrodynamic interactions and flow instabilities on the rheology of dilute flowing suspensions of swimming micro-organisms. The effect of external shear on the orientation distribution and the relative alignment of flow rheological properties is investigated. It is found that regions of negative particle viscosity are aligned with more concentrated areas of the flow; this alignment suggests that, as particles form clusters, it becomes easier for them to swim. This phenomenon could be the origin of correlated motions observed in experiments and simulations. The particle viscosity is also found to be slightly aligned with the director field and vorticity axis; this alignment becomes more pronounced as the flow becomes 2D. Moreover, we investigate time evolution of the rheological properties and the effect of shear on them and compare them with the results obtained from single-active-particle rheology. The spatially-averaged properties oscillate in time and these oscillations become damped with the shear. It appears that the effect of shear on the rheological properties is not expected a priori; the properties almost do not vary with shear as long as the flow is 3D, but as the flow becomes 2D, they start to approach the predictions of single self-propelled particle rheology and they match very well in the limit of high shear rates, where all the instabilities are damped by the external shear and the flow becomes spatially uniform.

To my mom, dad, brother and Setareh

Acknowledgments

Although my sincere gratitude to the people who have helped me throughout all these years to try to become a better individual cannot fit into the small space here, I would like to thank some of them.

First, I wish to thank my adviser, Prof. David Saintillan. I consider myself very lucky to have the chance to work with him. Professor Saintillan is a very sharp individual from whom I learnt many things. I would like to thank him for his patience and help through hours of fruitful discussions.

I would like to acknowledge the National Science Foundation for being the source of financial support of this work, and the National Center for Supercomputing Applications for providing part of computational resources for this work.

I am also thankful to my friends at UIUC. I remember the first day I came here, I didn't know a single individual and now I have nearly hundred friends who have made my stay more enjoyable and helped me feel like home while being thousands of miles far away from it.

Next, I would like to thank my mother Zahra, father Mazaher, and brother Hamid for their endless love, support and encouragement and providing me with all I need to achieve my goals. They get most, if not all, of the credit for everything I have achieved so far and I owe everything to them.

And finally, I would like to thank Setareh for believing in me. Her care, support and love has made everything much easier for me throughout these past years. She has inspired me everyday and has given me the motivation I need to try to be better.

Table of Contents

List of Tables . . . . . **vii**

List of Figures . . . . . **viii**

Chapter 1 Introduction **1**

Chapter 2 Flow Structures **8**
2.1 Introduction 8
2.2 Kinetic Theory 9
2.3 Linear Stability Analysis 13
2.4 Simulation Techniques 18
2.5 Numerical Simulation Results 20
2.5.1 Instabilities in the density field 20
2.5.2 Vortical structures 22
2.5.3 Q–R Plots 25
2.5.4 Joint probability distribution functions (JPDFs) 28
2.5.5 Alignment with the strain-rate eigenvectors 30
2.5.6 Autocorrelation functions 34
2.5.7 Energy spectrum E_k 38
2.5.8 Flow evolution in time 39
2.5.9 Statistics 46
2.5.10 Alignment of the concentration and the concentration weighted director fields 50
2.6 Concluding Remarks 54

Chapter 3 Rheology **55**
3.1 Introduction 55
3.2 Theory 57
3.3 Results 58
3.4 Concluding Remarks 67

Chapter 4 Conclusions **69**

Appendix A Spherical Harmonics Identities **71**

References **73**

List of Tables

A.1 Spherical harmonic identities used in reducing the multipolar integrands to simple products of harmonics 71

List of Figures

1.1 The flow field created by pusher and puller particles: (a) pusher particles induce a flow field directed away along their swimming axis and a flow field towards the cell along their side, (b) puller particles induce a flow opposite to that of pusher particles, i.e. a flow towards the cell along their swimming axis and away from the cell along their sides, (c) two pusher particles tend to align with each other and swim side by side, and (d) two puller particles tend to swim away from each other. Red solid arrows represent the local forcing from the cell on the surrounding fluid and the blue dotted arrows represent the induced flow direction. (Picture courtesy of Lauga and Powers [1]) 3

2.1 The coordinate system used in the work. The particle director $\mathbf{p}$ indicates the orientation of the particles and direction of swimming relative to the external flow. 11
2.2 Effect of shear rate on the (a) real part, and (b) imaginary part of growth rate σ. $S = 0$: black solid line, $S = 0.1$: blue dashed line, $S = 0.2$: red dash dotted line, and $S = 0.3$: green dash dot dotted line. 16
2.3 Base state distribution functions for $S = 0.1$, $D = 0.01$ and (a) $d = 0.001$, and (b) $d = 0.01$. . 17
2.4 Most unstable eigen modes for the distribution function $\tilde{\Psi}(\mathbf{p})$ for $S = 0$, and wave vectors: (a) $\mathbf{k} = 0$, (b) $\mathbf{k} = 0.1$, and (c) $\mathbf{k} = 0.2$. 17
2.5 Most unstable eigen modes for the distribution function $\tilde{\Psi}(\mathbf{p})$ for $S = 0.1$, and wave vectors: (a) $\mathbf{k} = 0$, (b) $\mathbf{k} = 0.1$, and (c) $\mathbf{k} = 0.2$. 18
2.6 Effect of rotational diffusion d on the real part of σ for (a) $S = 0$, and (b) $S = 0.1$. $d = 0.001$: solid line, $d = 0.01$: dashed line. 18
2.7 The computational grid deforms with the imposed shear flow to allow using the periodic boundary condition. Remeshing is done at regular intervals when $S \times t = n(n+1)/2$ and the grid becomes orthogonal whenever $S \times t = 2n$, where n is a positive integer. 19
2.8 Concentration field isosurfaces for different shear rates: (a) $S = 0$, $c = 1.5$, (b) $S = 0.1$, $c = 1.2$, (c) $S = 0.14$, $c = 1.1$, (d) $S = 0.2$, $c = 1$. 21
2.9 Vortex structures for different shear rates: (a) $S = 0$, $Q = 0.015$, (b) $S = 0.1$, $Q = 0.0075$, and (c) $S = 0.14$, $Q = 0.001$. 23
2.10 Three-dimensional topologies in the Q–R plane. $P = 0$ for incompressible flows. (Picture courtesy of Soria et al. [2]) 25
2.11 Q–R plots for different shear rates: (a) $S = 0$, and (b) $S = 0.1$. 26
2.12 Q_s–R_s plots for different shear rates: (a) $S = 0$, and (b) $S = 0.1$. 27
2.13 Q_s–Q_w plots for different shear rates: (a) $S = 0$, and (b) $S = 0.1$. 28
2.14 Joint probability distribution function of the concentration gradient angles for different shear rates: (a) $S = 0$, (b) $S = 0.1$, and (c) $S = 0.14$. 28
2.15 Joint probability probability function of vorticity vector angles for different shear rates: (a) $S = 0$, (b) $S = 0.1$, and (c) $S = 0.14$. 29
2.16 Joint probability distribution function of the director field angles for different shear rates: (a) $S = 0$, (b) $S = 0.1$, and (c) $S = 0.14$. 30
2.17 Alignment of the concentration gradient with the strain-rate eigenvectors for different shear rates: (a) $S = 0$, (b) $S = 0.1$, (c) $S = 0.14$, (d) $S = 0.2$. 31

2.18 Alignment of vorticity vector with the strain-rate eigenvectors for different shear rates: (a) $S = 0$, (b) $S = 0.1$, (c) $S = 0.14$. 32
2.19 Alignment of the director field with the strain-rate eigenvectors for different shear rates: (a) $S = 0$, (b) $S = 0.1$, (c) $S = 0.14$, (d) $S = 0.2$. 33
2.20 Alignment of the director field with (a) concentration gradient, and (b), (c) vorticity vector. $S = 0$: solid line, $S = 0.1$: dashed line , and $S = 0.14$: dash dotted line. 34
2.21 Concentration field autocorrelation function in x-y plane for different shear rates: (a) $S = 0$, (b) $S = 0.1$, and (c) $S = 0.14$. 35
2.22 Velocity field autocorrelation function in x-y plane for different shear rates: (a) $S = 0$, (b) $S = 0.1$, and (c) $S = 0.14$. 35
2.23 Director field autocorrelation function in x-y plane for different shear rates: (a) $S = 0$, (b) $S = 0.1$, and (c) $S = 0.14$. 36
2.24 Concentration field autocorrelation function in y-z plane for different shear rates: (a) $S = 0$, (b) $S = 0.1$, and (c) $S = 0.14$. 36
2.25 Velocity field autocorrelation function in y-z plane for different shear rates: (a) $S = 0$, (b) $S = 0.1$, and (c) $S = 0.14$. 37
2.26 Director field autocorrelation function in y-z plane for different shear rates: (a) $S = 0$, (b) $S = 0.1$, and (c) $S = 0.14$. 37
2.27 Energy spectrum for different shear rates. (a) total energy; from top to bottom: $S = 0$, $S = 0.05$(included just in the total energy), $S = 0.1$, $S = 0.14$. and (b) one-dimensional spectrum; from top to bottom: $S = 0$ (black color), $S = 0.1$ (blue color), $S = 0.14$ (red color). Solid line: E_{kx}, dashed line: E_{ky}, dash-dotted line: E_{kz}. 38
2.28 Spatially-averaged contraction for different shear rates. Solid line: $S = 0$, long-dashed line: $S = 0.1$, dash-dotted line: $S = 0.14$, dash-dot-dotted line: $S = 0.2$, dashed line: $S = 0.3$. . . . 39
2.29 Active input power for different shear rates. Solid line: $S = 0$, long-dashed line: $S = 0.1$, dash-dotted line: $S = 0.14$, dash-dot-dotted line: $S = 0.2$, dashed line: $S = 0.3$. 40
2.30 System entropy for different shear rates. Solid line: $S = 0$, long-dashed line: $S = 0.05$, dash-dotted line: $S = 0.1$, dash-dot-dotted line: $S = 0.14$, dashed line: $S = 0.5$. 41
2.31 Eigenvalues of strain-rate tensor for different shear rates. Solid line: $S = 0$, long-dashed line: $S = 0.1$, dash-dotted line: $S = 0.14$, dash-dot-dotted line: $S = 0.2$, dashed line: $S = 0.3$. . . . 42
2.32 (a) Swirling strength: λ_{ci}, (b) orbital compactness: $\lambda_{cr}/\lambda_{ci}$, and (c) stretching/compression strength: λ_r, for different shear rates. Solid line: $S = 0$, dashed line: $S = 0.1$, dash-dotted line: $S = 0.14$, dash-dot-dotted line: $S = 0.2$. 43
2.33 1D Correlation length of the concentration field, (a) L_x, and (b) L_z; for $S = 0$: red line, $S = 0.1$: green line, $S = 0.14$: blue line. 45
2.34 Temporal autocorrelation function for the (a) concentration field, (b) velocity field, and (c) director field. Black line: $S = 0$, red line: $S = 0.1$, and blue line: $S = 0.14$. 45
2.35 Probability distribution function of velocity components. Solid line: $S = 0$, dashed line: $S = 0.1$, dash-dotted line: $S = 0.14$. 47
2.36 Probability distribution function of velocity components for (a) $S = 0$, (b) $S = 0.1$, and (c) $S = 0.14$. Solid line: u_x, dashed line: u_y, dash-dotted line: u_z. 47
2.37 Probability distribution function of the concentration gradient components. Solid line: $S = 0$, dashed line: $S = 0.1$, dash-dotted line: $S = 0.14$. 48
2.38 Probability distribution function of the concentration gradient components for (a) $S = 0$, (b) $S = 0.1$, and (c) $S = 0.14$. Solid line: c_x, dashed line: c_y, dash-dotted line: c_z. 49
2.39 Probability distribution function of alignment of the concentration gradient field with gradient of divergence of the concentration weighted director field. Solid line: $S = 0$, dashed line: $S = 0.1$, dash-dotted line: $S = 0.14$. 50
2.40 Slices of the concentration field in different planes for $S = 0$, (a) x-y, (b) x_z, and (c) y-z. . . . 51
2.41 Slices of divergence of the concentration weighted director field in different planes for $S = 0$, (a) x-y, (b) x_z, and (c) y-z. 51
2.42 Slices of the concentration field in different planes for $S = 0.1$, (a) x-y, (b) x-z, and (c) y-z. . 52

2.43 Slices of the divergence of the concentration weighted director field in different planes for $S = 0.1$, (a) x-y, (b) x-z, and (c) y-z. 52
2.44 Slices of (a) concentration field and (b) divergence of the concentration weighted director field, in y-z plane for $S = 0.14$ 53
2.45 Correlation of the concentration weighted director field and the concentration field. Black line: $S = 0$, red line: $S = 0.1$, blue line: $S = 0.14$. 53

3.1 The particle viscosity η_p isosurfaces for different shear rates: a) $S = 0$, $\eta_p = -3.5$ b) $S = 0.1$, $\eta_p = -2.5$ c) $S = 0.14$, $\eta_p = -1$ d) $S = 0.2$, $\eta_p = -0.65$ 59
3.2 Joint probability distribution function of particle viscosity gradient ($\nabla\eta_p$) angles for different shear rates: (a) $S = 0$, (b) $S = 0.1$, and (c) $S = 0.14$ 60
3.3 x-y plane slices at mid z and $t = 440$ for $S = 0.1$ corresponding to (a) particle viscosity, (b) concentration, (c) velocity vectors over contours of vorticity magnitude, and (d) director field vectors. 61
3.4 y-z plane slices at mid x and $t = 750$ for $S = 0.14$ corresponding to (a) particle viscosity, (b) concentration, (c) velocity vectors over contours of vorticity magnitude, and (d) director field vectors. 62
3.5 Alignment of particle viscosity gradient ($\nabla\eta_p$) with (a) concentration gradient (∇c), (b) director field, and (c) vorticity field. Solid line: $S = 0.05$, dashed line: $S = 0.1$, and dash-dotted line: $S = 0.14$ 63
3.6 Time evolution of (a) particle viscosity η_p, (b) first normal stress difference ν_p, and (c) second normal stress difference κ_p. Red line: $S = 0.05$, blue line: $S = 0.1$, green line: $S = 0.14$, and black line: $S = 0.2$. 63
3.7 Time evolution of (a) dissipation due to the external flow Φ_f, (b) dissipation due to the Brownian motions Φ_b, and (c) active input power Φ_s. Red line: $S = 0.05$, blue line: $S = 0.1$, green line: $S = 0.14$, and black line: $S = 0.2$. 64
3.8 Shear effect on the (a) particle viscosity η_p, (b) first normal stress difference ν_p, and (c) second normal stress difference κ_p. The bars shown represent standard variation due to averaging. . 65
3.9 Shear effect on the (a) dissipation due to external flow Φ_f, (b) dissipation due to Brownian motions Φ_b, and (c) active input power Φ_s 66

Chapter 1

Introduction

Micro-organisms first appeared on Earth about 3.8 billion years ago and now are everywhere around us. They can be found in oceans, rivers, puddles, droplets, and in almost all biological systems including our own body. Their dynamics affects not only their own life, but also the life of the larger organisms that feed on them, and even the climate [3, 4]. It is estimated that there are approximately 5×10^{30} bacterial cells on Earth; therefore, in terms of both number and mass, the micro-organisms constitute the majority of the life around us [5]. Their size varies between 0.1 μm and 100 μm and their swimming speed does not usually go beyond a few hundreds $\mu\text{m} \cdot \text{s}^{-1}$. As a result, their corresponding Reynolds number is very small, i.e. $\text{Re} = \rho U l/\mu \ll 1$, in which ρ and μ are the fluid density, and viscosity and U and l are flow characteristic velocity and length scales, respectively. Therefore, when analyzing such flows, inertial effects can usually be ignored [6, 7, 8], and as a result, the net force and torque on an individual cell is zero and all the external forces and couples on the cell become transmitted to their surrounding fluid. Perhaps one of the most intriguing features of low-Reynolds-number flows is that the swimming strategies employed by larger organisms, such as fish, birds or insects, that operate at high Reynolds number, are useless for them at very small Reynolds numbers. That is to say, viscous dissipation will not let any attempt to move by conveying momentum to the fluid, to be successful. These effects can further be analyzed considering the Stokes equations of motion, which govern the fluid flow at low Reynolds numbers. The linearity and time independence of the Stokes equations lead to two interesting properties in low-Reynolds-number locomotion [9]. The first one is the *rate independence*, which states that for a swimming organism undergoing surface deformations, the travelled distance does not depend on the rate of surface deformation, but only on the sequence of shapes the body passes through. An interesting consequence of this property is that one can address many aspects of the low-Reynolds-number locomotion using a purely geometrical point of view [10, 11]. The second important property of low-Reynolds-number swimming is the so-called *scallop theorem*, which states that, if the sequence of shapes taken by a swimmer deforming in a fashion periodic in time is the same when viewed after a time-reversal transformation, then the swimmer cannot move on average. It should be noted that this constraint concerns only the sequence of shapes when viewed forward or backward

in time and not the rate of this deformation. The *scallop theorem* strongly constraints the type of low-Reynolds-number locomotion that can be considered effective [1]. More generally, it shows that bodies with just one degree of freedom cannot move on average due to the fact that they can deform just in a reciprocal fashion. However, it should be noted that the presence of non-reciprocal kinematics is a necessary but not sufficient condition for locomotion at low Reynolds numbers. In order to survive in such environments, micro-organisms have evolved their propulsion strategies so that they can successfully overcome and employ drag [1].

Micro-organisms have many different shapes and use a wide variety of diverse swimming mechanisms. They propel themselves through the fluid by changing their body shape in a periodic way and using waving, or rotating their flagella or cilia. Many microscopic swimmers use one or more of the mentioned mechanisms for propulsion. For instance, while sperm of many species propel themselves through whip-like motions of some flexible filaments distributed along their surface, *E. coli* swim by rotating their relatively stiff helix-like appendages that are distributed on their surface [12, 1].

While different swimmers use a wide variety of swimming mechanisms, universal features exist in the associated hydrodynamics. A self-propelled particle exerts a propulsive force $\mathbf{F}_p$ on the surrounding fluid that is balanced by the resistive drag $\mathbf{F}_d$ from the fluid ($\mathbf{F}_d = -\mathbf{F}_p$). Therefore, to the leading order, the particle exerts a force dipole of strength σ_0 on the fluid. The sign of σ_0 depends on the detailed swimming mechanism; it is negative for pushers (such as *E. coli* and *B. subtilis*), which propel by exerting a force near their tail resulting in a negative force dipole on the fluid, while it is positive for pullers (such as *Chlamydomonas Reinhardtii*), which propel themselves using their head, resulting in a positive force dipole. This dipole forcing induces a disturbance flow in the far field, the characteristics of which are universal for a wide variety of particles. As pusher particles swim, they induce a flow field away from their body along the swimming axis while drawing fluid towards their sides. However, pullers draw fluid in along their swimming axis while repelling fluid along their sides (see Figure 1.1 a, b).

Micro-organisms are found usually in semi dilute or concentrated suspensions. A concentrated population of suspended cells can be considered as a nonlinear dynamical system. As such, it is a generator of spatial and temporal patterns that are both fascinating and potentially of great biological importance [4]. Considering the dynamics of two swimmers will help us understand these many body systems better. Assume we have two swimming organisms, cell A and cell B. The flow field created by cell A will in general lead to two types of passive hydrodynamic interactions with its neighbor (cell B). First, cell B will feel the disturbance velocity field created by cell A, and will be carried along by this flow. Moreover, the gradients of this induced disturbance velocity field created by cell A tend to change the orientation of cell B that would as

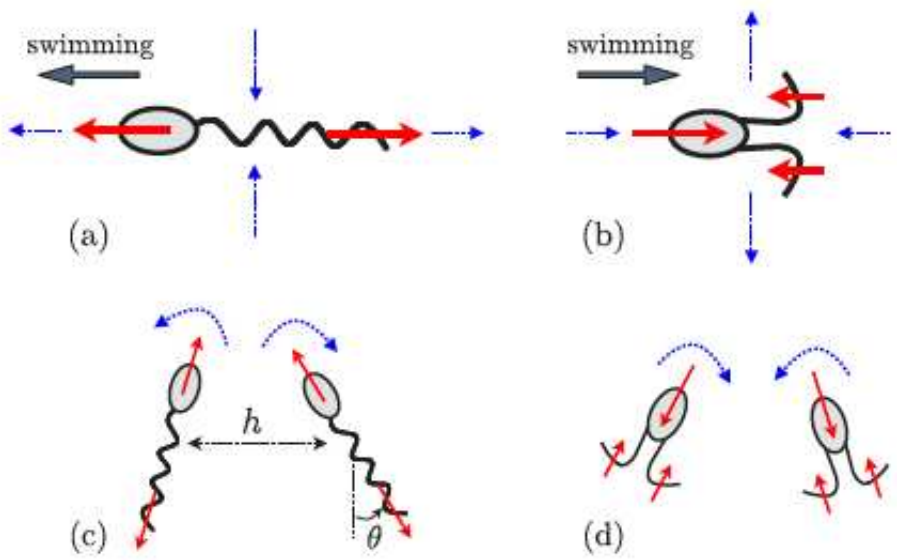

Figure 1.1: The flow field created by pusher and puller particles: (a) pusher particles induce a flow field directed away along their swimming axis and a flow field towards the cell along their side, (b) puller particles induce a flow opposite to that of pusher particles, i.e. a flow towards the cell along their swimming axis and away from the cell along their sides, (c) two pusher particles tend to align with each other and swim side by side, and (d) two puller particles tend to swim away from each other. Red solid arrows represent the local forcing from the cell on the surrounding fluid and the blue dotted arrows represent the induced flow direction. (Picture courtesy of Lauga and Powers [1])

a result, affect its future swimming direction. Therefore, depending on the nature of the induced velocity, for example in suspensions of pusher and puller particles, different rotational behaviors are expected to happen. As two pushers swim towards each other, they tend to become aligned and swim side by side while two pullers tend to swim away as they approach each other, as shown in Figure 1.1 (c, d). Note that the induced disturbance velocity of cell B will affect cell A, in the same way the cell B is affected by the induced flow of cell A. Moreover, as a solid body located in the shear flow, cell B will set up a disturbance flow, which then influences the velocity and orientation of cell A. But this *reflection* is a weaker effect than the direct interaction mentioned above, since it decays faster in space [1]. Overall, the induced translational disturbance velocity decays as $1/r^2$, where r is the distance from the particle's center of mass; however, the induced rotational velocity decays as $1/r^3$. This rapid decline suggests that the effect of detailed cell shape is unimportant in the far-field interactions. Such a property is crucial in the modeling of active suspensions [5].

Interactions between two nearby bacteria have also been explored both experimentally and numerically. Aranson et al. [13] experimentally observed two-cell interactions between *Bacillus subtilis* bacteria in a thin film. They observed that bacteria reoriented during collision and tended to align side-by-side afterwards.

Ramia et al. [14] and Nasseri and Phan-Thien [15] numerically investigated the interactions between bacteria using a boundary-element method. They employed a detailed model of a bacterium as a spherical body with a rotating helical flagellum and found attraction between two bacteria swimming side-by-side, as predicted by a far-field analysis. Pooley et al. [16] used a simple swimmer model consisting of three spheres joined by thin rods that move by shortening and extending the rods in a periodic and time-irreversible fashion. They showed that the interactions between two swimmers may be attractive, repulsive or oscillatory, depending on their relative displacement, orientation and phase. Later, Ishikawa and Pedley [17] used a series of spheres as their bacterial model to investigate near-field interactions. They also made use of boundary-element methods to perform a numerical analysis of the stability of two parallel swimming bacteria. While earlier experimental research based on observations in a thin film and near a wall and also analytical studies using multipoles suggested this state to be stable, Ishikawa and Pedley [17] reported the parallel swimming motion to be unstable. Such contradictory results suggest that the details of the near-field hydrodynamic interactions have an appreciable effect on the simulations and the ad hoc models used suffer from some shortcomings.

Going beyond two particles, it becomes very difficult to imagine how bacteria will interact with each other. Indeed, complex spatiotemporal coherent structures have been observed in concentrated suspensions of micro-organisms. Coherent structures in bacterial suspensions were first reported by Kessler and Wojciechowski [18] and Kessler and Hill [19], followed by Mendelson et al. [20]. They observed large-scale vortical and jet-like motions generated by *B. subtilis* in a thin water film above an agar gel. Later, Dombrowski et al. [21] also reported coherent structures in a concentrated suspension of *B. subtilis*. In a concentrated suspension, a *B. subtilis* cell tends to swim in much the same direction as its neighbors, therefore generating a flow pattern larger than the scale of an individual cell. The concentration dependence of the coherent structure was later reported by Sokolov et al. [22]. These pattern formations play a vital role in the dynamics of such suspensions and have been shown to affect considerably the suspension properties; for instance, they substantially enhance effective diffusion, as shown by Wu and Libchaber [23]. They studied the effect of bacterial motion on the diffusivity of micro-scale polystyrene beads in a free-standing stable two-dimensional soap film seeded with *E. coli* and micro-scale beads. They reported that the particles' diffusivity was enhanced by order of a thousand times greater than Brownian motions.

Beside the experiments, many researchers have also tried to study the correlated motions in concentrated suspensions of bacteria using mathematical models and numerical simulations [5]. These models can be categorized into two major groups: discrete models, in which the motions of individual particles are solved for, and mean-field or continuum models, which are developed mostly for dilute suspensions where particle–particle interactions can be ignored. The studies using the discrete models have involved various levels

of approximation. Detailed boundary-integral methods have been used to investigate the hydrodynamic interactions between nearby particles [24, 25, 26]. However, such simulations are very costly and limited to a small number of particles. Moreover, as mentioned above and also discussed in the recent work of Subramanian and Koch [27], these simulations are very sensitive to the details of the ad hoc models used for near-field hydrodynamic interactions. For instance, Mehandia and Nott [28] found that the formation of clusters can be related to the lubrication interactions. They observed that the velocity distribution of swimmers is very sensitive to the near-field hydrodynamics, and deviates from Gaussian distribution when considering only the far-field hydrodynamics. The numerical simulations of suspensions of spherical squirmers performed by Ishikawa et al. [26] also shows sensitivity to near-field hydrodynamics. The surface-velocity distribution used in their simulations appears to affect their results [24]. In fact, the distribution provides a clustering mechanism due to the induced radial inflow in the vicinity of the particles. As noted by Subramanian and Koch [27], although such model might be though reasonable for specific types of organisms such as *Opalina*, it can not be considered universal by any means. Even for such swimmers, in which the cilia normally beat in a single direction, the choice of surface-velocity distribution of squirmers in the study of Ishikawa et. al. [24] can be questioned. A single signed surface-velocity distribution that can naturally be expected due to the single-direction beating of the cilia, does not generate any force dipoles; as a result, Ishikawa et al. [24] have included an additional contribution that leads to an inverse flow at a critical angle on the surface of the particles. However, the force dipole so obtained cannot be considered physical. Hence, it appears that the nature of the near-field hydrodynamics in such suspensions can affect substantially the collective motions and clustering dynamics, and in the best scenario case can be considered only as an approximation to specific swimmers.

In order to capture the large-scale patterns that occur when many particles interact, simpler models have also been developed based on the universal far-field induced disturbance. Hopkins and Fauci [29] solved the Navier–Stokes equations in the presence of a discrete collection of micro-organisms. They considered these cells as point sources of gravitational force in the fluid equations. Using this model, they could successfully reproduce the experimentally observed bioconvection patterns in suspensions of bottom-heavy swimmers. Hernandez-Ortiz et al. [30] and Underhill et al. [31] simulated the motions of large populations of swimming particles that interact hydrodynamically in confined geometries. Their model consists of two rigidly linked beads that exert a force dipole on the fluid. Based on this model, they were able to simulate fairly large suspensions of interacting swimmers in a parallel plate geometry and were able to capture the qualitative features of experiments on bacterial suspensions. In particular, they observed that beyond a certain particle concentration, correlated motions on the scales much larger than the size of individual particles, start to

appear. They also reported an enhanced diffusion as a result of the motion of the particles. Cisneros et al. [32] also proposed a similar model, in which a cell body is modeled by a sphere and a flagella bundle is modeled by a rod. They numerically investigated hydrodynamic interactions between several swimming particles near a wall. Using slender-body theory, Saintillan and Shelley [33] investigated orientational order in suspensions of self-propelled narrow spheroids. They modeled a bacterium as a slender, narrow spheroid particle, which exerts an axisymmetric tangential shear stress on the fluid over a section of its body, and the no-slip conditions is applied to the rest of its body. The effect of a beating cilia on the surface of a micro-organism may be represented by such a choice of boundary conditions. Similar to the findings of Hernandez-Ortiz et al. [30], Saintillan and Shelley [33] observed large-scale correlated motions regardless of the initial condition—aligned or random isotropic. Particularly, in suspensions of pusher particles, they observed local alignment, strong density fluctuations, and coherent structures. Their numerical simulations verified the earlier findings of Simha and Ramaswamy [34] that the nematic suspensions of swimming particles are unstable at long wavelengths.

To overcome the size limitations of the very expensive particle-based simulations, and in order to be able to describe the observed large-scale motions, mean-field theories are required. Such models have particularly received much attention to describe systems where interactions are purely local, such as in flocking phenomenon [35, 36]. However, in suspensions of swimming micro-organisms, where the interactions are long ranged and cannot be neglected, these models are not useful, unless they become generalized by coupling the evolution equations for the particle configurations to equations for the fluid flow. In the last few years, there have been some efforts in this area. Ramaswamy et al. [34, 35, 37] included the effect of the force dipoles in Navier–Stokes equations, through a coarse-grained active-stress tensor, and coupled it to the dynamical equations of liquid crystals. Using this model, they reported that aligned suspensions of self-propelled particles that have specific range of wave angles with regard to the direction of alignment, are always unstable at long wavelengths. Later, based on the microscopic interaction rules derived from experimental observations, Aranson et al. [13] proposed an equation for the probability density of bacterial position and orientation. Their model could successfully reproduce the coherent structures observed in experiments. Recently, Saintillan and Shelley [38, 39] proposed a kinetic model for a dilute suspension of self-locomotive particles, swimming in a low-Reynolds-number regime. Their model can be considered and extension of the studies on the passive-rod suspensions [40, 41], that includes an extra active stress corresponding to the induced force dipoles generated by the swimming particles. Using this model, they generalized the long-wave predictions of Simha and Ramaswamy [34], reporting that both aligned and isotropic suspensions are prone to instabilities. They also observed that the long-time nonlinear behavior of a suspension of pusher particles is associated

with formation of strong density fluctuations that go through a quasi-periodic merge and break up cycle. Saintillan and Shelley [38, 39] further showed that such instabilities enhance the mixing in suspensions of swimming bacteria. More recently, using a linear stability analysis based on the kinetic theory developed by Saintillan and Shelley [38, 39], Hohenegger and Shelley [42] showed that in a suspension of pusher particles, the growth of perturbations is associated with a growth in the oscillations of swimmer direction, but not with an increase in the concentration fluctuations. They further realized that the instability can arise only from the first azimuthal mode in the swimmer direction. Hohenegger and Shelley [42] also found that if there is no diffusive mechanism present, short-scale perturbations behave in an oscillatory fashion, which is determined by the initial condition. Subramanian and Koch [27] have also addressed the concentration dependence of instabilities in a suspension of swimming bacteria. As they have explained, the origin of the instabilities lies in the intrinsic force dipole of the active particles; while placing a passive particle in an extensional flow, causes it to generate a disturbance flow to weaken the imposed perturbation, a pusher particle in a linear shear flow, induces a disturbance velocity that acts to strengthen the perturbation of the imposed flow, since its force dipole is directed outwards along its axis. Subramanian and Koch [27] further recognize the orientation decorrelation mechanism as the dominant effect of hydrodynamic interactions in dilute suspensions of active particles, as is also emphasized in the recent work of Hohenegger and Shelley [42].

In practice, the behavior of a micro-organism may be affected by its neighboring organisms, through reproductive activities or consuming or escaping in order to avoid being consumed. The increased competition for food may also be a reason to avoid neighboring bacteria [5]. However, in most of the existing mathematical and numerical studies, such phenomena have not been considered and the interactions were assumed to be purely hydrodynamical. Interestingly, it seems that comparing the results from theoretical works with experiments, leads many researchers to believe that the hydrodynamic interactions between the bacteria can suffice to reproduce the observed collective behaviors [32].

In this work, we investigate pattern formation in suspensions of swimming micro-organisms in the presence of an external shear flow. Including the shear flow will allow us to analyze the behavior of such suspensions in more realistic situations where ambient flow is present, as in oceans where motility could influence the bacterial ecology. Moreover, we will be able to investigate the effect of collective dynamics on the suspensions properties. In this regard, we study rheological properties of the active suspensions that have been recently subject to much interest and reported to show unexpected behaviors [43, 44, 45, 46, 47] in the second part of our work.

Chapter 2

Flow Structures

2.1 Introduction

As mentioned in Chapter 1, in this work we are interested in studying dilute suspensions of swimming self-propelled particles in the presence of an external shear flow. It is of high interest to discover how the pattern formation and orientation distribution of flow structures in active suspensions would be affected by an external flow that would simulate the more realistic environments, in which the bacteria live. As noted in Chapter 1, turbulent-like behavior has been observed in concentrated suspensions of micro-organisms. Such observations motivate us to make use of the vast turbulent-flows literature in oder to analyze the pattern formation in these suspensions in more detail. In fact, making benefit from the tools that are widely used to quantify turbulence, we can compare the flows developed in active suspensions with turbulent flows and investigate how similar these two different flows at two extreme values of Reynolds number really are. In order to achieve this goal, we first review some of the major studies performed on homogeneous turbulent shear flow, and then use some of the tools introduced in our work. For more details on these investigations, the reader is referred to a recent review by Wallace [48].

Among the very first numerical studies on turbulent shear flows, Rogers and Moin [49] studied the structure of the vorticity fields. They reported that coherent vortical structures are present in the flow and they tend to become inclined in the flow direction. Their simulations also indicated that the vorticity occurs in coherent filaments and the pulling of vortex filaments by the mean shear, aligns them with the direction of stretching strain. Ashurst et al. [50] later studied the alignment between vorticity and eigenvectors of the strain-rate tensor. They found that in both isotropic and homogeneous turbulent flows, there is a tendency for the vorticity to point in the intermediate strain direction and at three-fourths of their sample points, this intermediate strain turned out to be positive (extensive). They also observed that there is an increased probability for the scalar gradient to be aligned with the most compressive strain direction. Ashurst et al. [50] tried to explain these phenomena using angular momentum conservation. They suggested that in turbulent flows, stretching vortices become generated as a result of coupled act of vorticity and strain rate to

conserve the angular momentum; these stretching vortices create large strains in the plane normal to their axis. Therefore, scalar gradients become strengthened near such vortex filaments due to both compression and rotation, and tend to align in the compressive strain direction. However, these gradients are limited due to the viscosity in the plane normal to the vortex axis, and are negligible along the vortex axis, resulting in conservation of two components of the angular momentum; hence, the third component would also be conserved [50]. Jimenez [51] later offered a kinematic explanation for the alignment properties observed. He mentions that the alignment of the vorticity with the intermediate strain was not expected a priori because of the assumption that the vorticity would be stretched along any strain-rate eigenvector with a positive eigenvalue, and eventually aligns with the direction corresponding to the greatest positive eigenvalue. In fact, as Jimenez [51] explains, it can be shown that it is most likely for a strain-rate tensor to have two positive eigenvalues, resulting in the speculation that the flow should be dominated with vortex sheets; consequently, even the existence of vortex tubes was a matter of debate initially. Jimenez [51] suggests that, as the vorticity becomes strong enough, it would make the strain tensor to rotate towards the vortex axis.

In the present work, we first describe the kinetic model previously introduced by Saintillan and Shelley [38, 39] in Section 2.2. Using this model, we then analyze the effect of an external shear flow on the linear stability of active suspensions in Section 2.3. In particular, we show that the linear stability analysis predicts that the shear flow dampens the instabilities. In Section 2.5, we then perform 3D numerical simulations and show that our results in fact verify the predictions of stability analysis, i.e. the shear flow is shown to dampen the instabilities. The rate of this stabilizing effect is shown to be direction dependent; it is fastest in the flow direction and slowest in the direction perpendicular to the shear plane. Moreover, it is shown that shear flow tends to align the structures in the flow direction. Some of the tools widely used in turbulence literature to analyze the flows are also introduced, and some of the results are compared with those reported in homogeneous turbulent shear flows.

2.2 Kinetic Theory

Following the kinetic model previously developed by Saintillan and Shelley [38, 39], we represent the configuration of a suspension of swimming particles by means of a time-dependent probability distribution function $\Psi(\mathbf{x}, \mathbf{p}, t)$ for the particle center-of-mass position $\mathbf{x}$ and unit orientation vector $\mathbf{p}$, which describes the swimming direction. This distribution function satisfies a conservation (or Smoluchowski) equation [52]

$$\frac{\partial \Psi}{\partial t} = -\nabla_x \cdot (\dot{\mathbf{x}}\Psi) - \nabla_p \cdot (\dot{\mathbf{p}}\Psi), \tag{2.1}$$

where ∇_p is the gradient operator on the surface of the unit sphere Ω

$$\nabla_p = (\mathbf{I} - \mathbf{pp}) \cdot \frac{\partial}{\partial \mathbf{p}}. \tag{2.2}$$

The particle fluxes $\dot{\mathbf{x}}$ and $\dot{\mathbf{p}}$ in Equation (2.1) are modeled as

$$\dot{\mathbf{x}} = U_0\mathbf{p} + \mathbf{v} - D\,\nabla_x(\ln \Psi), \tag{2.3}$$

$$\dot{\mathbf{p}} = (\mathbf{I} - \mathbf{pp}) \cdot \nabla_x \mathbf{v} \cdot \mathbf{p} - d\,\nabla_p(\ln \Psi). \tag{2.4}$$

In Equation (2.3), the center-of-mass flux is expressed as the sum of three terms, accounting for particle swimming with velocity $U_0\mathbf{p}$, advection by the local fluid velocity $\mathbf{v}(\mathbf{x}, t)$, and center-of-mass diffusion with isotropic diffusivity D assumed to be constant. Similarly, Equation (2.4) accounts for particle rotation under the effect of the local velocity gradient via Jeffery's equation [53], where it is assumed that the particle has a high aspect ratio. Rotational diffusion is also included with constant diffusivity d. Finally, the probability distribution function is normalized as

$$\frac{1}{V}\int_V \mathrm{d}\mathbf{x} \int_\Omega \mathrm{d}\mathbf{p}\Psi(\mathbf{x}, \mathbf{p}, \mathrm{t}) = \mathrm{n}. \tag{2.5}$$

Here, $V = L^3$ denotes the volume of the system and is assumed to be cube of linear dimension L, and $n = N/V$ denotes the mean number density of the suspension, where N is the total number of swimming particles.

To close Equations (2.1), (2.3) and (2.4), the fluid velocity $\mathbf{v}$ and corresponding velocity gradient $\nabla_x\mathbf{v}$ must be determined. Here, we decompose the velocity as the sum of an imposed linear flow with uniform and constant velocity gradient $\mathbf{A}$ and of the disturbance velocity $\mathbf{u}$ induced by the particles as they swim

$$\mathbf{v}(\mathbf{x}, t) = \mathbf{x} \cdot \mathbf{A} + \mathbf{u}(\mathbf{x}, t). \tag{2.6}$$

For a linear shear flow in the x direction, the imposed velocity gradient may be expressed as $\mathbf{A} = Sy\hat{\mathbf{x}}$, where S is the constant shear rate (see Figure 2.1). In the low-Reynolds-number regime relevant to the locomotion of micro-organisms, the disturbance fluid flow driven by the particles satisfies the Stokes equations

$$\nabla_x q - \mu\nabla_x^2\mathbf{u} = \nabla_x \cdot \boldsymbol{\Sigma}^p, \quad \nabla_x \cdot \mathbf{u} = 0, \tag{2.7}$$

where μ is the viscosity of the suspending fluid, and q is the fluid pressure. In Equation (2.7), $\boldsymbol{\Sigma}^p(\mathbf{x}, t)$ is the

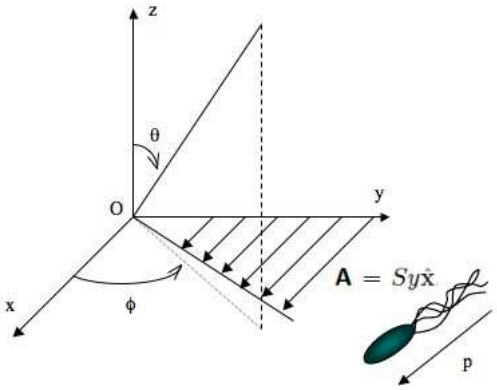

Figure 2.1: The coordinate system used in the work. The particle director $\mathbf{p}$ indicates the orientation of the particles and direction of swimming relative to the external flow.

particle extra stress, obtained as the orientational average of the force dipoles $\mathbf{S}(\mathbf{p})$ exerted by the particles on the fluid

$$\boldsymbol{\Sigma}^p(\mathbf{x},t) = \int_\Omega \mathbf{S}(\mathbf{p})\Psi(\mathbf{x},\mathbf{p},t)\,\mathrm{d}\mathbf{p}. \tag{2.8}$$

For a swimming particle in an external flow, the dipole $\mathbf{S}(\mathbf{p})$ arises from three contributions: resistance to stretching under the external flow, Brownian rotations, and self-propulsion. The first two contributions also arise with the passive particles [54]. The dipole due to the external flow can be expressed as

$$\mathbf{S}^f(\mathbf{p}) = C(\mathbf{pp} : \mathbf{A})\left(\mathbf{pp} - \frac{\mathbf{I}}{3}\right), \tag{2.9}$$

where the constant C depends on the particle shape; for a slender particle of inverse aspect ratio ε, it can be obtained from slender-body theory as $C = \pi\mu l^3/6\ln(2/\varepsilon)$. The contribution of the Brownian motions can be expressed as

$$\mathbf{S}^b(\mathbf{p}) = 3kT\left(\mathbf{pp} - \frac{\mathbf{I}}{3}\right), \tag{2.10}$$

in which kT denotes the thermal energy of the fluid. Finally, the permanent dipole resulting from self-propulsion can be expressed in the form

$$\mathbf{S}^s(\mathbf{p}) = \sigma_0\left(\mathbf{pp} - \frac{\mathbf{I}}{3}\right), \tag{2.11}$$

where the dipole strength σ_0 is a constant parameter whose sign depends on the mechanism for swimming: head-actuated swimmers or pullers, such as the alga *Chlamydomonas Reinhardtii*, result in $\sigma_0 > 0$, whereas rear-actuated swmmers or pushers, such as most swimming bacteria including *E. coli* and *B. subtilis*, result in $\sigma_0 < 0$. In addition, σ_0 is related to the single-particle swimming speed U_0 and particle length l by a

relation of the form $\sigma_0/\mu U_0 l^2 = \alpha$, where α is a dimensionless $O(1)$ parameter with the same sign as σ_0. In the following, we non-dimensionalize the equations using the characteristic length, velocity, and time scales $l_c = (nl^2)^{-1}$, $u_c = U_0$, and $t_c = l_c/u_c$. Upon non-dimensionalization, the conservation equation (i.e. Equation (2.1)) remains the same, but Ψ is now normalized as

$$\frac{1}{V^*}\int_V \mathrm{d}\mathbf{x}\int_\Omega \mathrm{d}\mathbf{p}\Psi(\mathbf{x},\mathbf{p},\mathrm{t}) = 1, \tag{2.12}$$

where the dimensionless cell volume is $V^* = (L/l_c)^3 = (nl^2L)^3$. The flux Equations (2.3)–(2.4) become

$$\dot{\mathbf{x}} = \mathbf{p} + \mathbf{v} - D^*\,\nabla_x(\ln\Psi), \tag{2.13}$$

$$\dot{\mathbf{p}} = (\mathbf{I} - \mathbf{pp})\cdot\nabla_x\mathbf{v}\cdot\mathbf{p} - d^*\,\nabla_p(\ln\Psi), \tag{2.14}$$

with dimensionless diffusion coefficients given by $D^* = Dnl^2/U_0$ and $d^* = dt_c = d/U_0 nl^2$. Finally, the dimensionless external shear rate is obtained as $S^* = St_c = S/U_0 nl^2$, and the disturbance velocity satisfies the dimensionless Stokes equations

$$\nabla_x q - \nabla_x^2\mathbf{u} = \nabla_x\cdot\mathbf{\Sigma}^p, \quad \nabla_x\cdot\mathbf{u} = 0, \tag{2.15}$$

with

$$\mathbf{\Sigma}^p(\mathbf{x},t) = (\alpha + Br^*)\int_\Omega \Psi(\mathbf{x},\mathbf{p},t)\left(\mathbf{pp} - \frac{\mathbf{I}}{3}\right)\mathrm{d}\mathbf{p} + \mathrm{C}^*\int_\Omega \Psi(\mathbf{x},\mathbf{p},\mathrm{t})(\mathbf{pp}:\mathbf{A})\left(\mathbf{pp} - \frac{\mathbf{I}}{3}\right)\mathrm{d}\mathbf{p}, \tag{2.16}$$

where $\alpha = \sigma_0/\mu U_0 l^2$, $Br^* = 3kT/\mu U_0 l^2$ and $C^* = Cn/\mu$. Next, we omit asterisks * on dimensionless parameters.

We define $S = \int \mathrm{d}\mathbf{x}\int \mathrm{d}\mathbf{p}\frac{\Psi}{\Psi_0}\ln(\frac{\Psi}{\Psi_0})$ as the relative configurational average entropy, where Ψ_0 is the probability density for the spatially uniform state in the presence of shear flow. We can solve for Ψ_0 using Equation (2.1) when there are no spatial gradients present. The system realizes its minimum entropy of value zero when $\Psi = \Psi_0$. The entropy as defined here obeys the evolution equation [39]

$$\Psi_0\dot{S} = -\frac{6}{\alpha}\int_V \mathrm{d}\mathbf{x}\mathbf{E}:\mathbf{E} - \int_\mathrm{V}\mathrm{d}\mathbf{x}\int_\Omega \mathrm{d}\mathbf{p}\left[\mathrm{D}|\nabla_\mathbf{x}\ln\Psi|^2 + \mathrm{d}|\nabla_\mathbf{p}\ln\Psi|^2\right]\Psi. \tag{2.17}$$

The first term on the right-hand side is proportional to the rate of viscous dissipation, which is a strictly positive term. Therefore, for a suspension of pushers $\alpha > 0$, any fluctuation away from the isotropic state Ψ_0 is expected to decay by both diffusive processes and the viscous dissipation term. But for the suspension

of pushers $\alpha < 0$, the leading term is positive that allows the possibility of growth of fluctuations away from the base state until they become balanced with the diffusive terms. As a result, in this work we focus on the case of pushers, which are more common in nature and shows more interesting behavior.

2.3 Linear Stability Analysis

The stability of an isotropic homogeneous active suspension was previously investigated in the absence of an external flow ($S = 0$) by Saintillan and Shelley [38, 39] and Hohenegger and Shelley [42]. In particular, it was found that suspensions of pushers are subject to a long-wavelength instability below a given wavenumber k_c, whereas suspensions of pullers are stable for $k \leq k_c$. Above k_c, both suspensions of pushers and pullers were found to be stable in the presence of rotational diffusion [42]. While the linear instability for pushers was found not to result in concentration fluctuations, numerical simulations demonstrated that such fluctuations still appear at long times as a result of nonlinearities [39]. In this section, we extend these previous studies to consider the effect of a non-zero external flow on the dynamics ($S \geq 0$).

In the base state, no hydrodynamic interactions is present and the system reduces to a single self-propelled particle in a linear shear flow. For such a system, the configuration of the particle may be represented by a distribution function $\Psi_0(\mathbf{p})$, which satisfies the steady state Fokker-Planck equation [52]

$$\nabla_p \cdot (\dot{\mathbf{p}}_0 \Psi_0) - d\, \nabla_p^2(\Psi_0) = 0, \tag{2.18}$$

where $\dot{\mathbf{p}}_0$ denotes the rotational velocity of the particle resulting from the local shear flow, and may be modeled using Jeffery's equation [55, 53] as

$$\dot{\mathbf{p}}_0 = (\mathbf{I} - \mathbf{pp}) \cdot \mathbf{A} \cdot \mathbf{p}. \tag{2.19}$$

For a linear shear flow, Equation (2.18) must be solved numerically, for instance using finite differences [56], or using spectral expansions on the basis of surface harmonics [57, 46]. Note that in the base state, Ψ_0 is uniform in space and therefore, no disturbance flow occurs: $\mathbf{u}_0(\mathbf{x}, t) = \mathbf{0}$, $q_0(\mathbf{x}, t) = 0$.

Next, we consider a small perturbation with respect to the uniform base state ($\epsilon \ll 1$)

$$\Psi(\mathbf{x}, \mathbf{p}, t) = \Psi_0(\mathbf{p}) + \epsilon \Psi_1(\mathbf{x}, \mathbf{p}, t), \tag{2.20}$$

with corresponding velocity and pressure fields

$$\mathbf{u}(\mathbf{x},t) = \epsilon \mathbf{u}_1(\mathbf{x},t), \quad q(\mathbf{x},t) = \epsilon q_1(\mathbf{x},t), \tag{2.21}$$

which in turn causes the rotation of the particles at the angular velocity $\dot{\mathbf{p}} = \dot{\mathbf{p}}_0 + \epsilon \dot{\mathbf{p}}_1$ with

$$\dot{\mathbf{p}}_1 = (\mathbf{I} - \mathbf{pp}) \cdot \nabla \mathbf{u}_1 \cdot \mathbf{p}. \tag{2.22}$$

Substituting Equations (2.20)–(2.21) into the governing equations and linearizing in ϵ with respect to the base state, we obtain the following equation for Ψ_1

$$\begin{aligned} \frac{\partial \Psi_1}{\partial t} + (\mathbf{x} \cdot \mathbf{A}^\dagger + \mathbf{p}) \cdot \nabla_x \Psi_1 - 3(\mathbf{pp} : \mathbf{A})\Psi_1 - 3(\mathbf{pp} : \nabla_x \mathbf{u}_1)\Psi_0 \\ + \dot{\mathbf{p}}_0 \cdot \nabla_p \Psi_1 + \dot{\mathbf{p}}_1 \cdot \nabla_p \Psi_0 - D\nabla_x^2 \Psi_1 - d\nabla_p^2 \Psi_1 = 0. \end{aligned} \tag{2.23}$$

Now, we consider the evolution of a distribution perturbation written as a plane wave of wavevector $\mathbf{k}$ and complex frequency $\sigma = \sigma_r + \imath\sigma_i$

$$\Psi_1(\mathbf{x},\mathbf{p},t) = \tilde{\Psi}(\mathbf{p},\mathbf{k},\sigma,t) \exp(\imath \mathbf{k} \cdot \mathbf{x} + \sigma t). \tag{2.24}$$

We wish to determine the dispersion relation $\sigma(\mathbf{k})$ allowing for such modes to satisfy the linearized conservation Equation (2.23), and more specifically to identify the wavevectors $\mathbf{k}$ leading to positive growth rates, i.e. positive values of the real part (σ_r) of the frequency that will result in the amplification of perturbations in time.

By linearity of the Stokes Equations (2.7), the disturbance velocity induced by the distribution perturbation Equation (2.24) can also be written as a plane wave of the same wavevector and frequency

$$\mathbf{u}_1(\mathbf{x},t) = \tilde{\mathbf{u}}(\mathbf{k},\sigma,t) \exp(\imath \mathbf{k} \cdot \mathbf{x} + \sigma t), \tag{2.25}$$

where the Fourier coefficients $\tilde{\mathbf{u}}(\mathbf{k},\sigma,t)$ can be expressed as [58]

$$\tilde{\mathbf{u}}(\mathbf{k},\sigma,t) = \frac{\imath\alpha}{k} \left(\mathbf{I} - \hat{\mathbf{k}}\hat{\mathbf{k}}\right) \cdot \left(\int_\Omega \tilde{\Psi}(\mathbf{p},\mathbf{k},\sigma,t) \left(\mathbf{pp} - \frac{\mathbf{I}}{3} \right) \mathrm{d}\mathbf{p} \right) \cdot \hat{\mathbf{k}}, \tag{2.26}$$

where $\hat{\mathbf{k}} \equiv \mathbf{k}/|\mathbf{k}|$. Substituting this expression into Jefferys Equation (2.22) allows us to calculate the Fourier

coefficient $\tilde{\dot{\mathbf{p}}}(\mathbf{p},\mathbf{k},\sigma,t)$ of the angular velocity as well

$$\tilde{\dot{\mathbf{p}}}(\mathbf{p},\mathbf{k},\sigma,t) = -\frac{\alpha}{k}\left(\mathbf{I}-\mathbf{pp}\right)\cdot\left[\left(\mathbf{I}-\hat{\mathbf{k}}\hat{\mathbf{k}}\right)\cdot\left(\int_{\Omega}\tilde{\Psi}(\mathbf{p},\mathbf{k},\sigma,t)\left(\mathbf{pp}-\frac{\mathbf{I}}{3}\right)\,\mathrm{d}\mathbf{p}\right)\cdot\hat{\mathbf{k}}\,\mathbf{k}\right]\cdot\mathbf{p}. \tag{2.27}$$

Finally, using Equations (2.24), (2.26), and (2.27) for the Fourier coefficients of the concentration distribution, disturbance velocity, and angular velocity, we find that the linearized conservation Equation (2.23) becomes

$$\begin{aligned}\left(\sigma + k^2 D + \imath\mathbf{k}\cdot\mathbf{p} - 3\mathbf{p}\cdot\mathbf{A}\cdot\mathbf{p}\right)\tilde{\Psi}(\mathbf{p},\mathbf{k}) - 3\imath\left(\mathbf{p}\cdot\mathbf{k}\right)\left(\mathbf{p}\cdot\tilde{\mathbf{u}}(\mathbf{k})\right)\Psi_0(\mathbf{p}) \\ + \dot{\mathbf{p}}_0\cdot\nabla_p\tilde{\Psi}(\mathbf{p},\mathbf{k}) + \tilde{\dot{\mathbf{p}}}\cdot\nabla_p\Psi_0(\mathbf{p},\mathbf{k}) - d\nabla_p^2\tilde{\Psi}(\mathbf{p},\mathbf{k}) = 0.\end{aligned} \tag{2.28}$$

For a given $\mathbf{k}$, this integro-differential Equation (2.28) is a generalized eigenvalue problem for $\left(\tilde{\Psi}(\mathbf{p},\sigma),\sigma\right)$. The original dispersion relation of Saintillan and Shelley [39] can be recovered by setting terms corresponding to shear equal to zero, and by considering the case of an isotropic orientation distribution, i.e. $\Psi_0 = 1/4\pi$. Moreover, it is worth mentioning that as Saintillan and Shelley [39] discussed, the linear stability analysis cannot predict the growth of concentration fluctuations. In the present analysis with $\mathbf{k} = \hat{\mathbf{z}}$, we also found the same result in the presence of shear flow; that is to say

$$c_1(\mathbf{x},t) = \int_{\Omega}\Psi_1(\mathbf{x},\mathbf{p},t)\,\mathrm{d}\mathbf{p} = 0, \tag{2.29}$$

or the perturbed concentration field is uniform in space. This result of linear stability analysis indeed is found in numerical simulations of Section 2.5 not to be true, and concentration fluctuations do occur because of nonlinearities.

In order to solve Equation (2.28), we expand the distribution function on the basis of surface harmonics, $\tilde{\psi}(\mathbf{p}) = \sum_{l=0}^{M}\sum_{m=-l}^{l} a_{l,m}Y_l^m(\theta,\phi)$. Then substituting this series into Equation (2.28), it can be turned into a system of algebraic eigenvalue problems for the coefficients $a_{l,m}$. We present in the Appendix the identities related to the spectral solution (for more details, the reader is referred to the recent work of Hoffman and Shaqfeh [59]).

A general solution of Equation (2.28) cannot be easily obtained. In this study, we limit ourself to the case of $\mathbf{k} = \hat{z}$, which indeed will be shown in the numerical simulations to be the most unstable direction. The solution of Equation (2.28) can be obtained for various choices of diffusion parameters D, d and shear rate S. Including translational diffusion D, as discussed by Saintillan and Shelley [39], simply shifts the solution

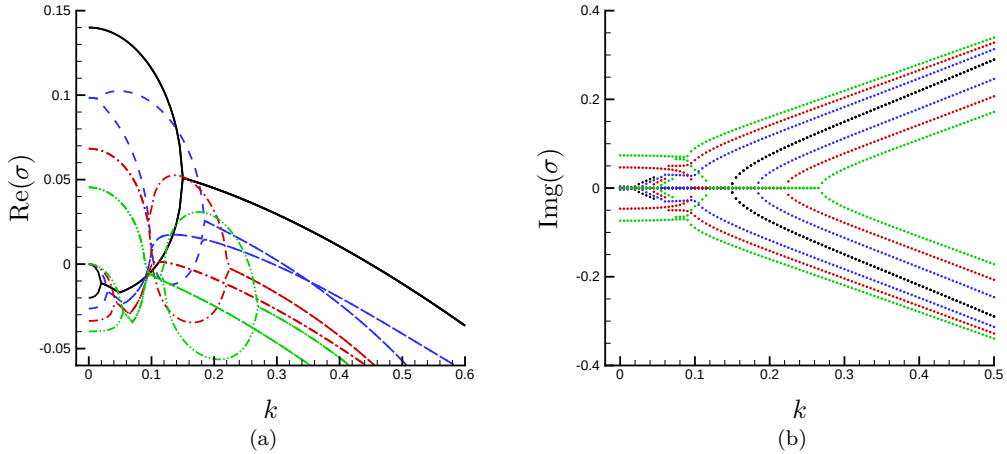

Figure 2.2: Effect of shear rate on the (a) real part, and (b) imaginary part of growth rate σ. $S = 0$: black solid line, $S = 0.1$: blue dashed line, $S = 0.2$: red dash dotted line, and $S = 0.3$: green dash dot dotted line.

for $\mathrm{Re}(\sigma)$ by $-Dk^2$ that results in a more rapid damping of instabilities at high wave numbers; however, the low wave numbers remain almost intact by including translational diffusion. The effect of rotational diffusion on the other hand seems to be more subtle. Recently, Hohenegger and Shelley [42] found that the growth of perturbations in suspension of pusher particles in not associated with growth of concentration fluctuations, but with a proliferation of oscillations in swimmer direction. This observation suggests that the rotational diffusivity can play an important role in stabilizing the flow. We therefore, investigate the effect of both rotational diffusion and shear rate on the growth rate.

Figure 2.2 shows the effect of the external flow strength on the growth rate. When there is no shear flow present, at low wave numbers, $\mathrm{Re}(\sigma) > 0$ and $\mathrm{Img}(\sigma) \equiv 0$, suggesting that the shear stress fluctuations will amplify exponentially at low wave numbers. At higher wave numbers, the imaginary part of σ becomes non-zero that suggests that stress oscillations will occur and amplify as the real part of σ is still positive. For high enough wave numbers, the $\mathrm{Re}(\sigma)$ becomes negative and the stress fluctuations are damped. The effect of shear as it appears from Figure 2.2 is to damp the instabilities. As shear increases, it decreases the magnitude of the positive $\mathrm{Re}(\sigma)$. It also causes unexpected branchings in the real part of the growth rate. The behavior of imaginary part of the growth rate in wave number is almost the same as for the case without shear, except for the fact that shear makes the imaginary part of σ non-zero even at low wave numbers. This observation suggests that at low wave numbers shear causes stress oscillations, but weakens the exponential growth of these stress fluctuations. The shear flow however, damps the higher wave number fluctuations. The branching also seems to be strengthened in the presence of shear; particularly, at long wave numbers for the $\mathrm{Img}(\sigma)$, it generates two branches, one greater and one lower in magnitude than in the case without

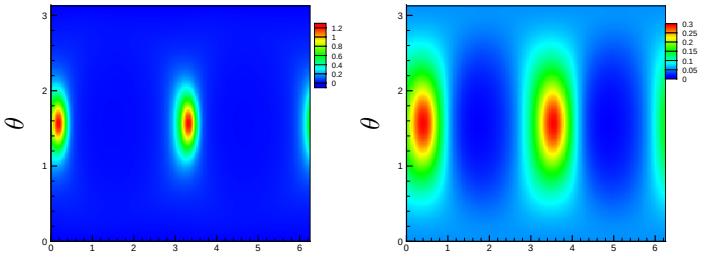

Figure 2.3: Base state distribution functions for $S = 0.1$, $D = 0.01$ and (a) $d = 0.001$, and (b) $d = 0.01$.

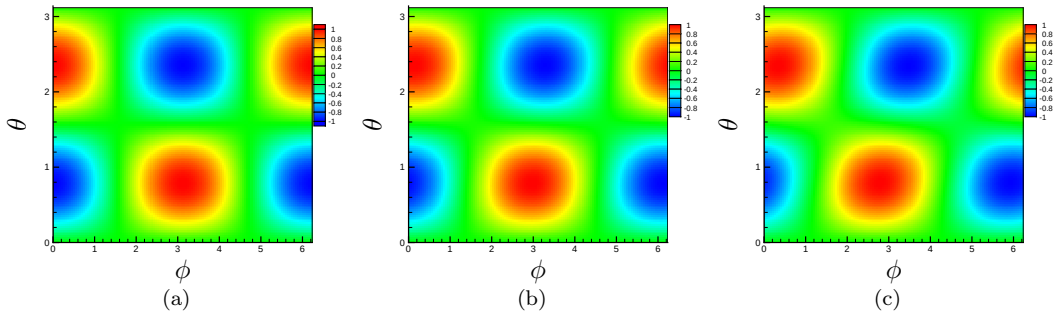

Figure 2.4: Most unstable eigen modes for the distribution function $\tilde{\Psi}(\mathbf{p})$ for $S = 0$, and wave vectors: (a) $\mathbf{k} = 0$, (b) $\mathbf{k} = 0.1$, and (c) $\mathbf{k} = 0.2$.

shear. In general, it might be perceived from this figures that shear flow tends to damp the higher wave number fluctuations, but strengthens the stress oscillations. As will be discussed in Section 2.5 numerical simulations show that the former effect is the dominant one.

It is interesting to take a look at the distribution function at the base and also perturbed states. When there is no shear present, the base state distribution is homogeneous $\Psi_0 = 1/4\pi$; however, shear orients the flow. Recently, the effect of shear on the orientation distribution has been investigated by Saintillan [46]. Here, we are interested mainly in the perturbed state, but it is also desirable to know the corresponding base states. Figure 2.3 shows the base state distributions for $S = 0.1$ and two different rotational diffusion values (i.e. $d = 0.001, 0.01$). As it appears, shear tends to reorient the particles in the flow direction (i.e. $\phi = 0, \pi/2$) while the effect of rotational diffusion appears to be smoothing out the distribution. The perturbed distribution function corresponding to different wave lengths is also considered here. Figure 2.4 shows the distribution function when there is no shear present and Figure 2.5 shows the same data in the presence of shear.

As mentioned above, it is also interesting to investigate the effect of rotational diffusion on the growth

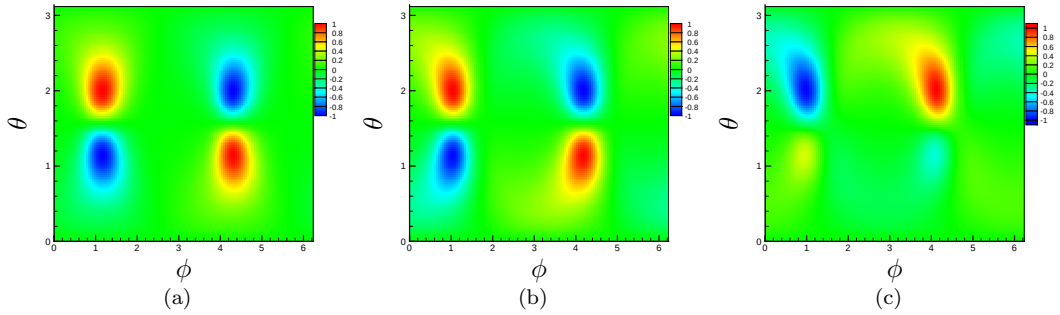

Figure 2.5: Most unstable eigen modes for the distribution function $\tilde{\Psi}(\mathbf{p})$ for $S = 0.1$, and wave vectors: (a) $\mathbf{k} = 0$, (b) $\mathbf{k} = 0.1$, and (c) $\mathbf{k} = 0.2$.

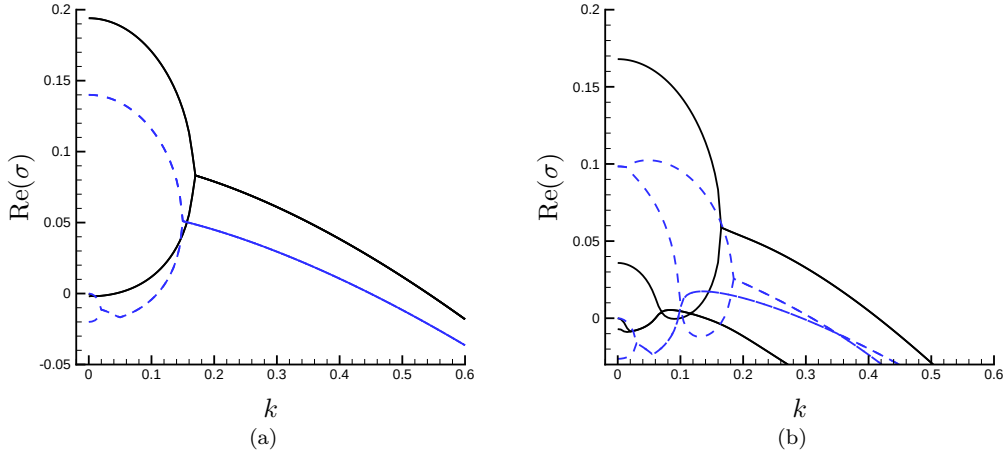

Figure 2.6: Effect of rotational diffusion d on the real part of σ for (a) $S = 0$, and (b) $S = 0.1$. $d = 0.001$: solid line, $d = 0.01$: dashed line.

rate. Figure 2.6 shows how d affects the growth rate for different shear rates. It appears that as for the shear rate, the rotational diffusion tends to stabilize the high wave number fluctuations and also it causes branching in the growth rate.

2.4 Simulation Techniques

Next, we present results from three-dimensional numerical simulations of the kinetic equations described in Section 2.2. Note that the kinetic model involves five independent variables in addition to time: three spatial coordinates x, y, and z, and two angles θ and ϕ for the parameterization of the orientation vector $\mathbf{p}$. The high-dimensionality of the problem makes numerical solutions very expensive, and for this reason we developed a parallel scalable code, which was used in all the simulations. Typical grids of 128^3 points

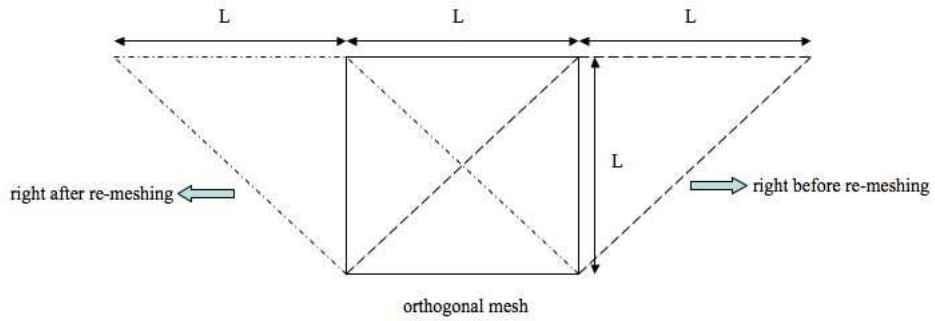

Figure 2.7: The computational grid deforms with the imposed shear flow to allow using the periodic boundary condition. Remeshing is done at regular intervals when $S \times t = n(n+1)/2$ and the grid becomes orthogonal whenever $S \times t = 2n$, where n is a positive integer.

in space and 16^2 points for the orientation angles were used, corresponding to a total of more than half a billion grid points.

In order to be able to use periodic boundary conditions for the solution of the flow equations, we use Rogallo's classic method, in which the computational grid deforms to follow the mean imposed flow, as shown in Figure 2.7 [60, 49]. Specifically, if x, y, and z denote spatial coordinates in a fixed reference frame, we define a new set of coordinates x', y', and z' by

$$x' = x - S \times y \times t, \quad y' = y, \quad z' = z. \tag{2.30}$$

In this new coordinate system, a triply periodic field remains periodic in time, allowing the use of Fourier-based methods. Specifically, the Stokes Equation (2.7) is solved spectrally using truncated Fourier series expansions [58] and the fast Fourier transform (FFT) algorithm. Knowing the disturbance velocity field $\mathbf{u}$, we can then solve the conservation Equation (2.1) for the distribution function Ψ using second-order finite differences for the fluxes, and a second-order Adams-Bashforth time-marching scheme.

As a result of the imposed shear, the computational grid introduced above becomes skewed as time increases. To allow the simulation to progress for a desirable amount of time without introducing large errors, it is necessary to perform a remeshing of the grid at regular time intervals [60]. The remeshing procedure makes use of the periodicity in the streamwise direction to move the data from the skewed grid onto a grid that is skewed in the opposite direction. In order to avoid data interpolation, this procedure is performed whenever $S \times t = n(n+1)/2$ where n is a positive integer: at these times, grid points from the two skewed grids indeed exactly overlap [60, 49]. With this method, the computational grid exactly matches the original orthogonal mesh whenever $S \times t = 2n$, as shown in Figure 2.7.

In all simulations, translational and rotational diffusion are both included to ensure that the solutions

remain bounded over time (typical values of $D = d = 0.01$ were used). All simulations shown are for pusher particles with $\alpha = -1$, as suspensions of pullers are known to be stable. In all cases, the initial condition is taken to be a uniform isotropic suspension with a weak perturbation of the form

$$\Psi(\mathbf{x}, \theta, \phi) = \frac{1}{4\pi} + \sum_i \epsilon_i \cos(\mathbf{k}_i \cdot \mathbf{x} + \xi_i) P_i(\theta) Q_i(\phi), \tag{2.31}$$

where $|\epsilon_i| \ll 1$ is a random coefficient of small magnitude, ξ_i is an arbitrary phase, and P_i and Q_i are low-order trigonometric polynomials in θ and ϕ with random coefficients. The initial random perturbations used in the simulations are band-limited, and typically include only the 10 longest modes.

2.5 Numerical Simulation Results

At $t = 0$, the imposed distribution, as represented in Equation (2.31), contains fluctuations at many length scales, and correspondingly, the mean director field exhibits correlation only over very short length scales. At short times, the evolution of the distribution function is characterized mainly by the decay of the imposed initial perturbations. But as time goes on, structures of the box size begin to form. As a result of the balance between active input power and diffusivities, the system develops into statistically steady fluctuations after some time. At this stage, instabilities cause the structures to form and break up and reorganize repeatedly. How these correlated motions are affected by the external shear flow is of main interest here. Figure 2.8 shows the isosurfaces of the concentration field for different shear strengths.

2.5.1 Instabilities in the density field

The numerical simulations show that the external shear flow acts to stabilize the flow as predicted by the linear stability analysis, but interestingly, in this process four different regimes of instability can be identified as the rate of stabilizing by the shear flow is direction dependent. The isosurfaces do not have any preferred direction when there is no external shear flow present, as shown in Figure 2.8 (a). For the weak shear strengths, 3D instabilities can be observed; in such regimes, shear tends to align the tube-like concentration iso-structures in the most stretching direction of the mean shear (i.e. 45°). As shear increases, the instabilities in the flow direction become damped and structures becomes uniform in the flow direction. In this case instabilities can be observed in the plane normal to the flow direction (i.e. y-z plane); this kind of instability is similar to that observed in the 2D simulations of Saintillan and Shelley [38, 39]. For this case, as mentioned the tube-like structures are totally aligned in the flow direction (see Figure 2.8 (c)). As shear increases further, the flow stabilizes all the instabilities in the shear plane (i.e. x-y). In this case, the

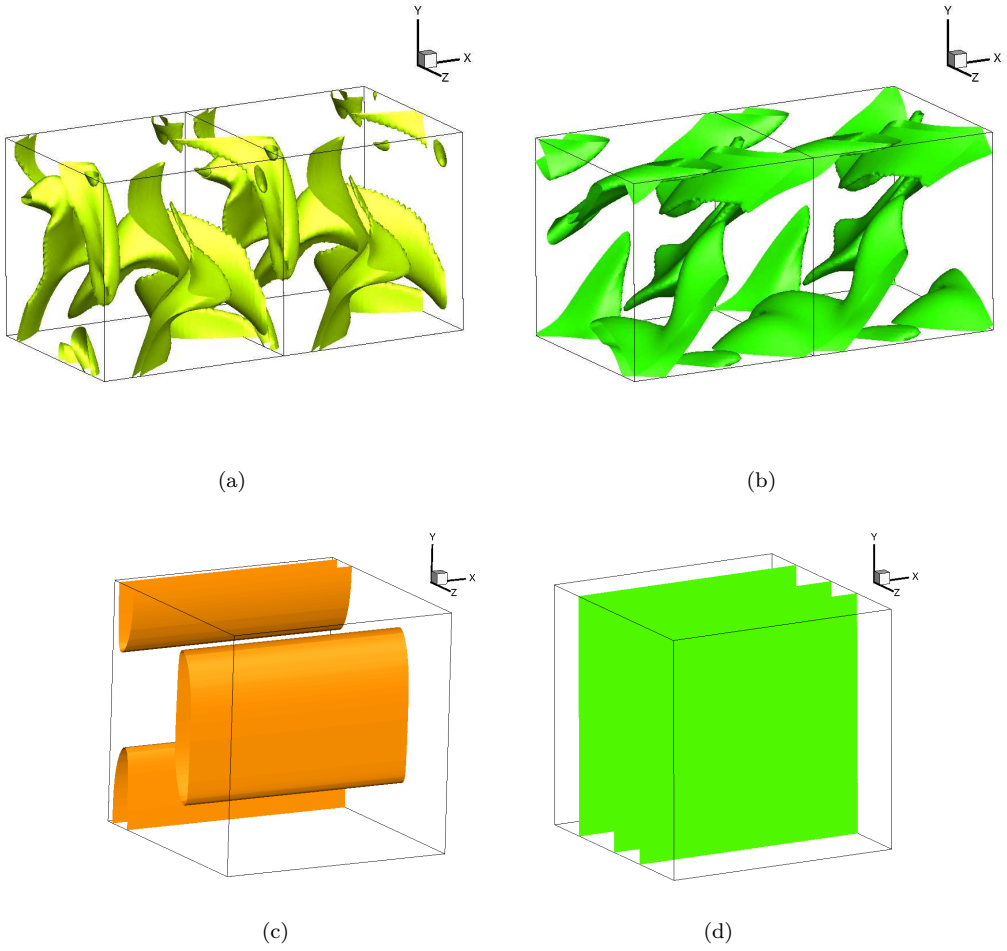

Figure 2.8: Concentration field isosurfaces for different shear rates: (a) $S = 0$, $c = 1.5$, (b) $S = 0.1$, $c = 1.2$, (c) $S = 0.14$, $c = 1.1$, (d) $S = 0.2$, $c = 1$.

flow is unstable only in the direction perpendicular to the shear plane (i.e. z direction) that results in the formation of band-like structures in this direction. But in this case, these bands do not merge and break up as observed by Saintillan and Shelley [38, 39], since there is no vorticity present in the flow. In fact, a closer look at the disturbance flow velocity field corresponding to this case, shows that it is consisted of jets of flow going up and down in the shear plane with almost no component in the z direction. That is why these bands are almost steady and do not break up. Finally, as shear strength increase further, the gradients in the z direction also become suppressed by the shear and all the instabilities in the flow become damped and the flow becomes akin to that of a single active particle in a spatially uniform shear flow [46]. Our simulations show that beyond shear strength of $S = 0.3$ there is no instability. In the following sections, we introduce some of the widely used tools in turbulence literature to investigate the observed instabilities more quantitatively and in detail. The similarities and differences of the observed turbulent-like motions with those of high-Reynolds-number turbulence are also discussed.

2.5.2 Vortical structures

Although the concept of vortices is considered to be as old as the subject of hydrodynamics, no single definition has been accepted for it so far [61]. As an example, Lugt [62] proposed that a multitude of material particles rotating around a common center, can be considered as a vortex. One may imagine a tube whose surface consists of vortex lines as a vortex; however, the existence of vortex cannot be implied merely by existence of a vortex tube. Some other intuitive ways of detecting vortices are also problematic; for instance, a set of spiraling streamlines cannot be considered a vortex since it is not Galilean invariant; a non-zero vorticity magnitude also can be considered as a necessary, but not sufficient, condition to find a vortex [61].

In spite of the lack of a single universally accepted definition for vortex, some vortex identification methods have been developed. These methods are based on the point-wise values of some specific functions, determining whether a point can be considered to be inside a vortex, or out of it. To meet the requirement of being Galilean invariant, these vortex detection methods are mostly based on the kinematic implications of velocity-gradient tensor $\nabla \mathbf{u}$. Among the proposed detection methods, the most popular ones are the Q criterion of Hunt, Wray, and Moin [63], the criterion developed by Chong, Perry and Cantwell [64] based on complex eigenvalues of $\nabla \mathbf{u}$, the method developed by Jeong and Hussain [61] that is called λ_2 criterion, and the proposed method by Zhou et al. [65]. While each of these methods might be better suited for specific types of flows, we decided to use the Q criterion, which is widely used as our vortex identifying tool (we compared our results using Q criterion with those obtained using λ_{ci}, and found that both show essentially

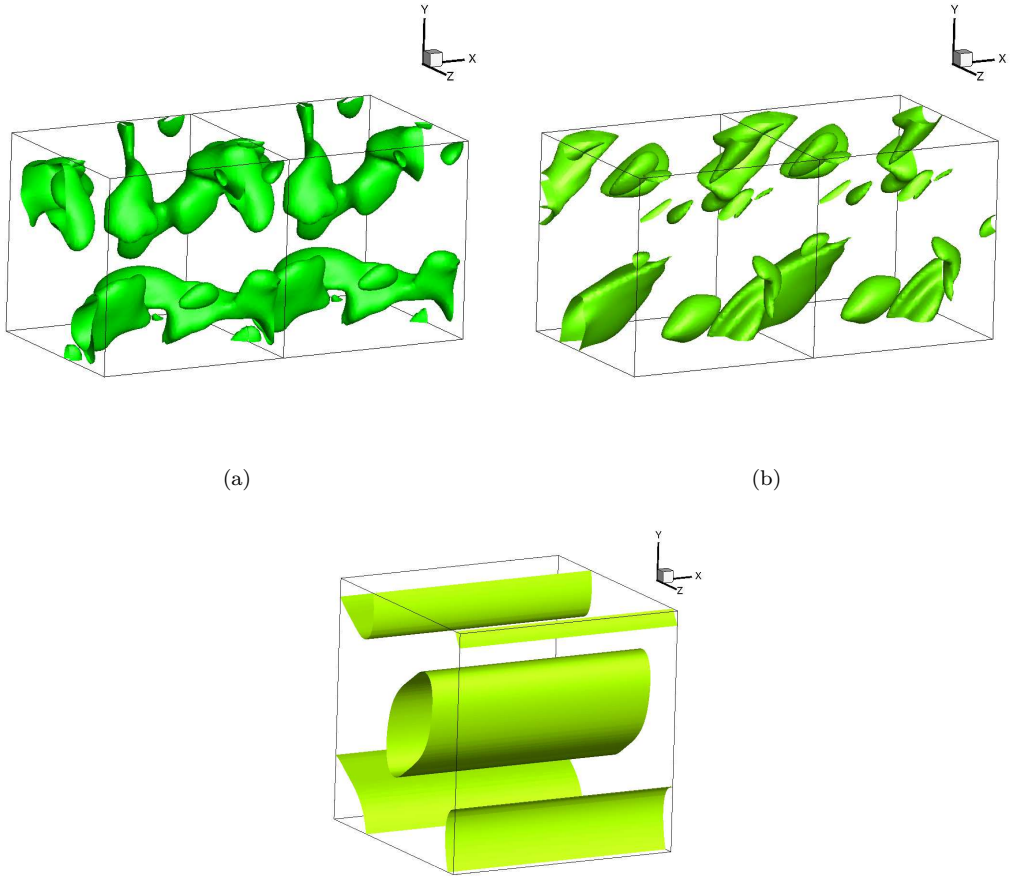

Figure 2.9: Vortex structures for different shear rates: (a) $S = 0$, $Q = 0.015$, (b) $S = 0.1$, $Q = 0.0075$, and (c) $S = 0.14$, $Q = 0.001$.

the same kind of structures.). In order to introduce the Q criterion, we need to first elaborate a little on the classification of 3D flow topologies, then we move on to analyzing the vortical structures in the flow.

For an observer, traveling with the local velocity of the flow, the local slope of streamlines at each point is indeterminate; that is to say each point can be considered a critical point. Therefore, such an observer, can categorize the flow topology based on the critical point terminology [64]. The velocity-gradient tensor can then be written as $\mathbf{A} = \nabla \mathbf{u} = \mathbf{E} + \mathbf{W}$, where $\mathbf{E}$ and $\mathbf{W}$ are rate of strain and rate of rotation tensors, respectively. The eigenvalues of velocity gradient satisfy the characteristc equation

$$\lambda^3 + P\lambda^2 + Q\lambda + R = 0, \tag{2.32}$$

where the invariants can be defined as

$$
\begin{aligned}
P &= -trace(\mathbf{A}) = -\mathbf{E}_{ii}, && \text{(2.33a)}\\
Q &= (P^2 - trace(\mathbf{A}^2))/2 \\
&= (P^2 - \mathbf{E}_{ij}\mathbf{E}_{ji} - \mathbf{W}_{ij}\mathbf{W}_{ji})/2, && \text{(2.33b)}\\
R &= (-P^3 + 3PQ - trace(\mathbf{A}^3))/3 \\
&= (-P^3 + 3PQ - \mathbf{E}_{ij}\mathbf{E}_{jk}\mathbf{E}_{ki} - 3\mathbf{W}_{ij}\mathbf{W}_{jk}\mathbf{E}_{ki})/3. && \text{(2.33c)}
\end{aligned}
$$

The invariants of the rate of strain tensor (P_s, Q_s, R_s) can be obtained from the above equations just by setting $\mathbf{W} = 0$. Also it should be noted that the flow studied here is incompressible; hence, $P = P_s = 0$. Thus, the second and third invariants (Q, R), and (Q_s, R_s), suffice to describe the local geometry of the flow. For the rotation tensor $\mathbf{W}$, the first and third invariants are identically zero, but the second invariant Q_w is non-zero and is proportional to the enstrophy density $(w_i w_i/2)$; it can be obtained by setting P and S equal to zero in the above set of equations.

Considering the definition of the second invariant of the velocity gradient, suggests that it can be used to identify the vortical structures in the flow

$$Q = \frac{1}{2}(\|\mathbf{W}\|^2 - \|\mathbf{E}\|^2). \tag{2.34}$$

In fact, Q corresponds to the local balance between shear strain and vorticity magnitude. Points with positive Q can be regarded as vorticity dominated, while those corresponding to the negative values represent the strain-dominated flows [63, 61].

Figure 2.9 shows the Q isosurfaces for the different shear rates. $Q > 0$ isosurfaces represent the vortical structures in the flow. As the figures clearly show, in accordance with the changes in the concentration field, the vortical structures also change with the shear rate strength. While there is no preferred direction without shear, the structures tend to align in the most stretching direction for intermediate shear rates. For the two-dimensional instabilities corresponding to higher shear rates, the vortex tubes become uniform in the flow direction while rotating the fluid in plane perpendicular to the flow direction. Note that for the shear rates corresponding to the one-dimensional instability there will be no vortical structure present and as discussed earlier, jet-like flow with no vorticity is observed.

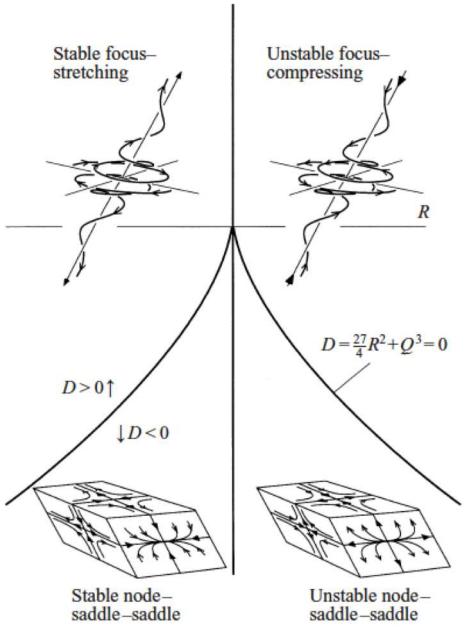

Figure 2.10: Three-dimensional topologies in the Q–R plane. $P = 0$ for incompressible flows. (Picture courtesy of Soria et al. [2])

2.5.3 Q–R Plots

It can be shown that the Q–R plane can be divided in to two parts with regard to the eigenvalues of velocity gradient. In this plane, the nature of the eigenvalues can be determined by the value of the discriminant $D = (27/4)R^2 + Q^3$; a positive discriminant, $D > 0$, corresponds to one real and two complex-conjugate eigenvalues, while its negative values, $D < 0$, corresponds to three distinct real eigenvalues. The line of $D = 0$ corresponds to three real eigenvalues, from which two are equal. The sign of the third invariant R can also help us to make a further classification; if $R < 0$, then the real part of two of the eigenvalues will be less than zero and its corresponding critical points can be classified as stable, while for $R > 0$ the sign of real parts of two of the eigenvalues is positive and the critical points would be attributed to an unstable topology [66, 48]. Figure 2.10 shows the various topologies that can occur in an incompressible flow based on these classifications (for further details, the reader is referred to Chong, Perry, and Cantwell [64]).

Figure 2.11 shows the Q–R plots corresponding to different shear rates. When there is no shear present, the plot shows a shape similar to the tear-drop shape (along second and fourth quadrants) repeatedly observed in turbulent flows that is considered a universal characteristics of small-scale motions of turbulence [2, 66, 67, 48]; however, it should be noted that the magnitiude of Q and R in Figure 2.11 indicates that the flow in the suspension is dominated mostly by large-scale motions while in the turbulent flows, fine-scale motions are an essential part of the flow. Imposing the shear flow as appears suppresses the smaller-scale

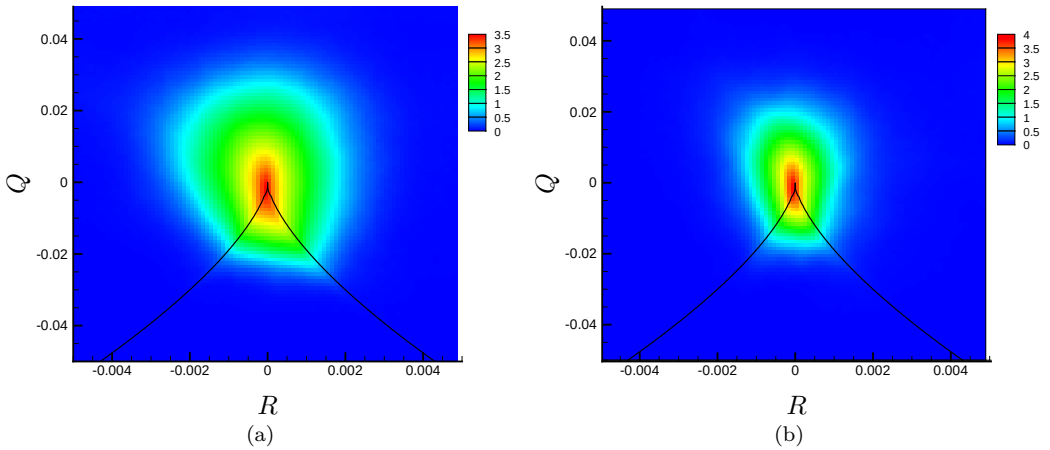

Figure 2.11: Q–R plots for different shear rates: (a) $S = 0$, and (b) $S = 0.1$.

fluctuations further. For the case corresponding to the two-dimensional instabilities there are no small-scale gradients as expected and the Q–R plot is focused essentially close to the origin. Note that because of the extreme variations of number density that occur in the Q–R plots, the logarithm of values of the density functions is used here as well as in the rest of density plots. Figure 2.11 shows that there is a slightly higher tendency towards the second and fourth quadrants. As described in Figure 2.10, these two quadrants correspond to the *Stable focus-stretching* and *Unstable node-saddle-saddle* topologies, respectively.

Because of the fact that all the eigenvalues of the strain-rate tensor are real due to its symmetry, in the Q_s–R_s plane, classifications with only negative discriminant $D_s = (27/4)R_s^2 + Q_s^3 \leq 0$ can be obtained. It can be further shown that each ratio of eigenvalues of the strain-rate tensor ($\alpha \geq \beta \geq \gamma$) can be mapped onto a line in the Q_s–R_s plane [2]. If $a = \beta/\alpha$, then

$$R_s = (-Q_s)^{3/2} a(1+a)(1+a+a^2)^{-3/2}, \tag{2.35}$$

in which $Q_s \leq 0$. Figure 2.12 shows that there is a slight tendency to the fourth quadrant, which corresponds to a saddle-saddle unstable node, and also to a positive intermediate rate of strain eigenvectors. It seems that shear damps this tendency, making the shapes more symmetric with regard to the $R_s = 0$ line. The lines on the figures correspond to different ratios of strain-rate eigenvalues. Ashurst et al. [50] reported that the ratio of the eigenvalues $\alpha : \beta : \gamma$ follow the line of $3 : 1 : -4$ while Soria et al. [2] and Blackburn et al. [66] reported a higher tendency towards ratio of $1 : 1 : -2$. Our results do not show a perfect match to either of these two lines; however, there is a slight tendency of the tail of the denser regions to follow the $3 : 1 : -4$ line and for points farther from the origin, a slight tendency towards the line of $1 : 1 : -2$ can be observed.

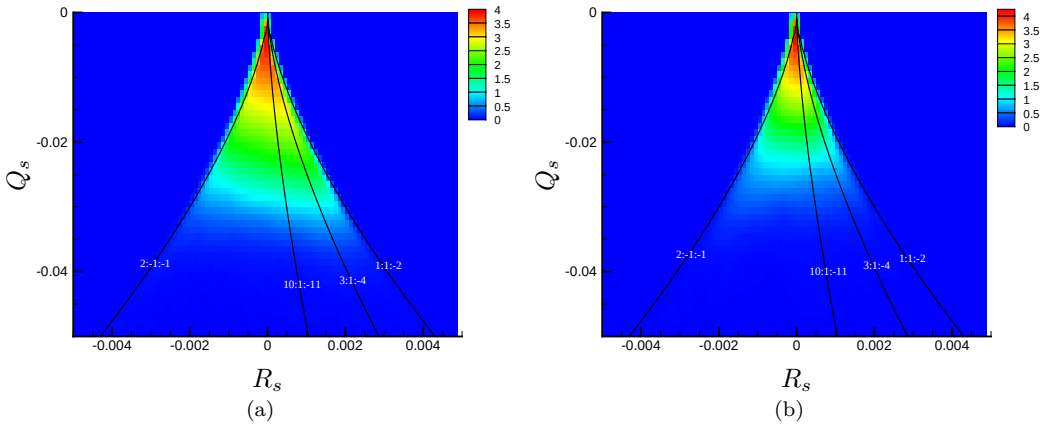

Figure 2.12: Q_s–R_s plots for different shear rates: (a) $S = 0$, and (b) $S = 0.1$.

But as will be discussed later, on average it seems that in the flow under study here, the intermediate rate of strain eigenvector is one order of magnitude smaller than both stretching and compressive components. For the cases corresponding to the three-dimensional instabilities, it will be shown later that on average, there seems to be a ratio of $10 : 1 : -11$ between the eigenvalues of the strain-rate tensor that is also shown in the Q_s–R_s plots here.

The mechanical kinetic energy dissipation as a result of viscous friction can be attributed to Q_s as $\Phi = 2\nu \mathbf{E}_{ij}\mathbf{E}_{ij} = -4\nu Q_s$, in which ν is the kinematic viscosity of the fluid. Therefore, negative values of Q_s correspond to positive kinetic energy dissipation, while Q_w is proportional to the enstrophy density $(w_i w_i/2)$ [2]. Figure 2.13 shows the relative importance of straining and rotation in the flow. Points, which lie near the Q_w axis are in nearly pure solid-body rotation, while points, which lie near the $-Q_s$ axis have motions that are nearly pure straining. Data that falls on the 45° line through the origin represents points in the flow with high dissipation accompanied by high vorticity. Such points are consistent with the picture of a *local vortex sheet*, where most of the strain is dominated by the velocity gradients within the sheet . For zero shear rate case, the straining seems to be the dominant mechanism while increasing the shear rate decreases the magnitude of straining to a point where almost none of these two mechanisms are present. Figure 2.13 suggests that the points with the highest dissipation are associated with comparably strong vorticity, i.e. they lie along the 45° axis; it also shows that there is no solid-body-like rotation and all vortical structures are accompanied by high dissipation that is in fact expected since the flow is essentially a viscous dominated flow. However, in turbulent flows purely vortical structures with small rates of dissipation are quite common.

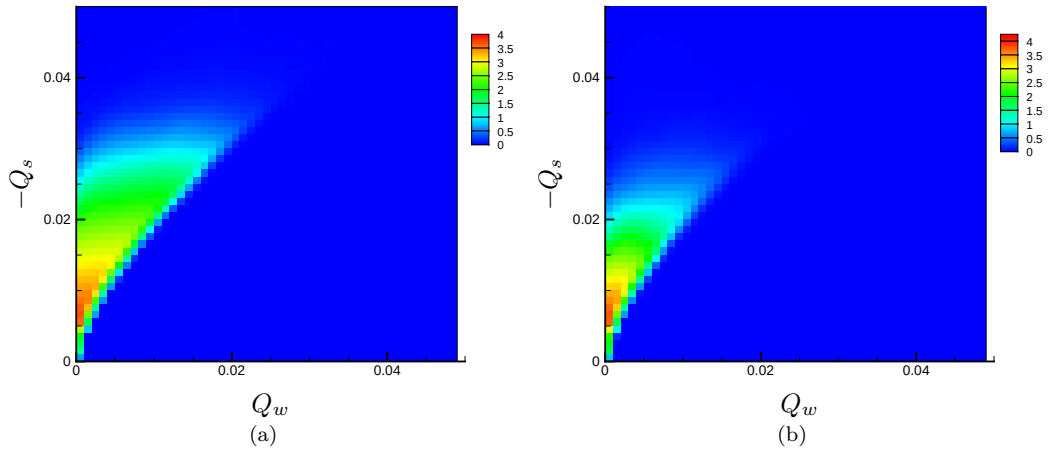

Figure 2.13: Q_s–Q_w plots for different shear rates: (a) $S = 0$, and (b) $S = 0.1$.

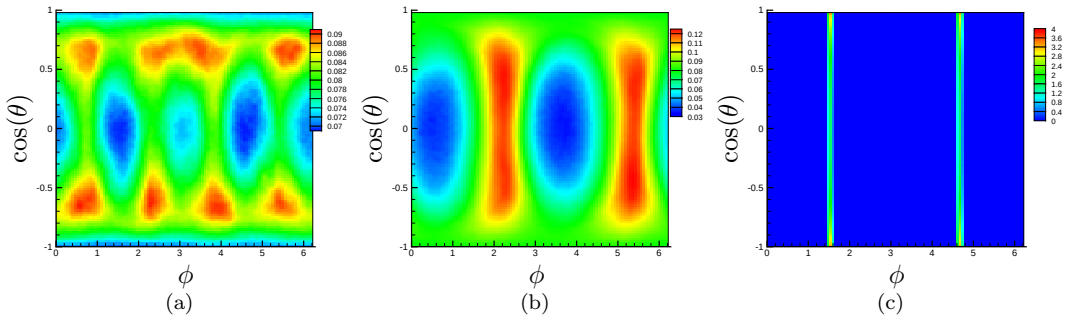

Figure 2.14: Joint probability distribution function of the concentration gradient angles for different shear rates: (a) $S = 0$, (b) $S = 0.1$, and (c) $S = 0.14$.

2.5.4 Joint probability distribution functions (JPDFs)

We now consider the spatial orientation distribution of different flow structures. As Figure 2.1 shows, the angle pair of $(\phi, \theta) = (0, \pi/2)$ points in the mean shear flow direction. Therefore, the orientation of a vector in the field can be determined with this angle pair. Using the joint probability distribution of this angle pair, we can further determine the most probable orientation of a given vector field. Due to the inherent bias that exists, θ angle is represented as $\cos(\theta)$ so that the natural bias towards the equator of the sphere can be overcome.

Figure 2.14 shows the probability distribution of the concentration gradient angles. For the zero-shear-rate case, there is almost no preferred direction. Note that the peaks and valleys that appear in this case are very close in magnitude and the slight variations observed in the plot can be attributed to the square shape of the computational domain. For the intermediate shear strengths, there is a tendency of aligning towards

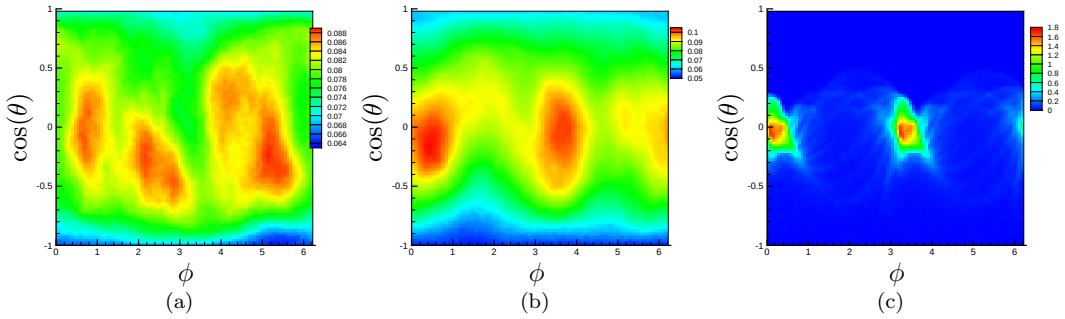

Figure 2.15: Joint probability probability function of vorticity vector angles for different shear rates: (a) $S = 0$, (b) $S = 0.1$, and (c) $S = 0.14$.

$\phi = 3\pi/4, \pi + 3\pi/4$, while in θ there is a wide variation symmetric about the shear plane. This distribution suggests that the concentration isosurfaces are oriented towards $\phi = \pi/4, \pi + \pi/4$, which is the direction of strongest stretching, and is in fact the same as what we observed from the concentration isosurfaces (Figure 2.8). As the instabilities become two-dimensional for $S = 0.14$, it seems that the peaks move towards $\phi = \pi/2, 3\pi/2$, suggesting that the concentration field is aligned in the flow direction ($\phi = 0, \pi$); this alignment is in fact what we have observed earlier from the concentration isosurfaces plots. The distribution in θ also shows that the gradient vector moves towards the z axis for the 2D instability case; this trend becomes more clear as we increase shear further and reach the 1D instability case (for $S = 0.2$) where there are gradients only in the z direction (i.e. perpendicular to the shear plane). Note that the contour levels change as shear increases; this change is because the distribution is more uniform without shear flow and it becomes increasingly concentrated as shear strength increases.

Figure 2.15 shows the probability density function of angles of vorticity vector for different shear rates. Similar to the concentration gradient vector, there seems to be no preferred direction in the case without shear. Adding shear seems to orient the vorticity axis towards $\phi = \pi/8, \pi + \pi/8$ while θ varies almost symmetrically about $\theta = \pi/2$ (i.e. shear plane). Increasing shear further shifts the vorticity towards the shear plane (i.e. $\theta = \pi/2$) and shear flow direction (i.e. $\phi = \pi/16, \pi + \pi/16$). Beyond this shear rate, there are no vortical structures present in the flow. Comparing Figures 2.14 and 2.15, it seems that the vorticity vectors are almost aligned with the concentration field. This alignment suggests that the concentration isosurfaces are actually vortex tubes that can be clearly observed in the 2D instability case, in which vortex tubes are uniform and aligned in shear flow direction (x). It should also be noted that as the strength of the shear flow increases and oscillations become damped, the strength of the vortical structures also decreases. Nevertheless, it should be mentioned that the straining mechanism becomes weaker with shear as well, as

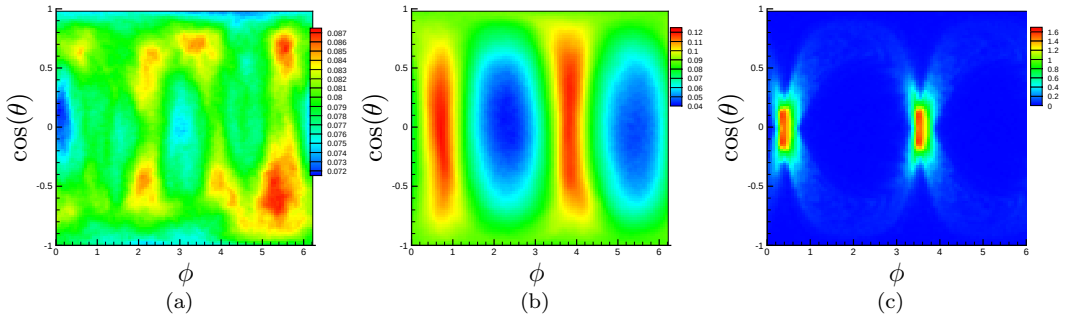

Figure 2.16: Joint probability distribution function of the director field angles for different shear rates: (a) $S = 0$, (b) $S = 0.1$, and (c) $S = 0.14$.

shown in Figure 2.13.

Figure 2.16 shows JPDF of the angles of the particle director field $\left(\mathbf{n}(\mathbf{x}, t) = \int_\Omega \mathbf{p}\mathbf{\Psi}(\mathbf{x}, \mathbf{p}, t)\, \mathrm{d}\mathbf{p}\right)$ for different shear rates. As for the concentration gradient and the vorticity fields, it seems that there is no preferred direction when there is no shear present, but shear orients the particles in $\phi = \pi/4, \pi + \pi/4$, which is the same as that of the concentration field (Figure 2.16 (b)); distribution in θ seems to be symmetric with regard to the shear plane. Increasing shear further, shifts the peaks towards $\phi = \pi/8, \pi + \pi/8$, which has a $\pi/8$ angle with the concentration isosurfaces (Figure 2.16 (c)). Comparing this figure with the previous two figures for the concentration gradient and the vorticity vectors, a picture of the flow can be suggested; it seems that the particles swim almost parallel to the axis of vortex tubes; therefore, stretching / compressing them. This phenomenon will in turn affect the concentration gradient, which is perpendicular to the vortex axis. However, as the flow considered here is not a vorticity dominated flow, such a simplistic description without considering straining mechanism may not be accurate. In the next sections, as we analyze the alignment of flow structures relative to each other and also with respect to the eigenvectors of the strain tensor, we can come up with a more detailed picture of the flow characteristics.

2.5.5 Alignment with the strain-rate eigenvectors

In the turbulent flow literature, it has been frequently noted that a seemingly universal behavior of turbulence is alignment of the vorticity vector with the eigenvector associated with the intermediate eigenvalue of the strain-rate tensor (β), and β is mostly positive indicating the extensional nature of the intermediate eigenvector. Moreover, it is reported that scalar gradient fields are aligned with the most compressive strain [50, 48]. In this section we analyze the alignment of the flow structures with the strain-rate eigenvectors; this investigation allows us to further compare the characteristics of the flow under study with turbulent

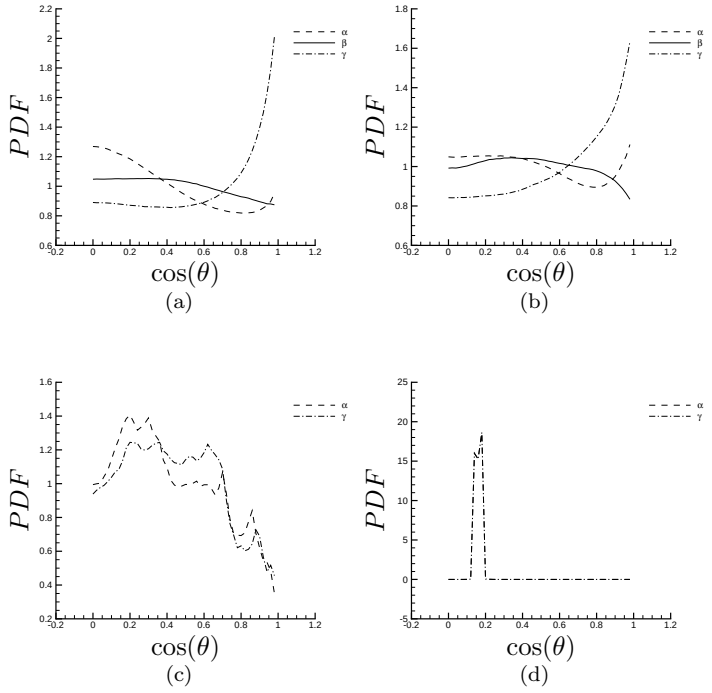

Figure 2.17: Alignment of the concentration gradient with the strain-rate eigenvectors for different shear rates: (a) $S = 0$, (b) $S = 0.1$, (c) $S = 0.14$, (d) $S = 0.2$.

flows and also inspect how the straining mechanism orients the structures.

Figure 2.17 (a, b) shows that the concentration gradient is aligned with the most compressive eigenvector for the cases corresponding to three-dimensional instabilities (i.e. $S = 0, 0.1$), there does not seem to be any considerable alignment with the intermediate eigenvector, but it seems that the concentration gradient has a higher probability of being normal to the most stretching eigenvector when there is no shear flow. For the 2D instability case, it seems that the alignments change completely; first, it should be noted that for this case, the strain-rate tensor has just two eigenvalues of the same magnitude, but opposite signs while the intermediate eigenvalue is zero. Figure 2.17 (c) suggests that the concentration gradient angle with both stretching and compressive eigenvectors has a wide range and at its peak varies between $\pi/4$ to $3\pi/8$. For the 1D instability case, Figure 2.17 (d) suggests that the concentration gradient is almost normal to both stretching and compressive eigenvectors (it has a fixed angle of $3\pi/8 + \pi/16$). The isosurfaces shown before in Figure 2.8, suggest that in this case, the gradients occur only in the z direction; a closer look at the velocity field reveals that there is a rather weak jet-like fluid motion in the shear plane. It should be noted that in this case, there are no vortical structures present in the flow and all the motion consists of jets of fluid going up and down in the shear plane. This observation suggests that all the stretching and compression

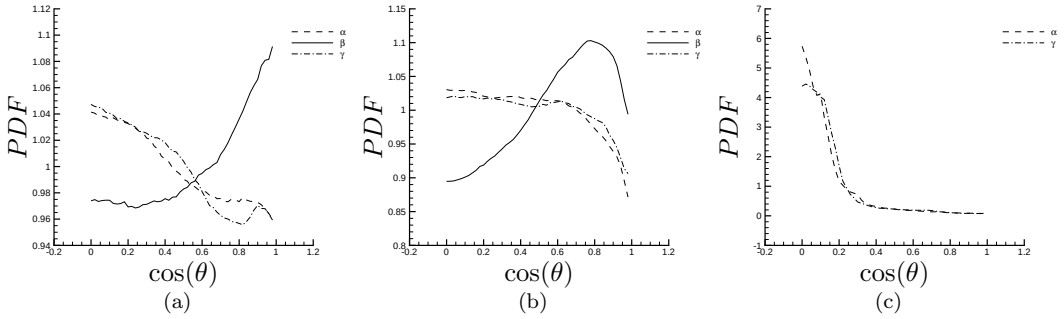

Figure 2.18: Alignment of vorticity vector with the strain-rate eigenvectors for different shear rates: (a) $S = 0$, (b) $S = 0.1$, (c) $S = 0.14$.

occurs in the shear plane and the concentration gradient is normal to this plane.

Figure 2.18 (a) shows that the vorticity has a tendency to be aligned with the intermediate eigenvector and be perpendicular to both stretching and compressive eigenvectors when there is no shear flow present. In turbulent flows, it has been considered a universal behavior for the vorticity vector to be aligned with the intermediate eigenvector; the same trend can be observed in Figure 2.18 for the 3D instability cases, but it should be noted that this alignment is not significant in the flow studied here. For the intermediate shear strength ($S = 0.1$), almost the same behavior can be observed except that the intermediate eigenvector and vorticity are not completely aligned and seem to have a fixed angle of $3\pi/16$ at the peak of the density function. The angle of the vorticity with the stretching and compressive eigenvectors however ranges from $\pi/2$ to $\pi/4$ at the density function's peak. For the 2D instability case, the vorticity seems to be normal to both the stretching and compressive eigenvectors.

The alignment of the director field with the strain eigenvectors is considered in Figure 2.19. It shows that the director field is aligned with the most stretching and normal to the most compressive eigenvectors for the 3D instability cases (Figure 2.19 (a,b)); however, there does not seem to be any specific relation with the intermediate eigenvector. For the 2D case (Figure 2.19 (c)), the director field seems to be almost normal to both stretching and compressive eigenvectors with a fixed angle of $7\pi/16$. In the 1D case (Figure 2.19 (d)), this alignment becomes more peaked and the angle is shifted to $3\pi/8$.

Now, considering all the alignments discussed above, we might be able to draw a picture of the flow. For the case without shear flow, it seems that particles swim in the most stretching direction; hence, creating a concentration gradient normal to it in the most compressive direction. The vorticity has a tendency to be aligned with the intermediate eigenvector and therefore, normal to the plane consisting of both compressive and stretching eigenvectors. For the moderate shear strengths where we still have 3D instabilities (i.e. $S =$

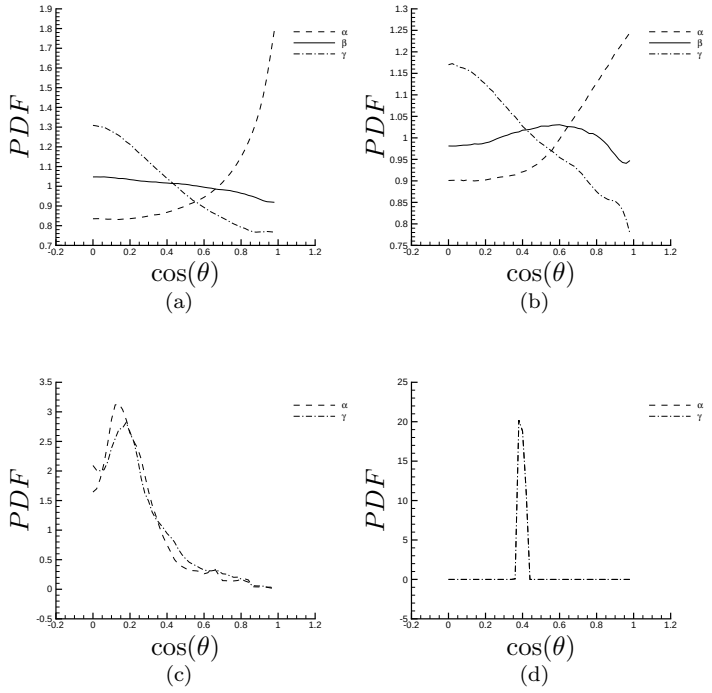

Figure 2.19: Alignment of the director field with the strain-rate eigenvectors for different shear rates: (a) $S = 0$, (b) $S = 0.1$, (c) $S = 0.14$, (d) $S = 0.2$.

0.1), the alignments with the strain-rate eigenvectors seem to be generally the same as in the case without shear flow; however, the vorticity seems to have an angle of $3\pi/16$ with the intermediate eigenvector at the density function's peak; its angle with both compressive and stretching eigenvectors also seem to vary between $\pi/2$ and $\pi/4$ at the density function's peak. It should be noted that as shear rate increases, the strength of the vortical structures decreases; this decline can be attributed to the tendency of shear flow to align all the structures in the flow direction. In the case corresponding to the 2D instabilities (i.e. $S = 0.14$), it seems that both the vorticity vectors and the director fields are almost normal to the plane consisting of compressive and stretching eigenvectors; the director field seem to have an angle of $7\pi/16$ with this plane; the concentration gradient on the other hand seems to be in the plane of the eigenvectors with its angle with them varying between $\pi/4$ to $7\pi/16$. As we will show later, there is no stretching or compression along the vortex axis for this case, that is consistent with having the vortex axis normal to the plane consisting of stretching and compressive eigenvectors. The main difference between 2D and 3D instability cases, then would be the fact that the director field is not aligned with the stretching eigenvector, but almost normal to it.

Figure 2.20 analyzes the alignment of the director field with the concentration gradient and also the

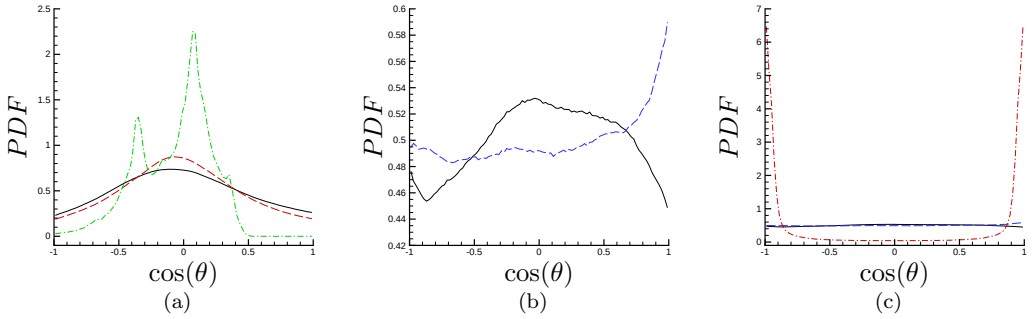

Figure 2.20: Alignment of the director field with (a) concentration gradient, and (b), (c) vorticity vector. $S = 0$: solid line, $S = 0.1$: dashed line , and $S = 0.14$: dash dotted line.

vorticity field. As the above discussion showed, we observe that the director field tends to be normal to the concentration gradient for the cases corresponding to the 3D instabilities; but for the 2D instabilities, as mentioned earlier, the peaks are a little deviated from $\pi/2$ and are not symmetric with respect to it either (Figure 2.20 (a)). Part (b) of the Figure 2.20 also suggests that there is no specific trend of alignment between the director field and the vorticity field for the 3D instability cases; however, it shows a slight tendency of the two fields being normal to each other when there is no shear flow, and being aligned when there is a moderate shear imposed. This alignment seems a little surprising, but it should be noted that when there is no shear present, there is no preferred direction for the flow structures as discussed before; therefore, there really is not any specific aligning between the director and vorticity fields. Adding shear; however, tends to slightly align the director and vorticity fields. Part (c) of the Figure 2.20, shows the same data as part (b) except for that it also includes the 2D instability case (i.e. $S = 0.14$); as it appears, when plotted together with the 3D instability cases, the 2D case shows a significant alignment between the director and vorticity fields while the cases corresponding to 3D instability cases (i.e. $S = 0, 0.1$) show no considerable alignment between the two fields.

2.5.6 Autocorrelation functions

In this section, we investigate the autocorrelation of different fields to obtain a more clear picture of the flow structures.

Figure 2.21 shows the correlation function of the concentration field in the shear plane (x-y) for different shear rates. As expected, it shows that the correlation function is completely symmetric with respect to both x and y when there is no shear imposed; but as shear flow is imposed, the concentration field becomes aligned in the most stretching direction (i.e. $\phi = \pi/4$). For the case of 2D instabilities, as shown earlier, the

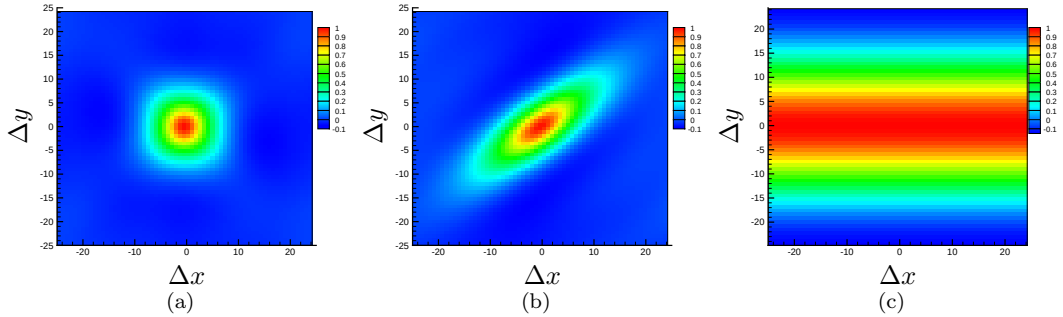

Figure 2.21: Concentration field autocorrelation function in x-y plane for different shear rates: (a) $S = 0$, (b) $S = 0.1$, and (c) $S = 0.14$.

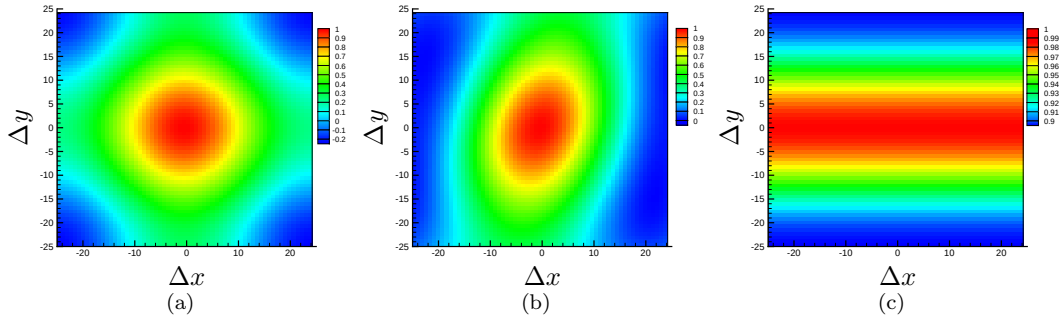

Figure 2.22: Velocity field autocorrelation function in x-y plane for different shear rates: (a) $S = 0$, (b) $S = 0.1$, and (c) $S = 0.14$.

structures are uniform and perfectly correlated in the flow direction; therefore, in the shear plane, there is only a wave-like variation in y direction. As the instabilities become 1D for higher shear rates, the structures become uniform in the shear plane and gradients are present only in the direction perpendicular to the shear plane; therefore, the flow is completely correlated in the shear plane.

Figure 2.22 shows the correlation function of the velocity field in the shear plane (x-y). As for the concentration field, the correlation function is completely symmetric when there is no shear flow; the shear flow again breaks this symmetry making the correlation inclined towards the most stretching direction; however, the velocity field's inclination towards the 45° is not as strong as for the concentration field. For the 2D instability case, as explained, the variations occur only in y direction and the correlation function looks quite similar to that of the concentration field.

Figure 2.23 shows essentially the same behavior for the director field as for the concentration field, i.e. no preferred direction without shear flow, alignment towards the most stretching direction for the intermediate shear strength, and wave-like variation in the y direction for the 2D instability case.

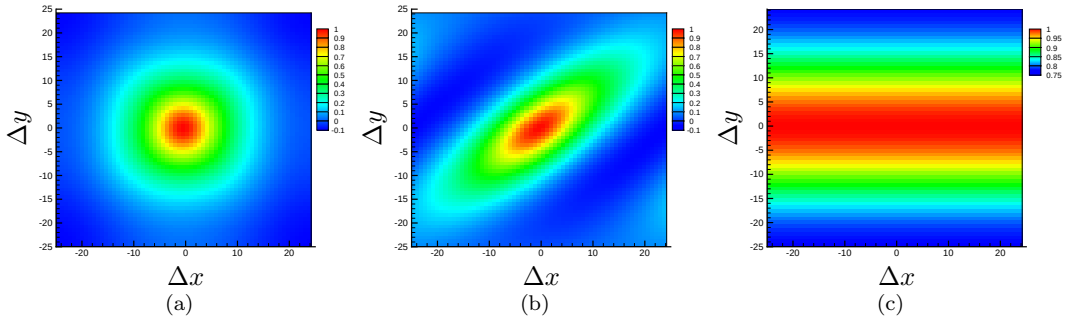

Figure 2.23: Director field autocorrelation function in x-y plane for different shear rates: (a) $S = 0$, (b) $S = 0.1$, and (c) $S = 0.14$.

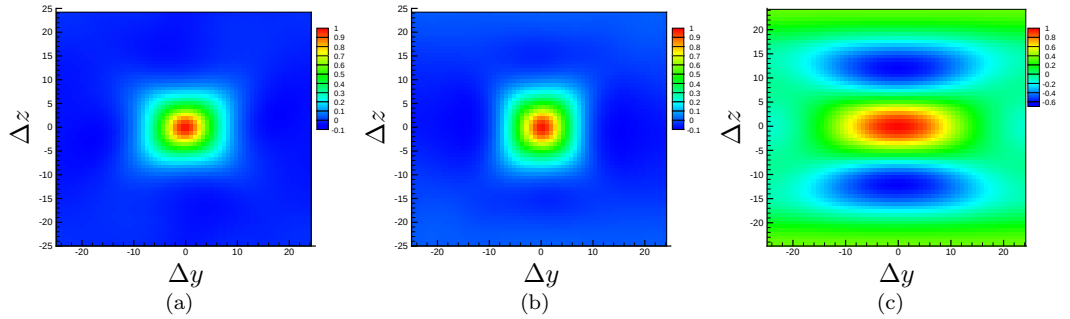

Figure 2.24: Concentration field autocorrelation function in y-z plane for different shear rates: (a) $S = 0$, (b) $S = 0.1$, and (c) $S = 0.14$.

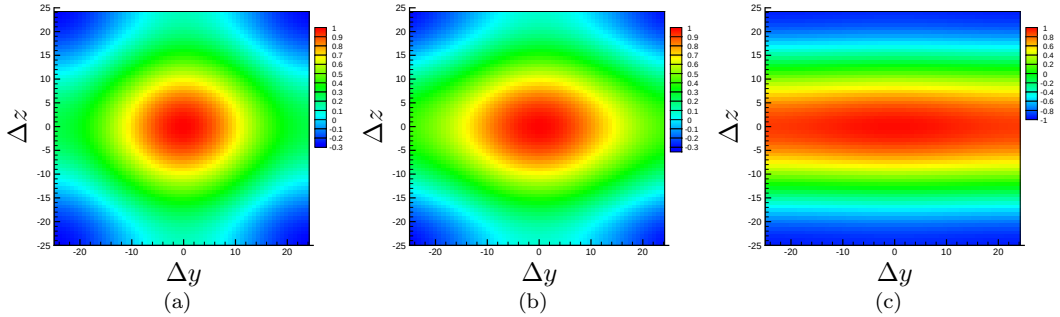

Figure 2.25: Velocity field autocorrelation function in y-z plane for different shear rates: (a) $S = 0$, (b) $S = 0.1$, and (c) $S = 0.14$.

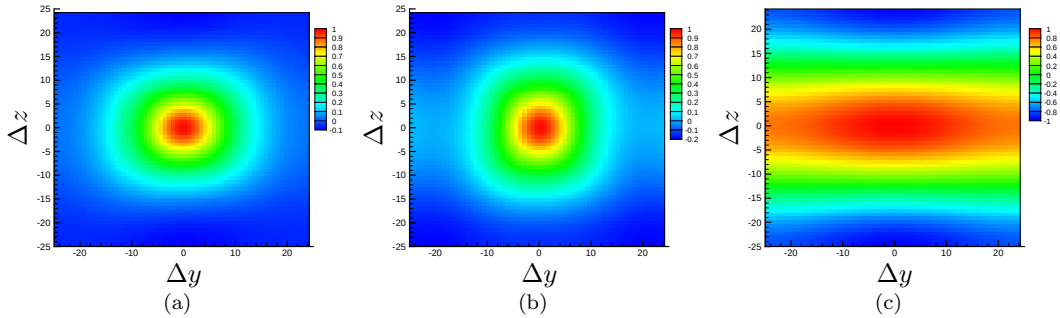

Figure 2.26: Director field autocorrelation function in y-z plane for different shear rates: (a) $S = 0$, (b) $S = 0.1$, and (c) $S = 0.14$.

Figure 2.24 shows the correlation function of the concentration field in the plane perpendicular to the shear plane, i.e. y-z. There seems to be no preferred direction for zero-shear-rate and intermediate-shear-rate cases; but for the $2D$ instability case, it suggests that there is a slightly stronger correlation in the y than in the z direction. Since the gradients in the z direction become damped the last, the correlation is weakest in this direction.

The same kind of behavior as the concentration field can be observed in the autocorrelation functions of the velocity field, as shown in Figure 2.25. However, the correlations in the velocity field seem to be stronger than that of the concentration field. In particular, the correlation in the y direction seems to be even stronger, suggesting that the shear flow damps the fluctuations in the velocity field faster than that of the concentration field.

The director field seems to have a tendency to be more correlated in the y direction when there is no shear flow present, as represented in Figure 2.26 (a); however, surprisingly this tendency weakens for the intermediate shear strengths, making the correlation function more symmetric with respect to both y and

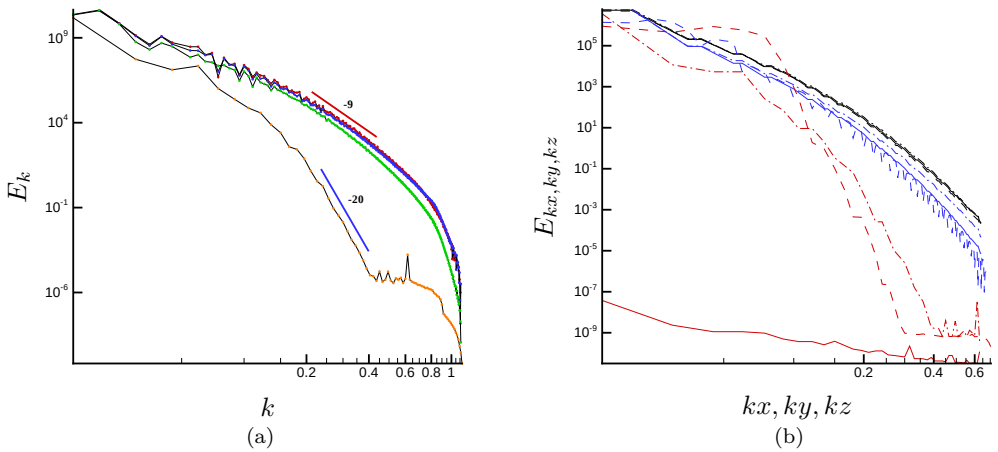

Figure 2.27: Energy spectrum for different shear rates. (a) total energy; from top to bottom: $S = 0$, $S = 0.05$(included just in the total energy), $S = 0.1$, $S = 0.14$. and (b) one-dimensional spectrum; from top to bottom: $S = 0$ (black color), $S = 0.1$ (blue color), $S = 0.14$ (red color). Solid line: E_{kx}, dashed line: E_{ky}, dash-dotted line: E_{kz}.

z directions (Figure 2.26 (b)). As the flow becomes two-dimensional at higher shear rates, the gradients in the y direction become further damped and the director field tends to be almost completely aligned in the y direction (Figure 2.26 (c)).

2.5.7 Energy spectrum E_k

One of the fundamental characteristics of the turbulent flows is the distribution of kinetic energy over a wide range of length scales. The energy spectrum of three-dimensional turbulence follows $E(\mathbf{k}) \propto k^{-5/3}$, while for a two-dimensional turbulence we have $E(\mathbf{k}) \propto k^{-3}$. In order to realize how different scales contribute to the flow under study, we also calculate the kinetic energy spectrum of the flow.

Figure 2.27 (a) suggests that in the flow studied here, the slope is much higher than that of turbulent flows, indicating that the flow is dominated by large-scale motions; also as shear increases, the slope increases further verifying that as discussed before shear damps the smaller-scale fluctuations. Figure 2.27 (b) further shows the one-dimensional energy spectrum of the flow for different shear rates. It shows how the flow energy is distributed in different directions. As appears, when there is no shear present, the distribution in all three directions is the same since there is no preferred direction, but as shear is imposed, there seems to be a deviation. For $S = 0.1$, although the spectrum is different, directions are still very close to each other, the energy in the direction perpendicular to the shear plane seems to be highest and in the y direction seems to be the lowest. The reason why the energy in z is the highest can be attributed to the fact that instabilities

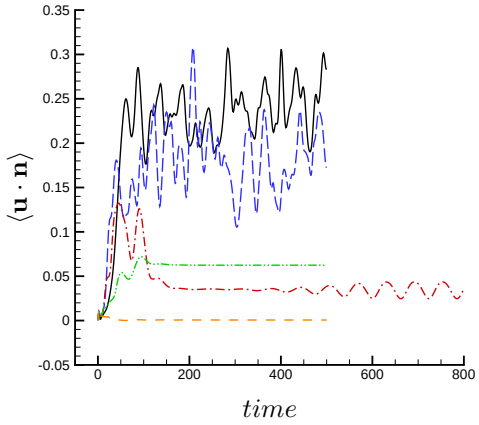

Figure 2.28: Spatially-averaged contraction for different shear rates. Solid line: $S = 0$, long-dashed line: $S = 0.1$, dash-dotted line: $S = 0.14$, dash-dot-dotted line: $S = 0.2$, dashed line: $S = 0.3$.

in this direction become damped the last, meaning that in the presence of shear flow, the instabilities in this direction are the strongest. For the 2D instability case, flow is uniform in the flow direction and as expected the energy in x is the lowest; the energy in z direction again seems to be higher in the intermediate scales.

2.5.8 Flow evolution in time

We now consider the evolution of some of the flow characteristics in time, that helps us understand how the flow develops over time and as will be shown reaches a statistically steady state in long times.

Spatially-averaged contraction of the velocity and director fields

In order to investigate the correlation between the director field $\mathbf{n}$ and the velocity field $\mathbf{u}$, we use the spatially-averaged contraction of these two fields, defined as

$$\langle \mathbf{u} \cdot \mathbf{n} \rangle = \frac{1}{V} \int_V c(\mathbf{x}, t) \mathbf{u}(\mathbf{x}, t) \cdot \mathbf{n} \, \mathrm{d}\mathbf{x}. \tag{2.36}$$

Figure 2.28 shows that $\langle \mathbf{u} \cdot \mathbf{n} \rangle$, which is initially close to zero, grows to reach a plateau for all shear rates considered. This behavior suggests that the particles tend to align in the local disturbance flow and swim in the direction of the flow. While alignment with the flow is easy to anticipate since the particles align in the local shear according to Jeffery's Equation (2.4), the fact that they on average tend to swim in the direction of the local velocity was a priori unexpected. This preferred alignment and orientation result in an increase in the effective swimming velocity of the particles, a phenomenon already shown in some earlier works. The effect of the external shear on this alignment is interesting here. It appears that increasing

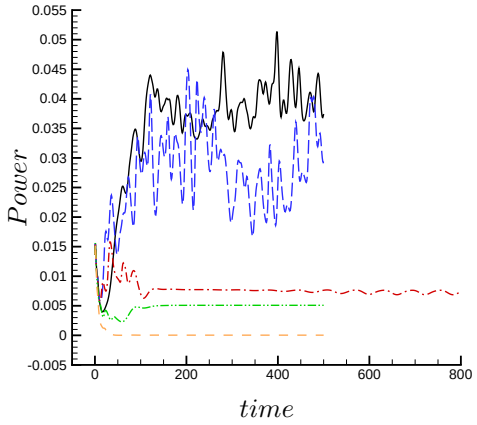

Figure 2.29: Active input power for different shear rates. Solid line: $S = 0$, long-dashed line: $S = 0.1$, dash-dotted line: $S = 0.14$, dash-dot-dotted line: $S = 0.2$, dashed line: $S = 0.3$.

shear while having a stabilizing effect on the flow, also decreases the alignment of the particles with the local disturbance flow. This trend stays valid until the instabilities become one-dimensional, in which case the alignment seems to be enhanced a little bit again. As shear increases further, all the instabilities become damped and the disturbance flow almost vanishes; that is why the alignment seems to go to zero for this case. However, it should be noted that the decreasing alignment of particles with the disturbance flow, in fact might be related to the decrease in magnitude of disturbance velocity with shear.

Active input power

Following Saintillan and Shelley [39], we can find an interesting interpretation of the dynamics in terms of input power generated by the swimming particles. Therefore, we define the local active power density as

$$p(\mathbf{x}, t) = -\alpha \int_{\Omega} (\mathbf{p} \cdot \mathbf{E} \cdot \mathbf{p})\, \Psi(\mathbf{x}, \mathbf{p}, t)\, \mathrm{d}\mathbf{p}, \tag{2.37}$$

from which we can also define the global input power as $P(t) = \int_{\Omega} p(\mathbf{x}, t)\, \mathrm{d}\mathbf{x}$. Figure 2.29 shows that the total input power injected by the particles into the fluid increases in time until it reaches a plateau over long times for the cases corresponding to three-dimensional instabilities; but for the two-dimensional and one-dimensional instabilities, it appears that the input power does not increase in time and reaches a plateau even lower than the initial perturbation values. Overall, it appears that the input power generated by the swimming particle decreases as the external shear increases and damps the instabilities. For the strongest shear rate considered here, i.e. $S = 0.3$, it appears that as there are no instabilities present, there is no disturbance flow either and the total injected power is in fact zero. This observation suggests that in strong

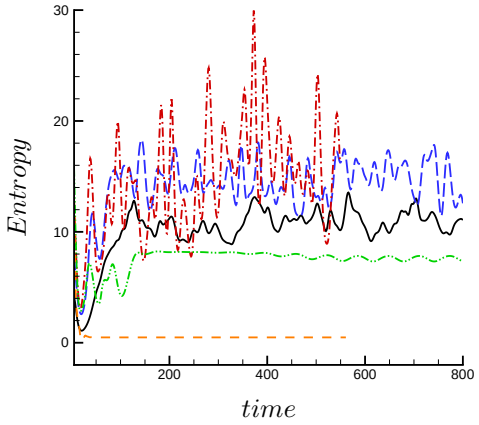

Figure 2.30: System entropy for different shear rates. Solid line: $S = 0$, long-dashed line: $S = 0.05$, dash-dotted line: $S = 0.1$, dash-dot-dotted line: $S = 0.14$, dashed line: $S = 0.5$.

shear flows, the particles essentially stop injecting power to the macro-scale flow and behave as a suspensions of passive particles in the presence of shear.

System entropy

Figure 2.30 shows the entropy of the system as defined in Section 2.2, and as expected it increases for the pusher particles, which are the case considered throughout this study. As Equation (2.17) suggests, the input power drives the increases in the fluctuations causing the system entropy to increase and reach a plateau at long times as well. The effect of shear on the system entropy is interesting; the entropy first increases by shear until it reaches a certain value (around $S = 0.08$ in our simulations); beyond this shear rate, the entropy of the system starts to decrease with shear and eventually as all the instabilities disappear and the flow becomes spatially uniform, we will have $\Psi = \Psi_0$ that results in a zero entropy as it appears to be the case for $S = 0.5$; note that the small non-zero value of the entropy for this case is due to the fact that still the flow contains very weak gradients. As the shear flow damps the small-scale fluctuations, it makes sense that the system entropy should decrease with shear; however, the initial growth of the entropy with shear cannot be explained in this frame.

Eigenvalues of strain-rate tensor

Figure 2.31 shows the eigenvalues of the strain-rate tensor where $\alpha \geq \beta \geq \gamma$. The sum of the eigenvalues is zero for incompressible flow. As this figure shows, in our simulations, α is always positive corresponding to the most stretching eigenvector of the strain-rate tensor while γ is always negative corresponding to the compressive component. β seems to be always close to zero having a positive (stretching) time average for

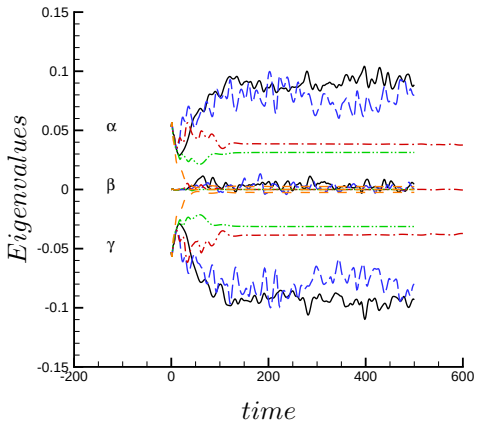

Figure 2.31: Eigenvalues of strain-rate tensor for different shear rates. Solid line: $S = 0$, long-dashed line: $S = 0.1$, dash-dotted line: $S = 0.14$, dash-dot-dotted line: $S = 0.2$, dashed line: $S = 0.3$.

both $S = 0$, and $S = 0.1$, which are the cases with three-dimensional instabilities while it becomes almost exactly zero for higher shear rates corresponding to two and one-dimensional instabilities. The property of β being positive on average observed in the 3D instability cases here is the same as that observed in turbulent flows [50, 48]. The magnitude of most stretching (α) and most compressive (γ) eigenvalues tend to decrease as shear rate increases, suggesting that the straining mechanism becomes weaker with shear rate. This behavior is consistent with the results of $Q_s - Q_w$ plots, which also suggested that both straining and vorticity dominated mechanisms become weaker with shear flow (Figure 2.13). For the 1D instability case (i.e. $S = 0.2$), as mentioned before, there are still jet-like fluid motions with no vorticity present in the shear plane that cause the flow to have non-zero compressive and stretching eigenvalues ($\alpha = -\gamma$). As shear increases further and the flow becomes spatially uniform, these eigenvalues also approach zero value, as presented in Figure 2.31 for $S = 0.3$.

Swirling strength, compactness, and stretching/compression

To analyze the swirling motions of the fluid in more detail, we use the swirling strength criterion developed by Zhou et al. [65]. It uses the imaginary part of the complex-conjugate eigenvalue of the velocity gradient $\nabla \mathbf{u}$ to identify vortices. When $\nabla \mathbf{u}$ has complex-conjugate eigenvalues, in a locally curvilinear coordinate system (y_1, y_2, y_3), spanned by the vectors (v_r, v_{cr}, v_{ci}), and moving with the local fluid velocity, the instantaneous

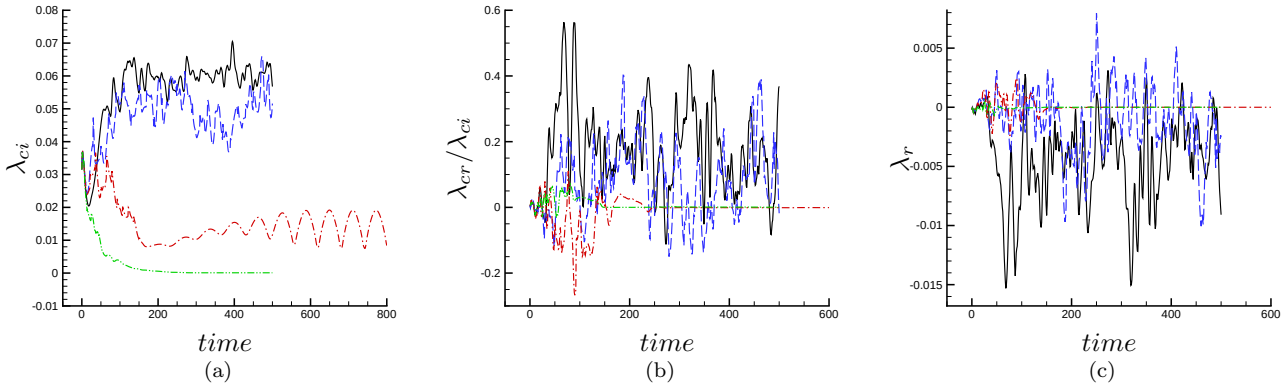

Figure 2.32: (a) Swirling strength: λ_{ci}, (b) orbital compactness: $\lambda_{cr}/\lambda_{ci}$, and (c) stretching/compression strength: λ_r, for different shear rates. Solid line: $S = 0$, dashed line: $S = 0.1$, dash-dotted line: $S = 0.14$, dash-dot-dotted line: $S = 0.2$.

streamlines can be defined as [68]

$$y_1(t) = y_1(0)e^{\lambda_r t}, \tag{2.38a}$$

$$y_2(t) = e^{\lambda_{cr} t}\left[y_2(0)\cos(\lambda_{ci}t) + y_3(0)\sin(\lambda_{ci}t)\right], \tag{2.38b}$$

$$y_3(t) = e^{\lambda_{cr} t}\left[y_3(0)\cos(\lambda_{ci}t) - y_2(0)\sin(\lambda_{ci}t)\right], \tag{2.38c}$$

where λ_r, v_r is the real eigen-pair and $\lambda_{cr} \pm \imath\lambda_{ci}, v_{cr} \pm \imath v_{ci}$ is the complex-conjugate eigen-pair of $\nabla\mathbf{u}$. Streamlines are the same as pathlines in a time frozen field, and t can be considered as a time-like parameter that evolves them. The flow swirls locally in the plane spanned by (v_{cr}, v_{ci}) and becomes stretched or compressed along the direction of v_r. The strength of a local swirling motion inside a vortex can be determined by λ_{ci}, which is called swirling strength. Moreover, the strength of stretching / compression can be determined through λ_r. Therefore, for a streamline to complete one revolution, it needs $2\pi/\lambda_{ci}$ time units. Now, consider two particles in the plane of vortex v_{cr}, v_{ci} that are initially separated by a distance r_0; after n revolutions of the vortex, the particles will have a distance r_f from each other that can be defined in terms of eigenvalues of $\nabla\mathbf{u}$ as [64, 68]

$$\frac{r_f}{r_0} = \exp(2\pi n \frac{\lambda_{cr}}{\lambda_{ci}}), \tag{2.39}$$

where the ratio $\lambda_{cr}/\lambda_{ci}$ is attributed to the spatial extent of the local spiraling motion, and is called inverse spiraling compactness. If we have a value of $\lambda_{cr}/\lambda_{ci} = 0$, then the vortex goes through a perfectly circular motion, while it would spiral outward, or inward, in the vortex plane for a positive, or negative, value of inverse spiraling compactness, respectively. Therefore, as suggested by Chakraborty et al. [68], for a point

to be considered inside a vortex core in an incompressible flow, the requirements are (i) $\lambda_{ci} \geq \epsilon$, and (ii) $-k \leq \lambda_{cr}/\lambda_{ci} \leq \delta$, where ϵ, δ, and k are positive thresholds whose values depend on the desired vortex strength, orbital compactness of the vortex core, and orbital compactness along the vortex axis, respectively.

Furthermore, using the above definitions, the second invariant of the velocity gradient can be written as

$$Q = \lambda_{ci}^2(1 - 3(\frac{\lambda_{cr}}{\lambda_{ci}})^2). \tag{2.40}$$

indicating that the $Q > 0$ criterion, which we used to identify the vortical structures in section 2.5.2, can be corresponded to the regions with local swirling $\lambda_{ci} > 0$, where spiraling motions (inward or outward) are limited by $|\lambda_{cr}/\lambda_{ci}| < 1/\sqrt{3}$ [68].

Figure 2.32 (a) shows the spatially-averaged swirling strength (λ_{ci}) as a function of time. It gives a qualitative description of the mean flow. As it appears, λ_{ci} decreases with shear rate until it becomes exactly zero for the case corresponding to the one-dimensional instabilities. Therefore, this figure suggests that shear flow weakens the vortical structures that is reasonable knowing that it tends to align all the structures in the flow direction, removing all swirling motions as a result. This observation is also consistent with the predictions of $Q_s - Q_w$ plots already discussed and represented in Figure 2.13.

Figure 2.32 (b) shows the spatially-averaged *inverse spiraling compactness* ($\lambda_{cr}/\lambda_{ci}$) as a function of time. For $S = 0$, $S = 0.1$, the average is mostly positive suggesting spiraling outward while for the two-dimensional instability case ($S = 0.14$), the ratio becomes zero, suggesting a perfectly circular path for the vortex tube. For higher shear rates, it is still zero, but for these cases as shown earlier there are no vortical structures present so this quantity becomes meaningless for them.

Figure 2.32 (c) shows the spatially-averaged λ_r, which determines the strength of stretching or compression along the vortex axis. When there is no external shear flow present, it appears that λ_r is negative on average, suggesting a compressive flow along the vortex axis. But as shear flow is imposed, the value of λ_r increases showing both compressive and stretching mechanisms play a role. For the case of $S = 0.14$ corresponding to two-dimensional instabilities, $\lambda_r = 0$, suggesting that there is no stretching or compression along the axis of vortex tubes present in the flow that could be anticipated knowing that the vortical structures remain perfectly circular for this shear rate. For higher shear rates, this value remains zero, but as for the orbital compactness, there is no vortical structure present in the flow and therefore, there is no meaning for λ_r in these cases. While it might be hard to describe the exact dynamics of the flow by looking just at the instantaneous streamlines when the instabilities are three-dimensional, for the two-dimensional case, we can in fact easily observe the vortex tubes, which are perfectly circular and do not become stretched or

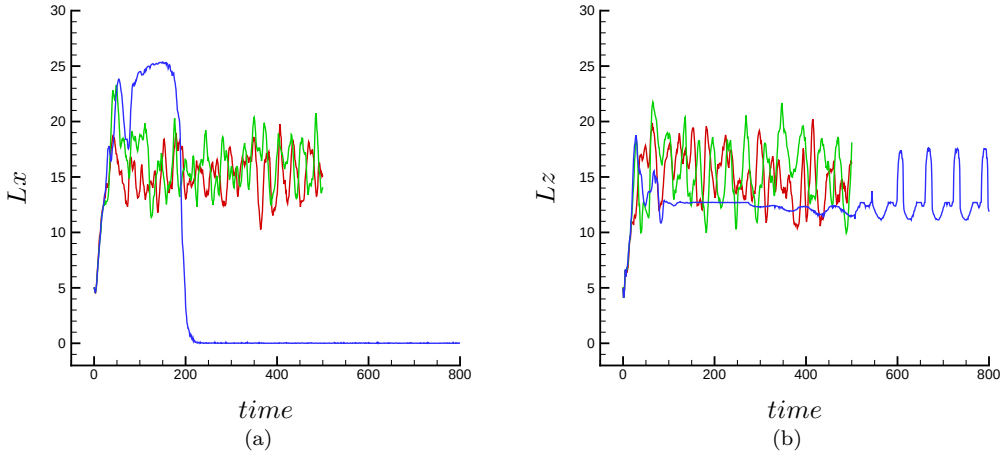

Figure 2.33: 1D Correlation length of the concentration field, (a) L_x, and (b) L_z; for $S = 0$: red line, $S = 0.1$: green line, $S = 0.14$: blue line.

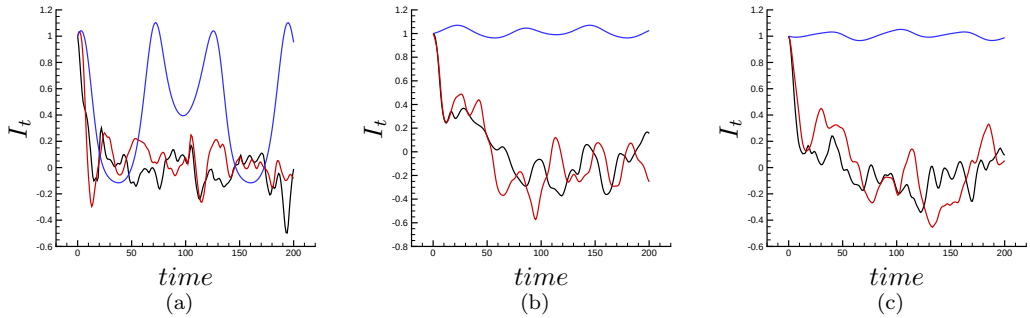

Figure 2.34: Temporal autocorrelation function for the (a) concentration field, (b) velocity field, and (c) director field. Black line: $S = 0$, red line: $S = 0.1$, and blue line: $S = 0.14$.

compressed along their axis, as shown in Figure 2.9.

Correlation Length and Temporal Autocorrelation

Since the flow is dominated essentially by the large-scale motions of the box size, it is easy to anticipate that it should also be correlated on the size of the box. This correlation can be observed from the 2D plots of autocorrelation functions in Section 2.5.6. However, as the flow becomes 2D, it becomes perfectly correlated in the flow direction and as it becomes 1D, in the shear plane. This transition from three-dimensional instabilities to 2D instabilities turns out to cause interesting behavior in the correlation length of the concentration field. Figure 2.33 shows the 1D correlation length of the concentration field in (a) x direction and (b) z direction. In the flow direction, as expected when the flow is 3D, the velocity and director

fields are correlated on the box size; however, the correlation length of the concentration field seems to be on the scale of one-thirds of the box size. As the flow becomes 2D, it becomes perfectly correlated in the x direction resulting in a zero correlation length in this direction. For the z direction, the same behavior can be observed for the 3D cases, i.e. the velocity and director fields are correlated on the box size while the correlation length of the concentration field is on the scale of one-thirds of the box size. The 2D case also seems to be correlated on the same length scales in the z direction; the oscillations in the correlation length for this case become quasi-steady in time. The observed oscillation in the 2D case could be related to the presence of vortex tubes, which are aligned in the flow direction and disappear and re-appear again in a quasi-periodic fashion. All the flow properties appear to be correlated on the box size in the y direction, as expected (not included).

Figure 2.34 shows the temporal autocorrelation of different fields. It can help us understand how flow structures evolve in time and basically how long it takes for a structure to de-correlate in time. All the fields corresponding to the 3D instability cases, i.e. the concentration, velocity and director fields, seem to de-correlate in time very rapidly and in fact show anti-correlation after a while. However, the 2D instability case shows a quite different behavior. For this case, the concentration field initially seems to de-correlate in time as for the 3D case, just a little slower, but it becomes correlated with the initial field again over longer times. This behavior seems to occur repeatedly and it suggests that the flow is in fact in a quasi-steady state and shows a periodic behavior in time. The time period of this quasi-steady state seems to be almost 100 time units. The velocity field, and the director field for this case on the other hand seem to stay perfectly correlated in time. In fact, they also show the same kind of periodic oscillations in time, but they do not de-correlate and stay almost perfectly correlated in time.

2.5.9 Statistics

Velocity Statistics

In this section, we analyze the distribution of the velocity components; it helps us understand the fluid motion more clearly; it can also help us investigate the effect of shear on the fluid motion.

Figure 2.35 shows the distribution of velocity components for different shear rates. The u_x distributions is similar to a normal distribution for $S = 0$, and $S = 0.1$ that correspond to the 3D instability case and the distributions become more peaked as shear increases, but the distribution is completely different for the case of 2D instability (i.e. $S = 0.14$), in which it shows two symmetric peaks corresponding to non-zero velocities. The distribution of u_y is essentially the same as u_x except for that $S = 0$, and $S = 0.1$ distributions are closer to each other; the $S = 0.14$ distribution is broader for u_y. For the u_z distribution, the 3D instability

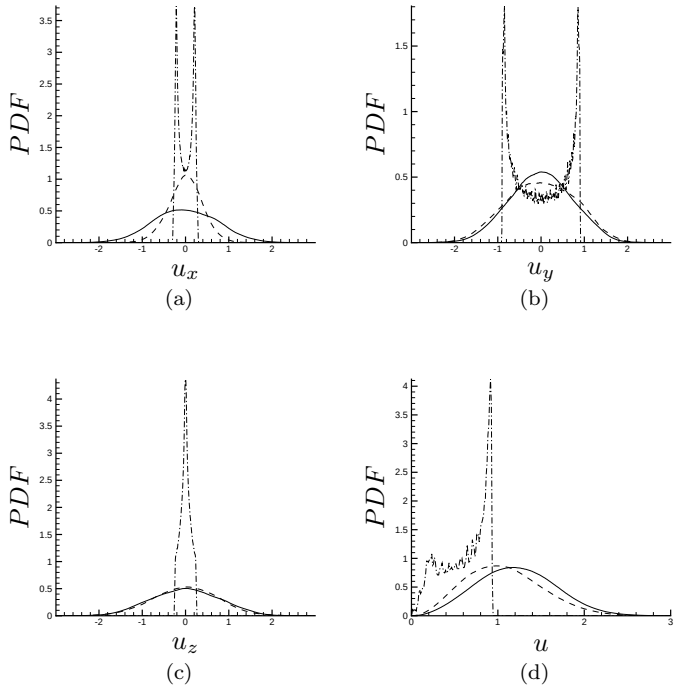

Figure 2.35: Probability distribution function of velocity components. Solid line: $S = 0$, dashed line: $S = 0.1$, dash-dotted line: $S = 0.14$.

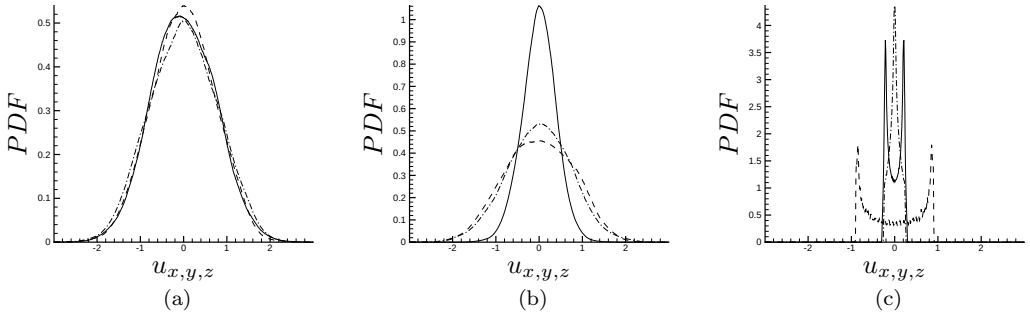

Figure 2.36: Probability distribution function of velocity components for (a) $S = 0$, (b) $S = 0.1$, and (c) $S = 0.14$. Solid line: u_x, dashed line: u_y, dash-dotted line: u_z.

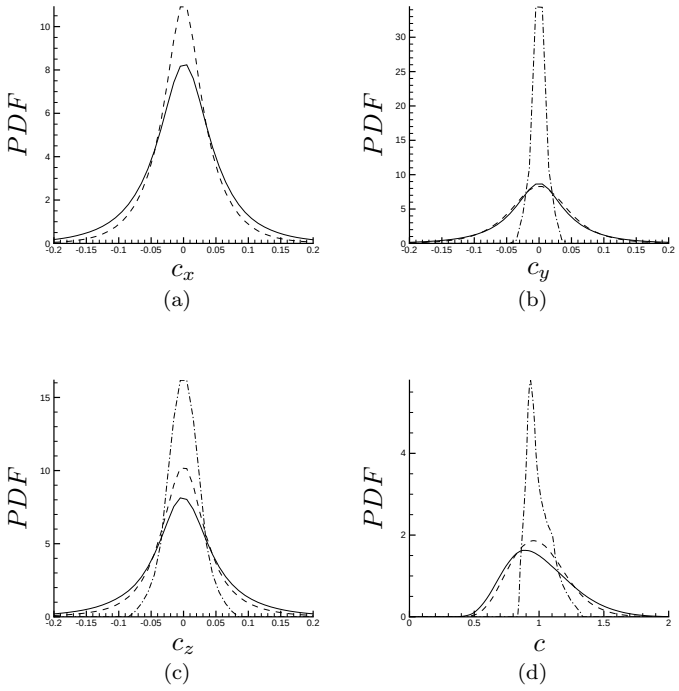

Figure 2.37: Probability distribution function of the concentration gradient components. Solid line: $S = 0$, dashed line: $S = 0.1$, dash-dotted line: $S = 0.14$.

cases are very close to each other again, but the $S = 0.14$ distribution becomes very peaked close to zero velocity. The total velocity distribution is also shown in Figure 2.35 (d); it seems that imposing the shear shifts the peak closer to the zero velocity; the distribution corresponding to the 2D instability case is shifted more towards zero velocity and is very peaked close to $u = 1$.

Figure 2.36 shows the distribution of different velocity components corresponding to different shear rates. It is essentially the same data as Figure 2.35, but now it is easier to compare how different velocity components behave in each shear strength. It clearly shows that for the case without shear flow, different velocity components behave the same way and have a normal distribution since there is no preferred direction; however, for $S = 0.1$, the u_x distribution is more peaked close to the zero velocity. For the case of 2D instability, it appears that both u_x and u_y have two symmetric non-zero peaks; the u_y distribution is wider; the u_z component is however very peaked around the zero velocity.

Density Field Statistics

Figure 2.37 shows the distribution of the concentration gradient components corresponding to different shear rates. The gradient in all directions seem to follow a normal distribution. The c_x, which is the gradient in

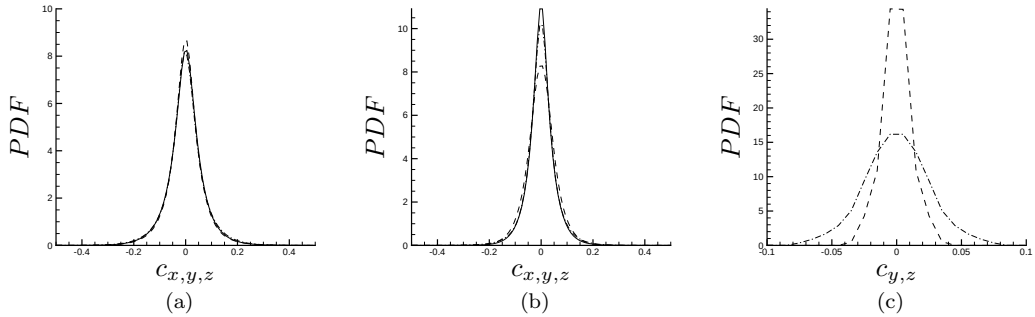

Figure 2.38: Probability distribution function of the concentration gradient components for (a) $S = 0$, (b) $S = 0.1$, and (c) $S = 0.14$. Solid line: c_x, dashed line: c_y, dash-dotted line: c_z.

the flow direction becomes more peaked close to zero as shear increases. As the instabilities become 2D, the structures become uniform in the flow direction and there will be no gradient in this direction. That is why we have included just the results corresponding to 3D instabilities in part (a) of Figure 2.37. For the gradient in the y direction, it seems that the distributions are very close as long as the flow is still 3D; however, as it becomes 2D, the gradient becomes highly peaked close to zero. This tendency can be understood better knowing that as we increase shear a little further, 2D instability becomes 1D and the flow becomes perfectly uniform in the shear plane, meaning that we will not have any gradients in this plane. The concentration gradient in the z direction, also behaves almost the same as in other directions. As shear increases, the distribution becomes more peaked close to zero and beyond some shear rate, as all the instabilities become damped, it becomes exactly zero. The gradients in this direction become damped the last as shown earlier; that is why as shear rate is increased, it becomes peaked close to zero slower than the other two directions.

Figure 2.38 shows essentially the same data as Figure 2.37, but gradients corresponding to each shear rate are plotted separately. It clearly shows the distribution for each shear strength; as for the velocity components, when there is no shear, there is no preferred direction and all the gradient components are almost the same, However, as shear is imposed on the flow and damps the instabilities, the gradients become weaker, fastest in the flow direction and the slowest in the direction perpendicular to the shear plane. As explained above, for the 2D case (Figure 2.38 (c)), since there is no gradient in the flow direction, only the gradients in y and z are included.

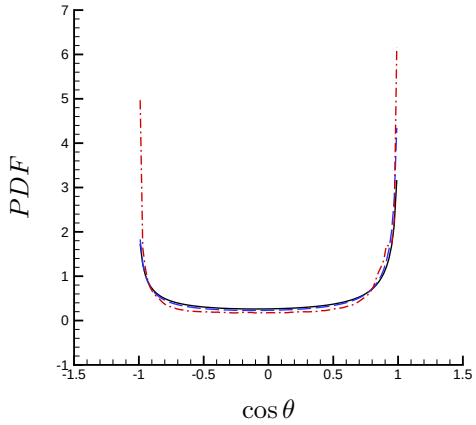

Figure 2.39: Probability distribution function of alignment of the concentration gradient field with gradient of divergence of the concentration weighted director field. Solid line: $S = 0$, dashed line: $S = 0.1$, dash-dotted line: $S = 0.14$.

2.5.10 Alignment of the concentration and the concentration weighted director fields

Following Saintillan and Shelley [39], we can integrate the conservation Equation (2.1) over $\mathbf{p}$, and then making use of the incompressibility condition, we arrive at a conservation equation for the concentration field $c(\mathbf{x}, t)$:

$$\frac{\partial c}{\partial t} + \mathbf{u} \cdot \nabla_{\mathbf{x}} c - D\nabla^2_{\mathbf{x}} c = -\nabla_{\mathbf{x}} \cdot (c\,\mathbf{n}). \tag{2.41}$$

This equation clearly identifies $\nabla_{\mathbf{x}} \cdot (c\,\mathbf{n})$ as a source term for magnitude changes in the concentration field, which is otherwise advected by the flow velocity and smoothed out by the diffusional terms. We should therefore, expect any observed density fluctuations to arise due to this term. The concentration weighted director field $c\,\mathbf{n}$ is not divergence free in general and since it determines the local direction of swimming of the particles, it will cause aggregation of particles wherever $\nabla_{\mathbf{x}} \cdot (c\,\mathbf{n}) < 0$ and a depletion in regions where $\nabla_{\mathbf{x}} \cdot (c\,\mathbf{n}) > 0$; therefore, resulting in the formation of density gradients [39]. The spatial gradients then become stabilized by the translational diffusion while the local alignment becomes stabilized by the rotational diffusion. Hence, the magnitude of density fluctuations at long times is determined by the balance of instabilities caused by the aggregation and depletions and the diffusive effects.

Figure 2.39 clearly shows the alignment of the concentration gradient with the gradient of divergence of the concentration weighted director field. It shows that the gradient of these two fields are totally aligned with each other, suggesting that the fields themselves are also aligned on average. As the flow becomes two-dimensional, this alignment seems to become stronger.

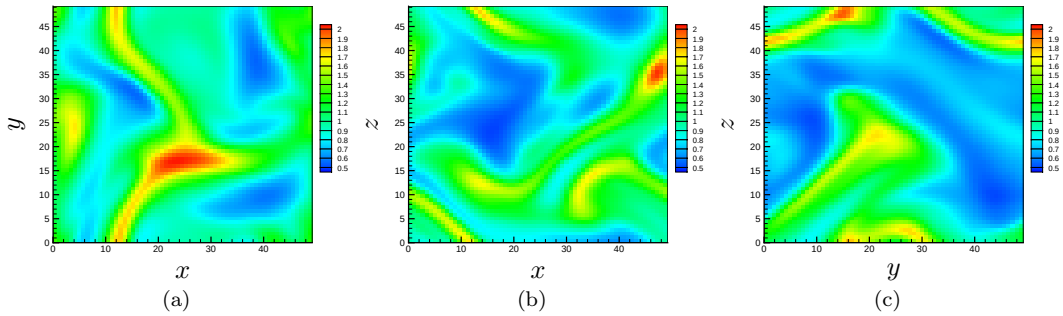

Figure 2.40: Slices of the concentration field in different planes for $S = 0$, (a) x-y, (b) x_z, and (c) y-z.

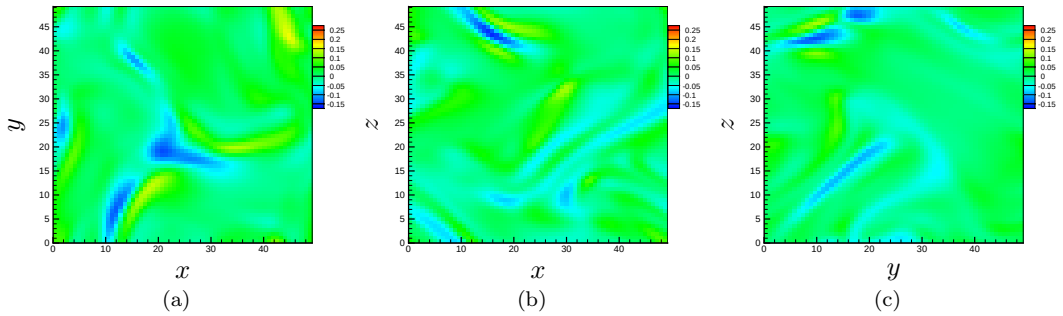

Figure 2.41: Slices of divergence of the concentration weighted director field in different planes for $S = 0$, (a) x-y, (b) x_z, and (c) y-z.

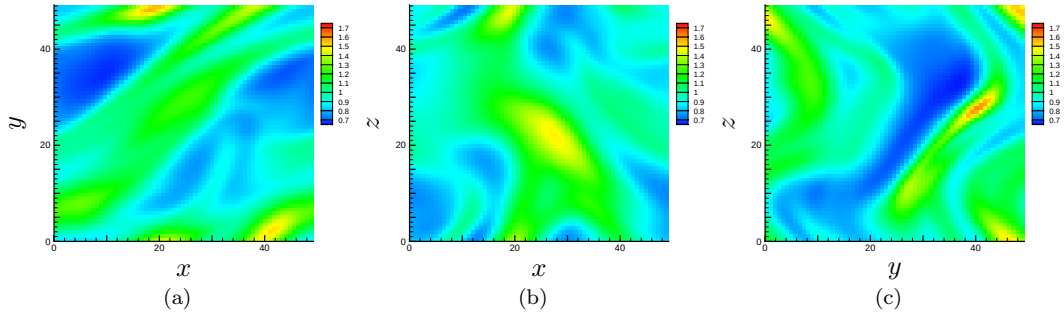

Figure 2.42: Slices of the concentration field in different planes for $S = 0.1$, (a) x-y, (b) x-z, and (c) y-z.

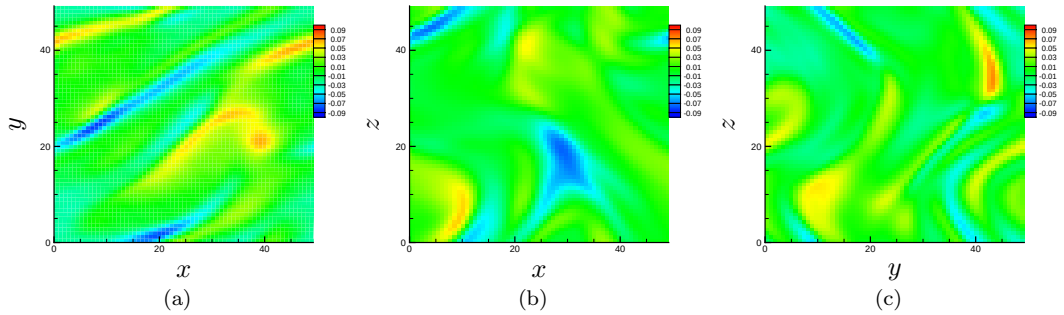

Figure 2.43: Slices of the divergence of the concentration weighted director field in different planes for $S = 0.1$, (a) x-y, (b) x-z, and (c) y-z.

To obtain a more qualitative picture of this alignment, we can compare the slices of the concentration field with the slices of the concentration weighted director field. Figures 2.40 and 2.41 show a slice of these two fields at the middle of the third dimension for x-y, x-z, and y-z planes respectively. It can be observed that both fields show a similar pattern and the orientation of structures are very close.

Almost the same behavior as for the case without shear flow can be observed when we impose shear on the system. Figures 2.42 and 2.43 show the same information as the last two figures for the $S = 0.1$. The structures, show the similar kind of alignment here as well.

As we increase shear further, the instabilities become 2D and the structures becomes uniform in the flow direction. For this case, we show just the two fields in the plane normal to the flow direction (Figure 2.44). They also show the same kind of behavior as for lower shear rates; the alignment seems to be even stronger as was found in Figure 2.39.

The correlation of the two fields can be further investigated over time by defining a correlation coefficient

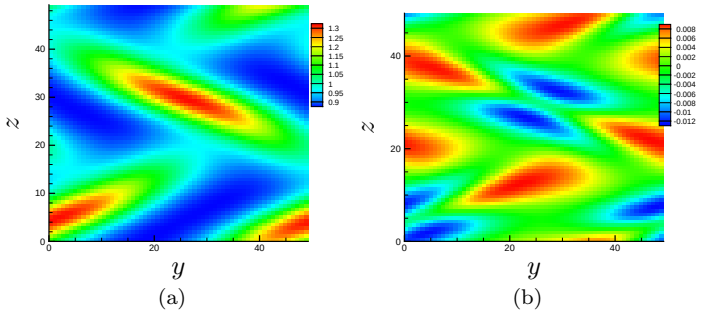

Figure 2.44: Slices of (a) concentration field and (b) divergence of the concentration weighted director field, in y-z plane for $S = 0.14$

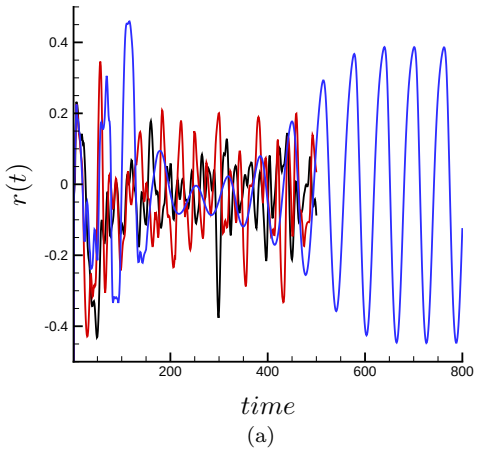

Figure 2.45: Correlation of the concentration weighted director field and the concentration field. Black line: $S = 0$, red line: $S = 0.1$, blue line: $S = 0.14$.

$r(t)$ as follows

$$r(t) = \frac{\int_\Omega (c-1) \times \nabla_{\mathbf{x}} \cdot \mathbf{n} \, \mathrm{d}\mathbf{x}}{\left(\int_\Omega (c-1)^2 \, \mathrm{d}\mathbf{x} \times \int_\Omega (\nabla_{\mathbf{x}} \cdot \mathbf{n})^2 \, \mathrm{d}\mathbf{x} \right)^{1/2}}. \tag{2.42}$$

Figure 2.45 shows the time evolution of the coefficient $r(t)$. At very short times, there does not seem to be any specific relation between the two fields. That is when the flow is developing after we perturb it, as discussed before, first the perturbations die off, but after a while the instabilities begin to occur. Between $t = 50 - 100$ a clear anti-correlation can be observed between the two fields. Beyond this time, the anti-correlation becomes a little weaker and the coefficient $r(t)$ oscillates between positive and negative values; however, it still seems to have a negative mean. The behavior of the case corresponding to 2D instabilities seem to be a little different at long times as the flow becomes statistically steady. In this case, the correlation coefficient clearly shows a quasi-periodic oscillation in time with constant amplitude. In this case, it seems

that flow becomes anti-correlated and correlated repeatedly.

2.6 Concluding Remarks

We have investigated pattern formation in dilute suspensions of swimming particles in the presence of an external shear flow. Using a kinetic model developed by Saintillan and Shelley [38, 39], we have done a linear stability study and also extensive three-dimensional numerical simulations to analyze the behavior of active suspensions when a shear flow is imposed on them. The dilute suspensions of active particles were found to be prone to instabilities and to reach a statistically steady state at long times. The suspension is characterized by large-scale collective motions of the size of the computational domain. These pattern formations were shown to have no preferred direction when in a quiescent flow; however, the shear flow tends to reorient them. It was found that the shear tends to align the particles with its mean direction and therefore stabilizes the flow. This damping mechanism by shear seems to be direction dependent; it is fastest in the direction of flow and slowest in the direction perpendicular to the shear plane. The shear flow first orients the structures in the most stretching axis of the mean strain field. As shear becomes stronger, the structures becomes uniform in the flow direction, making the instabilities two-dimensional. In this case, all the structures are totally aligned with the imposed flow. As the shear increases further, the structures become uniform in the shear plane, leaving a one-dimensional wave-like instability in the direction perpendicular to the shear plane. It seems that the flow dynamics here is dominated mainly by the director field being almost aligned with the most stretching eigenvector of the strain-rate tensor, therefore creating an inward gradient normal to it, in the direction of most compressive eigenvector.

Furthermore, some similarities between the flow under study here and turbulent flows were found. Although this flow is dominated by large-scale motions, it exhibits some of the characteristics that are considered universal in turbulent flows. It was found that there is a tendency towards the second and fourth quadrants in the Q–R plots, corresponding to the stable focus / stretching and unstable node / saddle / saddle topologies, respectively; this tear-drop shape in the Q–R plots is observed repeatedly in turbulent flows [48]. The shear flow, however, tends to damps the smaller-scale oscillations and therefore, concentrate the Q–R plots closer to the origin. Moreover, it was found that there is a slight tendency for the vorticity to be aligned with the strain-rate eigenvector corresponding to the intermediate strain eigenvalue. This behavior is also considered a universal characteristic of turbulent flows [50, 48].

Chapter 3

Rheology

3.1 Introduction

As particles swim, to leading order they cause a far-field force dipole, which in turn creates a disturbance flow in the fluid; this disturbance flow is known to result in hydrodynamic interactions, complex pattern formations and correlated motions in suspensions of many particles. These force dipoles exerted by the particles on the fluid are also expected to modify the effective rheology of their suspensions. The classical theories of Kirkwood and Batchelor for particulate suspensions [69, 52, 70, 71], motivates this anticipation due to the fact that the effective stress caused by a distribution of particles, can be expressed as a volume average of force dipoles on the particles.

Few experimental works have investigated the rheology of active suspensions; among them, Chen et al. [72] reported stress fluctuations by measuring the correlations of passive tracer particles in a bath of *E. coli*; their results indicated that the macroscopic fluctuations in stress depend substantially on the swimming behavior of bacteria on the microscopic level. Recently Sokolov and Aranson [73] investigated the rheology of a suspension of swimming *Bacillus subtilis*, through immersing a magnetic particle in a suspension film and measuring the viscous torque exerted on it. They observed a reduction of the effective viscosity by up to a factor of 7, and also found that this decrease is correlated with the activity of the particles, represented by their swimming velocity.

The effective rheology of the suspensions of self-propelled particles, have also been addressed in a few theoretical and computational studies. Hatwalne et al. [43] followed Simha and Ramaswamy [34], and included the effect of active stresses in their continuum model for the linear viscoelasticity of the liquid crystals. Using this model, they found that the viscosity increases in a suspension of puller particles as a results of activities, while it decreases in a suspension of pusher particles. Later, Ishikawa and Pedley [44] considered the rheological properties of a semi-dilute suspension of squirmers. They reported that the suspension rheology is strongly affected by the relative direction of shear flow and the gravity for bottom heavy squirmers. They also observed that the rheology is influenced by the sign of the stresslet, the bottom-

heaviness strength and the shear rate, and reported that the suspension shows strongly non-Newtonian properties. Recently, Haines et al. [45] demonstrated the importance of the particle orientation distribution on the rheology using a two-dimensional model. Based on an anisotropic distribution, they reported a viscosity reduction for pushers, even for isotropic particles. They also investigated the effect of bacterial shape to the leading on the rheological properties of the suspension. Later, they extended their model to three dimensions [74], and based on a Fokker-Planck equation, determined the orientation distribution using both numerical and asymptotic methods. Haines et al. [74] suggested that there is a decrease in the effective viscosity due to self propulsion when bacteria align along one of the principal axes of the hydrodynamic rate of strain tensor; it should be noted that such alignment can be achieved only by asymmetric bacteria. In fact, a dilute suspension of spheres shows Newtonian properties, while those of a suspension of ellipsoids often behave in a non-Newtonian way because of the fact that the ellipsoids tend to align with the principle axis of strain, except for few cases, such as an axisymmetric straining motion [5].

Saintillan [46], investigated the effective particle viscosity and normal stresses in a dilute active suspension using a simple kinetic model, in which the particle's orientation distribution satisfies the Fokker-Planck equation, and the particle's rotational velocity can be obtained from Jeffery's equation [55, 53]. His model can be regarded as an extension of classic studies of passive rod suspensions [75, 54]. He observed that the effective shear viscosity decreases in a suspension of pushers while it increases in pullers. Normal stresses were also found to be enhanced in puller suspensions, while they change sign for pushers. More recently, Saintillan extended this model to investigate other common flow types, and specifically to irrotational flows where it is possible to obtain analytical expressions for the effective viscosity and normal stresses [47]. In all types of flows considered in his study, results were in agreement with previous models and experiments. He also suggested the input power generated by swimming particles as the origin of the decrease in the predicted viscosity of the suspensions of pusher particles.

Of great interest in active suspensions is the effect of hydrodynamic interactions induced by the permanent force dipoles on the rheology of the suspension. However, none of the aforementioned works has addressed the role of hydrodynamic interactions on the rheology. In the Chapter 2, we investigated the effect of an external shear flow on the pattern formation and orientation distribution of a dilute suspension of swimming micro-organisms. The three-dimensional numerical simulations suggest that shear flow tends to orient the structures in the most stretching direction for intermediate shear strengths and in the flow direction for high enough shear rates. Shear flow is also found to damp the instabilities fastest in the mean flow direction, and slowest in the direction perpendicular to the shear plane; therefore, resulting in 3D, 2D, 1D instabilities and a stable regime as shear rate increases. These phenomena suggest that the rheological properties of an active

suspension can be quite complex and unsteady and hence, very hard to anticipate. In this work, we try to investigate the effect of hydrodynamic interactions and their resulting flow instabilities on the rheology of active suspensions.

In this work, we try to reveal the effect of hydrodynamic interactions on the rheology of a dilute suspension of self-propelled particles. In Sec. 3.2, we present the kinetic theory we are going to use to model the flow. Then, we move on to present the results in Sec. 3.3. The effect of shear on the orientation distribution of particle viscosity and also its alignment with other flow properties are investigated to gain a qualitative picture of the flow. We then analyze the time evolution of the rheological properties and the effect of shear on them and finally compare our results with those obtained from single-active-particle rheology [46].

3.2 Theory

In this work, we make use of the kinetic model developed by Saintillan and Shelley [38, 39], which was earlier introduced in Section 2.2. Now, in order to investigate the rheological properties of the suspension, we can move on to define the non-dimensional particle viscosity η_p, first normal stress difference ν_p and the second normal stress difference κ_p as

$$\eta_p = \boldsymbol{\Sigma}^p_{xy}/S, \tag{3.1}$$

$$\nu_p = (\boldsymbol{\Sigma}^p_{xx} - \boldsymbol{\Sigma}^p_{yy})/S^2, \tag{3.2}$$

$$\kappa_p = (\boldsymbol{\Sigma}^p_{yy} - \boldsymbol{\Sigma}^p_{zz})/S^2. \tag{3.3}$$

Therefore, using Equation (2.16), we can express the rheological properties as

$$\eta_p = C\left\langle p_x^2 p_y^2\right\rangle + \frac{\alpha + Br}{S}\left\langle p_x p_y\right\rangle, \tag{3.4}$$

$$\nu_p = C\frac{\left\langle p_x^3 p_y\right\rangle - \left\langle p_x p_y^3\right\rangle}{S} + \frac{\alpha + Br}{S^2}\left(\left\langle p_x^2\right\rangle - \left\langle p_y^2\right\rangle\right), \tag{3.5}$$

$$\kappa_p = C\frac{\left\langle p_y^3 p_x\right\rangle - \left\langle p_x p_y p_z^2\right\rangle}{S} + \frac{\alpha + Br}{S^2}\left(\left\langle p_y^2\right\rangle - \left\langle p_z^2\right\rangle\right), \tag{3.6}$$

in which $\langle\cdot\rangle$ denotes the configurational average

$$\langle\cdot\rangle = \int_\Omega \cdot\, \Psi(\mathbf{x}, \mathbf{p}, t)\, \mathrm{d}\mathbf{p}. \tag{3.7}$$

Furthermore, following Saintillan [47], we can perform an energy balance and identify the origin of

dissipation and active power in the flow, through considering the flow of an active suspension in a finite domain Ω bounded by fixed no slip boundaries, and governed by the unsteady Cauchy equation

$$\rho \frac{D\mathbf{u}}{Dt} = \nabla \cdot (-q\mathbf{I} + 2\mu \mathbf{E} + \mathbf{\Sigma}^p), \tag{3.8}$$

in which D/Dt denotes the material derivative. Now, taking the dot product of Equation (3.8) with $\mathbf{u}$ and integrating over the domain Ω through integration by parts and using symmetry of $\mathbf{E}$, yields [76]

$$\rho \frac{dE_k}{dt} = -2\mu \int_\Omega \mathbf{E} : \mathbf{E} \, \mathrm{dV} - \int_\Omega \mathbf{\Sigma}^{\mathrm{p}} : \mathbf{E} \, \mathrm{dV}, \tag{3.9}$$

in which E_k represents the kinetic energy of the flow and is defined as $E_k = 1/2\rho \int_\Omega |u|^2 \, \mathrm{dV}$. It should be noted that the energy balance presented here is valid only on length scales much larger than the size of the individual swimming particles. The first term on the right hand side of Equation (3.9) corresponds to the rate of viscous dissipation Φ in a viscous fluid and is always negative; i.e. $\Phi = 2\mu \int_\Omega \mathbf{E} : \mathbf{E} \, \mathrm{dV} \geq 0$. The second term corresponds to the contribution from the extra particle stresses (Equations 2.9, 2.10, and 2.11). Therefore, we can decompose it as

$$\int_\Omega \mathbf{\Sigma}^p : \mathbf{E} \, \mathrm{dV} = \int_\Omega \mathbf{\Sigma}^{\mathrm{f}} : \mathbf{E} \, \mathrm{dV} + \int_\Omega \mathbf{\Sigma}^{\mathrm{b}} : \mathbf{E} \, \mathrm{dV} + \int_\Omega \mathbf{\Sigma}^{\mathrm{s}} : \mathbf{E} \, \mathrm{dV}. \tag{3.10}$$

The first two terms on the right hand side of 3.10 are dissipative terms corresponding to the inextensibility of particles in the presence of shear flow (Φ_f) and to the Brownian motions (Φ_b), respectively. The third term (Φ_s), however can be regarded as an active input power induced by the permanent dipoles exerted by the swimming particles [47]. This term can be attributed to the rate of mechanical energy generated by the particles, as they swim through the fluid, and therefore is not a dissipative term. In fact, it is negative for pusher particles, causing the intrinsic particle viscosity to become negative. We will further discuss this phenomenon in the Section 3.3.

3.3 Results

Figure 3.1, shows the isosurfaces of particle viscosity η_p for different shear rates. As shear rate increases, the isosurfaces seem to become aligned with the most stretching direction of the imposed flow; beyond a certain shear strength, the instabilities in the flow become 2D and the structures becomes uniform in the flow direction (x). Increasing the shear further will damp the instabilities in the y direction as well and there

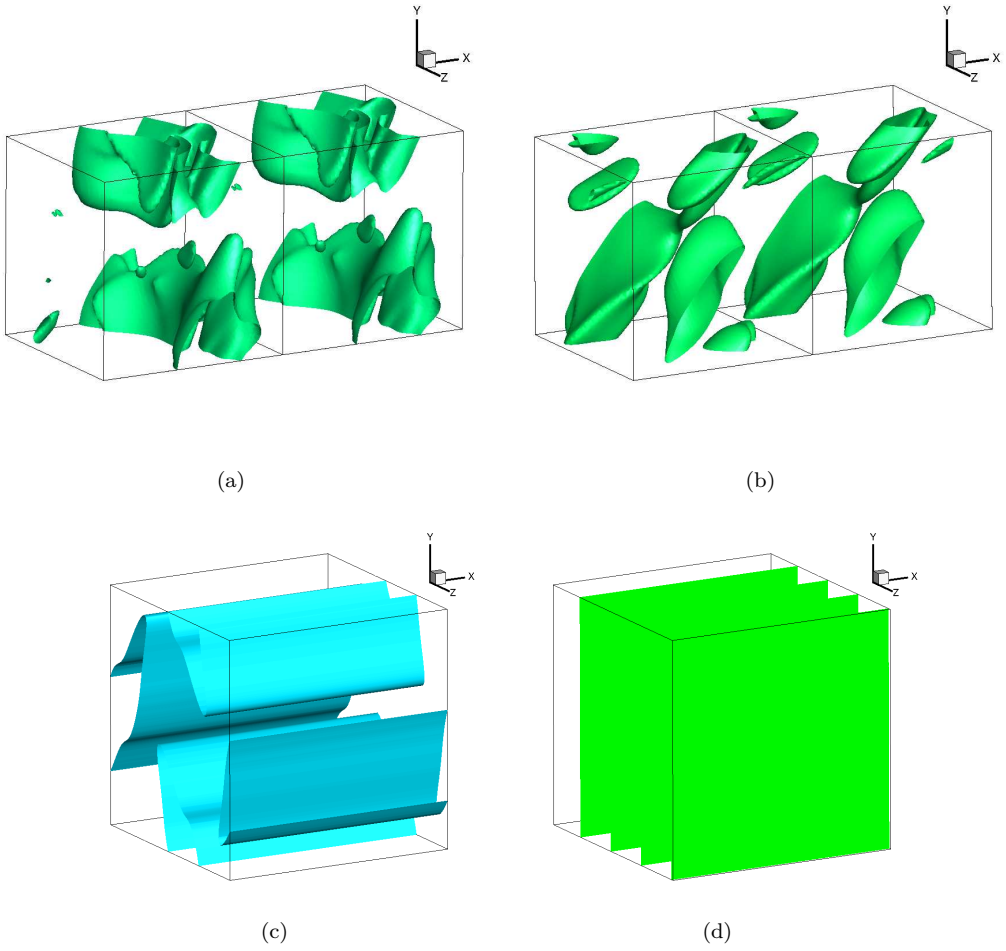

Figure 3.1: The particle viscosity η_p isosurfaces for different shear rates: a) $S = 0$, $\eta_p = -3.5$ b) $S = 0.1$, $\eta_p = -2.5$ c) $S = 0.14$, $\eta_p = -1$ d) $S = 0.2$, $\eta_p = -0.65$

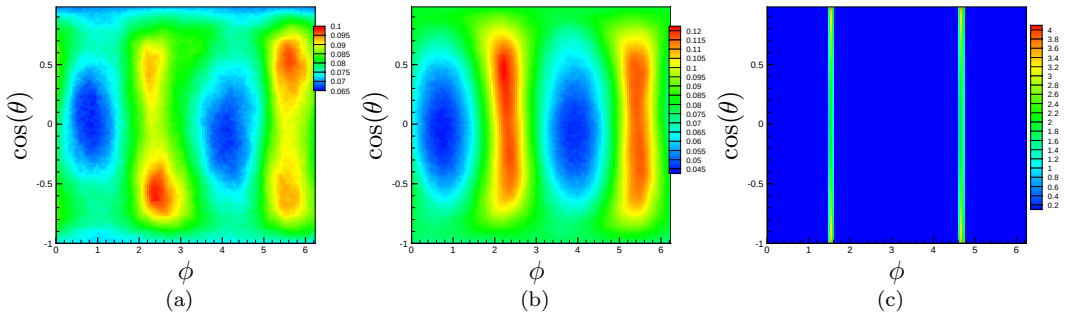

Figure 3.2: Joint probability distribution function of particle viscosity gradient ($\nabla\eta_p$) angles for different shear rates: (a) $S = 0$, (b) $S = 0.1$, and (c) $S = 0.14$

seems to be a 1D instability in the direction normal to the shear plane (i.e. z direction). Beyond a certain shear strength, no instabilities will be present in the flow and the structures become spatially uniform. In this case, it is expected that the rheological properties of the flow become the same as that of a single swimming particle in the presence of shear flow.

Now, in order to look closer at the effect of shear flow on the orientation of structures in the flow, we make use of joint probability distribution functions (JPDF) of angles of scalar field gradients.

Figure 3.2 shows the JPDF of angles of particle viscosity gradient ($\nabla\eta_p$). When there is no shear present in the flow, there is no preferred direction; it should be noted that the contour levels of peaks and valleys in Figure 3.2 (a) are very close to each other and their corresponding angle might be an artifact of the computational domain being square. Part (b) of the figure shows that as shear increases, it initially tends to orient the gradient vector to $\phi = 3\pi/4, \pi + 3\pi/4$ while it is symmetric about $\theta = \pi/2$ (i.e. shear plane). This observation suggests that in the shear plane, the structures as shown in Figure 3.1, are oriented in the $\phi = \pi/4$ direction, which is the most stretching direction of the flow while they oscillate almost symmetrically about $\theta = \pi/2$. However, as shear strength increases further and flow becomes 2D and uniform in the shear flow direction, the gradient vector becomes aligned with the poles (i.e. $\theta = 0, \pi$), suggesting that the structures are completely aligned in the flow direction.

In order to gain a qualitative picture of the flow field, we present a slice of different fields in the shear plane (i.e. x-y) for $S = 0.1$ and in the y-z plane for $S = 0.14$ (since the flow is uniform in the flow direction for this shear rate corresponding to 2D instabilities).

Figure 3.3 shows mid z slice of different fields in x-y plane for $S = 0.1$. The structures corresponding to the higher magnitudes of negative particle viscosity seem to be aligned with the most stretching direction in the shear plane. Comparing the particle viscosity with the concentration field, it seems that large-scale

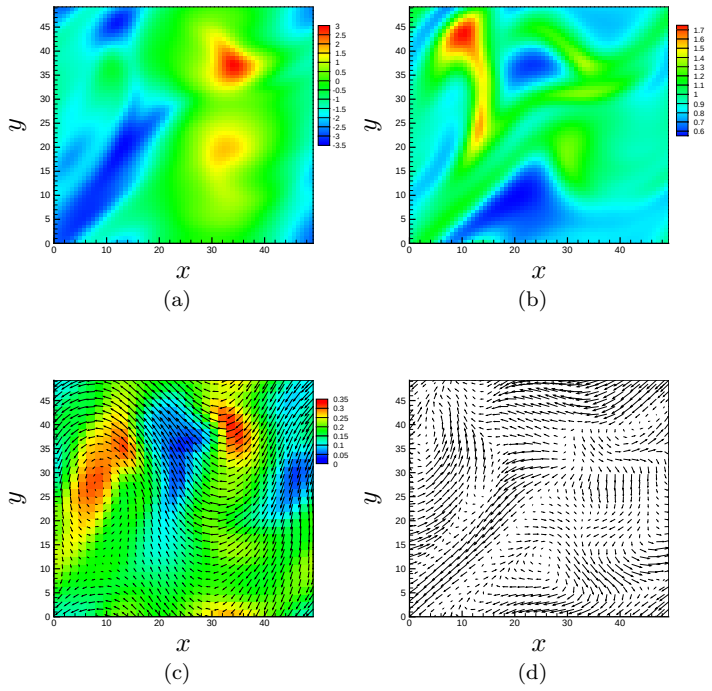

Figure 3.3: x-y plane slices at mid z and $t = 440$ for $S = 0.1$ corresponding to (a) particle viscosity, (b) concentration, (c) velocity vectors over contours of vorticity magnitude, and (d) director field vectors.

structures have the same orientation in both, but no relations between more concentrated regions and particle viscosity can be perceived from this figure. Looking more closely at the velocity vectors and the director field, suggests that the most negative values of particle viscosity are associated with a jet of aligned swimming particles in the most stretching direction that also corresponds to low vorticity magnitudes. It in fact suggests that the negative particle viscosity is associated with an extensional type of flow.

Figure 3.4 shows the same information as that of Figure 3.3 in the mid x slices of y_z plane for $S = 0.14$. For this shear rate, as indicated earlier the flow is 2D and uniform in the x direction. In this figure, it is more clear that negative particle viscosities are associated with high concentration regions. This observation suggests that as particles form clusters and inject power into the fluid around them, they create a negative particle viscosity, which reduces flow drag on them and therefore, makes it easier for them to swim. Comparing the particle viscosity with the velocity and director fields, it appears that higher magnitudes of particle viscosity are associated with vortical structures. However, it is not easy to obtain a precise picture of flow and the relative effect of different flow properties on the particle viscosity by looking just at typical slices of flow and we will need other tools.

Analyzing the alignment of the particle viscosity with the concentration gradient, the director field

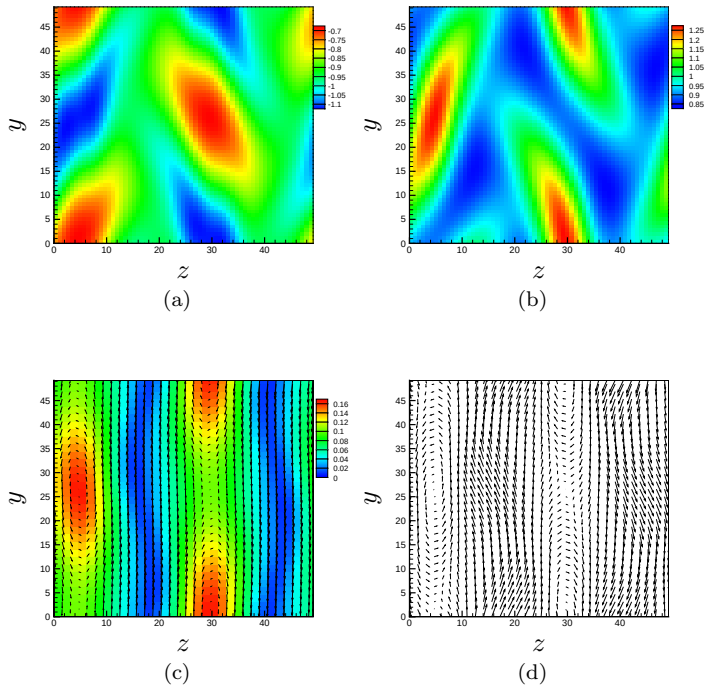

Figure 3.4: y-z plane slices at mid x and $t = 750$ for $S = 0.14$ corresponding to (a) particle viscosity, (b) concentration, (c) velocity vectors over contours of vorticity magnitude, and (d) director field vectors.

$\mathbf{n} = \frac{1}{c(\mathbf{x},t)} \int_\Omega \Psi(\mathbf{x}, \mathbf{p}, t)\mathbf{p}\, \mathrm{d}\mathbf{p}$, and the vorticity field, we might be able to understand their relative effects and also the effect of shear flow on the orientation distribution of structures.

Figure 3.5 shows the alignment of particle viscosity gradient ($\nabla\eta_p$) with different fields mentioned above. As it appears, ($\nabla\eta_p$) is aligned with the concentration gradient and this alignment seems to increase with shear rate. The reason why the figure suggests a $\theta = \pi$ degree between the two fields is that the particle viscosity is mostly a negative quantity; therefore, the figure suggests that higher concentration regions are associated with lower particle viscosities (i.e. greater in magnitude). This observation makes sense since more concentrated regions can be interpreted as regions where more active power is generated by the particles and according to the energy balance presented in Section 3.2, this power injection results in lower particle viscosities. Parts (b) and (c) of Figure 3.5 suggest that ($\nabla\eta_p$) slightly tends to be normal to both the director, and vorticity fields, while this effect becomes more pronounced in the 2D instability case. In the 2D case, it is relatively easy to imagine this alignment; it means that iso structures of particle viscosity are aligned with the director field and vorticity axis. Considering a vortex tube whose axis is aligned in the flow direction, particles swim around the vortex axis and the gradients become normal to it, resulting in the alignments observed. It is worth mentioning here that the alignment of other rheological properties such

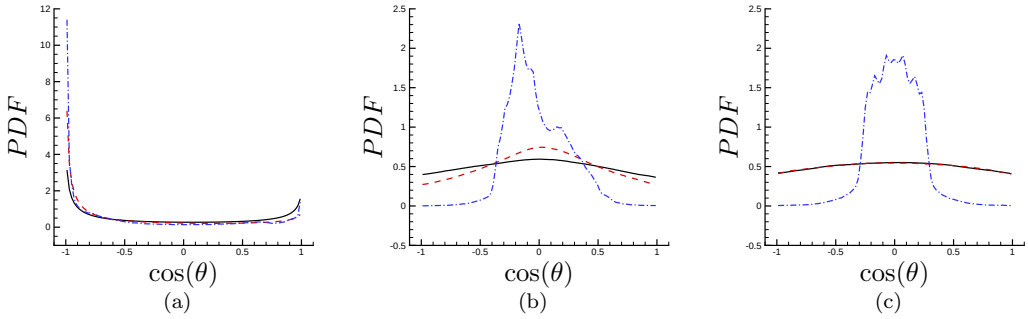

Figure 3.5: Alignment of particle viscosity gradient ($\nabla\eta_p$) with (a) concentration gradient (∇c), (b) director field, and (c) vorticity field. Solid line: $S = 0.05$, dashed line: $S = 0.1$, and dash-dotted line: $S = 0.14$

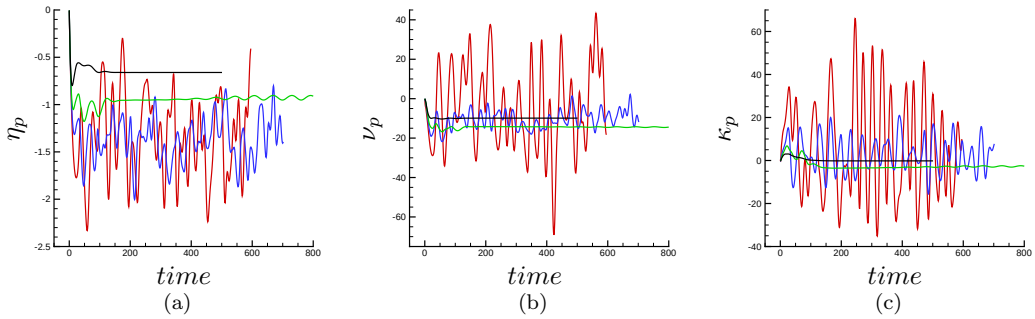

Figure 3.6: Time evolution of (a) particle viscosity η_p, (b) first normal stress difference ν_p, and (c) second normal stress difference κ_p. Red line: $S = 0.05$, blue line: $S = 0.1$, green line: $S = 0.14$, and black line: $S = 0.2$.

as normal stress differences (i.e. ν_p and κ_p) and also diffusions and active input power (i.e. Φ_f, Φ_b and Φ_s) were also investigated and they show essentially the same behavior as particle viscosity.

Now, having a more clear picture of the flow and the relative effect of different fields on the particle viscosity, it is interesting to analyze time evolution of different rheological properties. The effect of hydrodynamic interaction and instabilities can be observed qualitatively from the evolution in time of spatially-averaged rheological properties. Figure 3.6 shows the time evolution for the particle viscosity and normal stress differences. As it appears, all the properties oscillate considerably in time for lower shear rates, but as shear increases, it damps the oscillations more and more until the instabilities become 2D (corresponding to the green line in the figures), for which small amplitude quasi-steady oscillations can be observed at the long times. Increasing shear further, all the properties corresponding to 1D and no instability cases, cease to oscillate and they become steady in time as flow develops. The particle viscosity appears to be negative on average for smaller shear rates and approaches zero as shear increases. This observation suggests that at lower shear rates particles create a negative particle viscosity; therefore, reducing the total viscosity, making

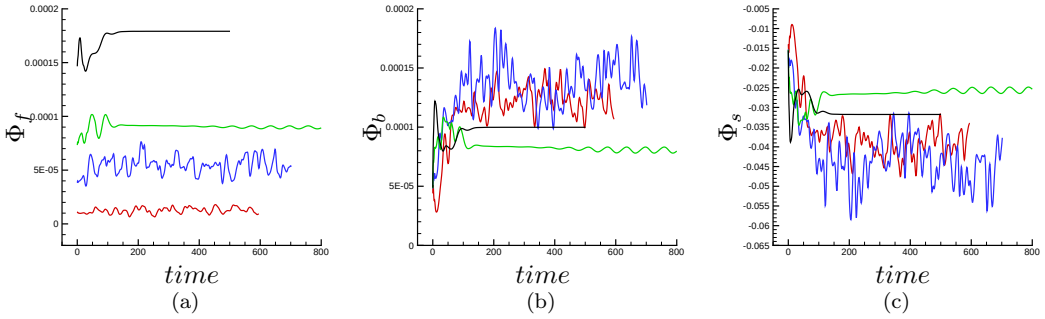

Figure 3.7: Time evolution of (a) dissipation due to the external flow Φ_f, (b) dissipation due to the Brownian motions Φ_b, and (c) active input power Φ_s. Red line: $S = 0.05$, blue line: $S = 0.1$, green line: $S = 0.14$, and black line: $S = 0.2$.

it easier to swim and resulting in the correlated motions or vice versa. As shear increases and dampens the instabilities, the negative particle viscosity also decreases in magnitude, making it harder for the particles to swim that eventually damps all the correlated motions and makes the particles completely aligned with the shear flow. The first normal stress difference seems to be negative most of the time for all shear rates. As shear rate increases, it decreases more in magnitude, becoming closer to zero value. The second normal stress difference is however positive most of the time, decreasing in magnitude as well as shear increases. The case corresponding to the 2D instability (the green line in the figures) seems to behave a little differently from the trend explained; it seems to be greater in magnitude for the first normal stress difference and to be negative most of the time for the second normal stress difference.

The time evolution of energy dissipations and active input power of particles (Figure 3.7) also is interesting to analyze in order to understand how different energy mechanisms vary in time and also how shear strength affects them. Dissipation due to the external shear flow Φ_f increases in magnitude as shear rate increases as expected due to the fact that it represents the dissipation caused by the external flow caused by inextensibility of the particles; therefore, this dissipation should increase with the strength of the external flow. The oscillation amplitude also decreases on average as shear strength increases. The effect of shear on the evolution of dissipation due to the Brownian motions (Φ_b) seems to be a little bit harder to anticipate. In fact, Φ_b represents the competition of two opposing effects. As shear increases, we know that oscillations become damped and the particles become more aligned with the external flow, consequently, reducing the diffusion due to the Brownian motions that are principally fluctuations. However, since the dissipation is also proportional to the shear strength, it is hard to guess how it behaves as shear increases. Figure 3.7 shows that it increases a little bit initially when the flow is still 3D, but it decreases almost considerably as the flow becomes 2D. As shear increases and instabilities become damped further, Φ_b seems to increase

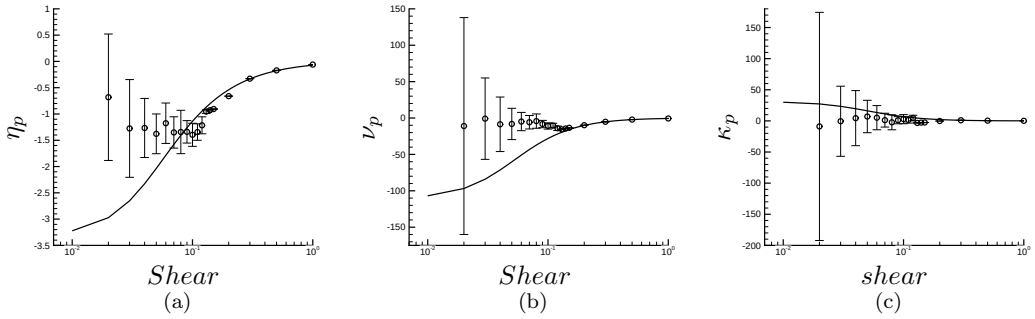

Figure 3.8: Shear effect on the (a) particle viscosity η_p, (b) first normal stress difference ν_p, and (c) second normal stress difference κ_p. The bars shown represent standard variation due to averaging.

again. The behavior of the active input power is also similar to that of Brownian motion and hard to anticipate a priori. It increases in magnitude with shear rate while the instabilities are 3D, but decreases substantially in magnitude as the flow becomes 2D. As shear strength increases further Φ_s increases in magnitude again. As explained earlier, particles seem to generate less and less power as shear aligns them and damps the instabilities, but since Φ_s is proportional to the shear rate as well, it increases in magnitude beyond a certain shear limit.

Now, having observed the effect of hydrodynamic instabilities on the evolution of different rheological properties, we are eager to inspect more about the dependence of these properties on the strength of imposed shear flow. Then, we will be able to compare our results with those published for a single self-propelled particle without any hydrodynamic interactions [46]. Such a comparison clearly shows the effect of hydrodynamics on the rheology of the flow.

Figure 3.8 presents the variation of particle viscosity, and normal stress differences with shear rate. The solid line corresponds to the rheology of a single pusher particle in shear flow and therefore, no hydrodynamic interactions is included in it. However, the simulation results presented so far include the hydrodynamic interactions and consequently, are able to capture the role of instabilities on the rheological properties. The particle viscosity η_p predicted by single-particle rheology appears to be negative for low shear rates; this behavior could be anticipated from Equation (3.4), were the permanent dipole due to swimming appear to decrease the Brownian and external flow contributions to the particle viscosity. As shear increases, the particles become aligned with the flow and their corresponding viscosity approaches zero. However, the particle viscosity obtained from our simulations does not follow the same trend for lower shear rates. In fact, it seems to not vary much as long as the flow is still 3D; but as the flow becomes 2D, it approaches the single-particle rheology. Increasing shear further damps all instabilities, making the flow the same as that

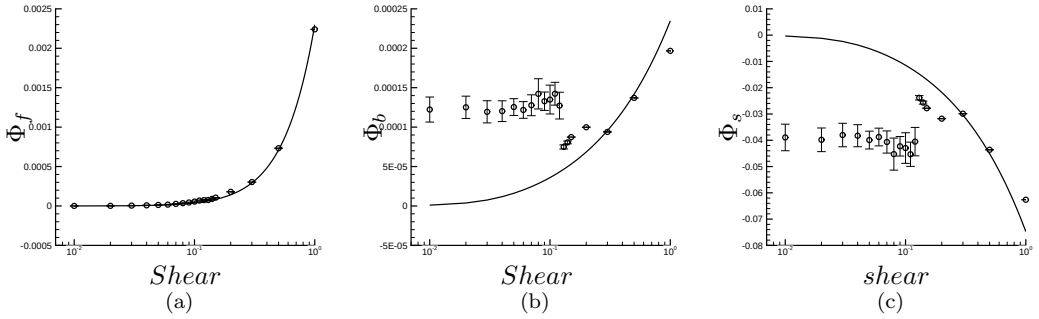

Figure 3.9: Shear effect on the (a) dissipation due to external flow Φ_f, (b) dissipation due to Brownian motions Φ_b, and (c) active input power Φ_s

of a single active particle in the shear flow; that is why as instabilities disappear, our results agree very well with the single-particle rheology.

The normal stresses as shown before oscillate considerably in time; they seem to be closer to zero on average than the predictions from the single-particle rheology. Overall, they follow the same behavior as the particle viscosity; almost constant with shear for low strengths and matching the single-particle rheology for high shear rates. On average, the first normal stress difference (ν_p) is negative and the second normal stress difference (κ_p) is positive for lower shear rates; both of them approach zero as shear increases. It should be noted that due to high oscillation amplitude of the data for lower shear rates, their standard variation is considerable; however, as shear damps the oscillations, the standard variation of the data also decreases for higher shear rates.

Finally, Figure 3.9 shows the effect of shear on the energy dissipation and active input power. The simulation results and the predicted values of dissipation due to the inextensibility of particles in the presence of the external shear flow (i.e. Φ_f) for a single self-propelled particle, appear to match very well for all values of shear considered here. Φ_f as expected increases with shear and is positive since it corresponds to a diffusive mechanism. The results from simulations and single self-propelled particle theory however do not match for Brownian dissipation and active input power as those of Φ_f. The Brownian dissipation Φ_b seems to be almost constant with shear for low shear strengths, but as the flow becomes 2D, it decreases considerably that is expected since in the 2D case the structures are perfectly aligned with the shear in the flow direction. That is also the reason why the simulation results approach the theory. For higher values of shear, the simulation results match better with the theory, increasing with shear rate; however, they do not match perfectly for highest shear value examined. The particle active input power (Φ_s) is negative while the dissipation mechanisms are always positive. Φ_s is actually the cause of creating negative particle viscosities.

The trend of Φ_s is pretty much the same as the Brownian dissipation; though, their sign is different. That is to say Φ_s almost does not change for lower shear rates, decreases in magnitude as flow becomes 2D, but increases in magnitude again as shear strength increases further. In all the cases, as expected, it seems that the simulations and single-active-particle theory match very well for higher values of shear as soon as oscillations become damped and flow becomes 2D and further 1D and finally spatially uniform.

3.4 Concluding Remarks

In this work, we have made use of the kinetic theory developed by Saintillan and Shelley [38, 39] to investigate the rheology of active suspensions. We extended recent numerical works on rheology of dilute suspensions of swimming particles to include the effect of hydrodynamic interactions. The role of shear strength on the instabilities and its effect on the particle viscosity and orientation of its iso-structures were investigated. It is shown that, as shear increases, the isosurfaces of particle viscosity and other rheological properties become aligned with the most stretching direction of the imposed flow; as shear increases further and instabilities become 2D, the structures become uniform in the flow direction. Increasing shear further damps all the instabilities in the shear plane, leaving a 1D instability normal to the shear plane; beyond this point, all instabilities become damped and the rheological properties of the flow will be the same as those of a single self-propelled particle in the shear flow.

We further showed that the particle viscosity and other rheological properties are aligned with the concentration field. This observation suggests that more concentrated regions of the flow are associated with lower total viscosity that makes it easier for micro-organisms in large groups to swim, and therefore result in collective dynamics in such suspensions. The rheological structures were also found to be slightly aligned with the director field and the vorticity vectors when the flow is 3D, but completely aligned with these two fields as the flow becomes 2D. It is easy to imagine this alignment in the 2D case where it can be thought of as a vortex tube with the vortex axis in the flow direction, leading particles to swim about the vortex axis; therefore, the viscosity gradient will be normal to both the director field and the vortex axis.

Moreover, we investigated the time evolution of the rheological properties of the suspension, showing the effect of instabilities and hydrodynamic interactions on the rheology as flow develops in time. All properties oscillate considerably in time, but the amplitude of these oscillations decreases with shear. The particle viscosity seems to decrease in magnitude as shear increases. The first normal stress difference is negative while the second one is positive; this behavior is in contrast to the passive suspensions, for which both of them decrease in magnitude with shear rate. The energy dissipation due to the inextensibility of particles

in the external shear flow increases with shear, but the other two energy mechanisms seem to behave in a more complicated fashion with shear. The Brownian diffusion first decreases with shear as the particles become aligned with the flow, but with increasing shear, it increases again. The active input power, which represents the mechanical energy injected by the swimming particles into the fluid, is negative and decreases in magnitude as shear increases, but similar to the Brownian diffusion, it increases in magnitude again as shear increases further.

Finally, we compared the rheological properties of the suspension obtained from the simulations with those of a single active particle in the shear. It seems that the properties do not vary much with shear as long as the flow is 3D, but as the instabilities are damped and the flow becomes 2D, our results approach those predicted by the non-interacting theory. As shear increases further and all instabilities in the flow become damped, the flow becomes spatially uniform that is essentially the same as that of a single self-propelled particle in the presence of an external flow; for this reason our results match very well those of the theory in the limit of high shear rates.

Chapter 4

Conclusions

In this work, we have studied the collective dynamics and rheological properties of a dilute suspensions of swimming pusher particles, in the presence of an external shear flow. Based on a kinetic model recently proposed by Saintillan and Shelley [38, 39], we have performed linear stability analysis and 3D numerical simulations to gain an understanding of the effect of the imposed shear flow on the suspensions properties and pattern formation. Instabilities and collective motions on the length scales much larger than the size of an individual organism were observed; these dynamics were found to reach a statistically steady state at long times. The linear stability analysis suggested that the effect of shear is to dampen the instabilities; the numerical simulations verified these predictions and also found the rate of this stabilizing effect to be direction dependent. When there is no shear flow present, the flow structures have no preferred direction; however, imposing the external flow reorients the structires. We found that the flow structures tend to become aligned with the extensional axis of the mean shear for the low-to-intermediate shear rates, while increasing shear a little bit further will make them totally aligned with the imposed flow, making the structures uniform in the flow direction. Beyond this shear rate, the instabilities in the shear plane will disappear altogether, resulting in a 1D wave-like gradient in the direction perpendicular to the shear plane. This 1D instability also disappears for strong enough imposed flow, making the structures spatially uniform. We also tried to analyze the relative interplay of different flow properties; our results suggest that the dynamics of the suspension is dominated by the alignment of director field with the most stretching strain that leads to a density gradient in the direction of most compressive strain, which is normal to the stretching direction.

Although the flow under study in this work is at low-Reynolds-number regime and is dominated by the large-scale motions, we found that it shares some similarities with turbulent flows. In particular, in the Q–R plots, we observed a slight tendency towards the second and fourth quadrants when there is no shear flow present. A tear-drop-like geometry oriented towards these two quadrants, is reported in many of the studies on turbulent flows [48]. However, as mentioned, it should be noted that the turbulent flows are dominated by fine-scale fluctuations while the small-scale oscillations in an active suspension at the Stokes-flow regime, are very weak. In fact the shear flow turns out to dampen these smaller-sclae oscillations, making the Q–R

plots more focused near the origin. We also observed that there is a slight tendency for the vorticity to be aligned with the intermediate-strain direction. This alignment is also reported repeatedly in turbulent flow literature and is considered a universal characteristic of such flows [50, 48].

In the second part of this work, we investigated numerically the rheological properties of an active suspension in the presence of an external linear shear flow. As the flow goes through the different instability regimes described above, we found that the rheological properties' iso-structures become aligned with the shear flow, as for the other flow structures. In fact, we found that the particle viscosity is aligned with the concentration field and also slightly with the director and vorticity fields. This suggests that as pusher particles form clusters, they reduce the viscosity of the suspending fluid that makes it easier for them to swim; this might be the reason why particles tend to swim in large groups and strong density fluctuations are observed in such suspensions. The time evolution of spatially averaged particle viscosity, first and second normal stress differences, as well as active input power and diffusive mechanisms were also also investigated. All these properties oscillate in time and were found to reach a statistically steady state at long times. In particular, the particle viscosity was found to be negative; also, in contrast to the passive suspensions, the first and second normal stress differences were found to be negative and positive, respectively. All these properties decay in magnitude as the strength of the shear flow is increased. Furthermore, we compared the rheological properties, active input power, and diffusive mechanisms with those predicted by the single-active-particle rheology, and found that these predictions are mostly different for lower shear rates, but they approach each other as the imposed shear weakens the instabilities and finally the flow becomes spatially uniform.

Appendix A

Spherical Harmonics Identities

As mentioned in Section 2.3, we can expand the distribution function on the basis of surface harmonics, $\tilde{\psi}(\mathbf{p}) = \sum_{l=0}^{M} \sum_{m=-l}^{l} a_{l,m} \mathbf{Y}_l^m(\theta, \phi)$. Substituting this expansion into Equation (2.28), we can simplify further the equation so obtained using the following properties of the spherical harmonics:

$$\int_{\Omega} \mathbf{Y}_l^m \, \mathrm{d}\mathbf{p} = 2\sqrt{\pi}\delta_{l,0}\delta_{m,0}, \tag{A.1}$$

$$\nabla^2 \mathbf{Y}_l^m = -l(l+1)\mathbf{Y}_l^m. \tag{A.2}$$

Then we can make use of the orthonormality property of spherical harmonics to simplify the obtained equation further, through multiplying it by the complex conjugate $\mathbf{Y}_l^{m*}$ and using the identity

$$\int_{\Omega} \mathbf{Y}_l^m \mathbf{Y}_{l'}^{m'*} \, \mathrm{d}\mathbf{p} = \delta_{\mathrm{l,l'}}\delta_{\mathrm{m,m'}}. \tag{A.3}$$

At this level, to enhance the simplification further, we can use some of the analytical recursive identities of the spherical harmonics that help reduce the obtained equation to a system of algebraic eigenvalue problems for the coefficients $a_{l,m}$. Tabel A.1 lists the identities used in reducing the multipolar integrands to simple products of harmonics.

Product	Result	Coefficients	
$\cos\theta \, \mathbf{Y}_l^m$	$A_{l,m}^1 \mathbf{Y}_{l+1}^m + A_{l,m}^2 \mathbf{Y}_{l-1}^m$	$A_{l,m}^1 = \sqrt{\frac{(l-m+1)(l+m+1)}{(2l+1)(2l+3)}}$	$A_{l,m}^2 = \sqrt{\frac{(l-m)(l+m)}{(2l-1)(2l+1)}}$
$\exp^{\imath\phi} \sin\theta \, \mathbf{Y}_l^m$	$B_{l,m}^2 \mathbf{Y}_{l-1}^{m+1} - B_{l,m}^1 \mathbf{Y}_{l+1}^{m+1}$	$B_{l,m}^1 = \sqrt{\frac{(l+m+1)(l+m+2)}{(2l+1)(2l+3)}}$	$B_{l,m}^2 = \sqrt{\frac{(l-m)(l-m-1)}{(2l-1)(2l+1)}}$
$\exp^{-\imath\phi} \sin\theta \, \mathbf{Y}_l^m$	$C_{l,m}^1 \mathbf{Y}_{l+1}^{m-1} - C_{l,m}^2 \mathbf{Y}_{l-1}^{m-1}$	$C_{l,m}^1 = \sqrt{\frac{(l-m+1)(l-m+2)}{(2l+1)(2l+3)}}$	$C_{l,m}^2 = \sqrt{\frac{(l+m)(l+m-1)}{(2l-1)(2l+1)}}$

Table A.1: Spherical harmonic identities used in reducing the multipolar integrands to simple products of harmonics

Further, to evaluate the terms involving gradient $\nabla_p \mathbf{Y}_l^m$, we use the relation

$$\frac{\partial \mathbf{Y}_l^m}{\partial \theta} = \frac{1}{\sin\theta}\left(l\cos\theta \mathbf{Y}_l^m - \alpha_{l,m}\mathbf{Y}_{l-1}^m\right), \tag{A.4}$$

where $\alpha_{l,m}$ is defined as

$$\alpha_{l,m} \equiv \sqrt{\frac{(2l+1)(l^2-m^2)}{2l-1}}. \tag{A.5}$$

Finally, going through the steps mentioned above and using the identities, we can reduce Equation (2.28) to an algebraic combination of coefficients introduced in Table A.1 and the $\alpha_{l,m}$ coefficients. This is a system of algebraic eigenvalue problems for coefficients $a_{l'm'}$. We may therefore, write these equations in the form of an eigenvalue equation $\mathbf{M}\cdot\mathbf{a} = \lambda\mathbf{a}$, in which $\mathbf{a}$ is the vector of spherical harmonics expansion coefficients and λ is the corresponding eigenvalue set. If we truncate this system for a finite number N of harmonic modes, then the obtained eigenvalues resulting from numerically solving this system will be a discrete approximation to the first $(N+1)^2$ eigenvalues of Equation (2.28). We make use of Netlib's LAPACK package to solve this eigenvalue problem numerically.

References

[1] E. Lauga and T. R. Powers. The hydrodynamics of swimming micro-organisms. *Reports on Progress in Physics*, 72(9):096601, 2009.

[2] J. Soria, R. Sondergaard, B. J. Cantwell, M. S. Chong, and A. E. Perry. A study of the fine-scale motions of incompressible time-developing mixing layers. *Physics of Fluids*, 6(2):871–884, 1994.

[3] M. Andreae R. Charlson, J. Lovelock and S. Warren. Oceanic phytoplankton, atmospheric sulphur, cloud albedo and climate. *Nature*, 326(6114):655, 1987.

[4] T. J. Pedley and J. O. Kessler. Hydrodynamic phenomena in suspensions of swimming micro-organisms. *Annual Review of Fluid Mechanics*, 24(1):313–358, 1992.

[5] T. Ishikawa. Suspension biomechanics of swimming microbes. *Journal of The Royal Society Interface*, 6(39):815–834, 2009.

[6] J. Lighthill. *Mathematical Bio-Fluid Dynamics*. SIAM, Philadelphia, 1975.

[7] J. Lighthill. Flagellar hydrodynamics. *SIAM Review*, 18(2):161–230, 1976.

[8] S. Childress. *Mechanics of Swimming and Flying*. Cambridge University Press, 1981.

[9] E. M. Purcell. Life at low Reynolds number. *American Journal of Physics*, 45(1):3–11, 1977.

[10] A. Shapere and F. Wilczek. Self-propulsion at low Reynolds number. *Physical Review Letters*, 58(20):2051–2054, May 1987.

[11] A. Shapere and F. Wilczek. Geometry of self-propulsion at low Reynolds number. *Journal of Fluid Mechanics*, 198:557–585, 1989.

[12] H. Berg and R. Anderson. Bacteria swim by rotating their flagellar filaments. *Nature*, 245(5425):380–382, 1973.

[13] I. S. Aranson, A. Sokolov, J. O. Kessler, and R. E. Goldstein. Model for dynamical coherence in thin films of self-propelled micro-organisms. *Physical Review E*, 75(4):040901, Apr 2007.

[14] M. Ramia, D. L. Tullock, and N. Phan-Thien. The role of hydrodynamic interaction in the locomotion of micro-organisms. *Biophysical Journal*, 65(2):755–778, 1993.

[15] S. Nasseri and N. Phan-Thien. Hydrodynamic interaction between two nearby swimming micromachines. *Computational Mechanics*, 20(6):551–559, 11 1997.

[16] C. M. Pooley, G. P. Alexander, and J. M. Yeomans. Hydrodynamic interaction between two swimmers at low Reynolds number. *Physical Review Letters*, 99(22):228103, Nov 2007.

[17] T. Ishikawa and T. J. Pedley. Diffusion of swimming model micro-organisms in a semi-dilute suspension. *Journal of Fluid Mechanics*, 588:437–462, 2007.

[18] J. O. Kessler and M. Wojciechowski. *Collective dynamics of swimming bacteria. In Bacteria as Multicellular Organisms (eds J. A. Shapiro and M. Dworkin)*. Oxford University Press, 1997.

[19] J. O. Kessler and N. A. Hill. *Complementarity of physics, biiology, and geometry in the dynamics of swimming micro-organisms. In Physics of Biological Systems, from Molecules to Species (eds. H. Flyvbjerg et al.)*. Springer Lecture Notes in Physics, 1997.

[20] N. H. Mendelson, A. Bourque, K. Wilkening, K. R. Anderson, and J. C. Watkins. Organized cell swimming motions in bacillus subtilis colonies: Patterns of short-lived whirls and jets. *Journal of Bacteriology*, 181(2):600–609, 1999.

[21] Ch. Dombrowski, L. Cisneros, S. Chatkaew, R. E. Goldstein, and J. O. Kessler. Self-concentration and large-scale coherence in bacterial dynamics. *Physical Review Letters*, 93(9):098103, Aug 2004.

[22] A. Sokolov, I. S. Aranson, J. O. Kessler, and R. E. Goldstein. Concentration dependence of the collective dynamics of swimming bacteria. *Physical Review Letters*, 98(15):158102, Apr 2007.

[23] X. L. Wu and A. Libchaber. Particle diffusion in a quasi-two-dimensional bacterial bath. *Physical Review Letters*, 84(13):3017–3020, Mar 2000.

[24] T. Ishikawa, M. P. Simmonds, and T. J. Pedley. Hydrodynamic interaction of two swimming model micro-organisms. *Journal of Fluid Mechanics*, 568:119–160, 2006.

[25] T. Ishikawa and T. J. Pedley. Coherent structures in monolayers of swimming particles. *Physical Review Letters*, 100(8):088103, Feb 2008.

[26] T. Ishikawa, J. T. Locesi, and T. J. Pedley. Development of coherent structures in concentrated suspensions of swimming model micro-organisms. *Journal of Fluid Mechanics*, 615:401–431, 2008.

[27] G. Subramanian and D. L. Koch. Critical bacterial concentration for the onset of collective swimming. *Journal of Fluid Mechanics*, 632:359–400, 2009.

[28] V. Mehandia and P. R. Nott. The collective dynamics of self-propelled particles. *Journal of Fluid Mechanics*, 595:239–264, 2008.

[29] M. M. Hopkins and L. J. Fauci. A computational model of the collective fluid dynamics of motile micro-organisms. *Journal of Fluid Mechanics*, 455:149–174, 2002.

[30] J. P. Hernandez-Ortiz, Ch. G. Stoltz, and M. D. Graham. Transport and collective dynamics in suspensions of confined swimming particles. *Physical Review Letters*, 95(20):204501, Nov 2005.

[31] P. T. Underhill, J. P. Hernandez-Ortiz, and M. D. Graham. Diffusion and spatial correlations in suspensions of swimming particles. *Physical Review Letters*, 100(24):248101, Jun 2008.

[32] L. Cisneros, R. Cortez, Ch. Dombrowski, R. E. Goldstein, and J. O. Kessler. Fluid dynamics of self-propelled micro-organisms, from individuals to concentrated populations. *Experiments in Fluids*, 43(5):737–753, 11 2007.

[33] D. Saintillan and M. J. Shelley. Orientational order and instabilities in suspensions of self-locomoting rods. *Physical Review Letters*, 99(5):058102, Jul 2007.

[34] R. A. Simha and S. Ramaswamy. Hydrodynamic fluctuations and instabilities in ordered suspensions of self-propelled particles. *Physical Review Letters*, 89(5):058101, Jul 2002.

[35] J. Toner, Y. Tu, and S. Ramaswamy. Hydrodynamics and phases of flocks. *Annals of Physics*, 318(1):170–244, 2005. Special Issue.

[36] A. Czirók, A. Barabási, and T. Vicsek. Collective motion of self-propelled particles: kinetic phase transition in one dimension. *Physical Review Letters*, 82(1):209–212, Jan 1999.

[37] S. Sankararaman and S. Ramaswamy. Instabilities and waves in thin films of living fluids. *Physical Review Letters*, 102(11):118107, Mar 2009.

[38] D. Saintillan and M. J. Shelley. Instabilities and pattern formation in active particle suspensions: Kinetic theory and continuum simulations. *Physical Review Letters*, 100(17):178103, Apr 2008.

[39] D. Saintillan and M. J. Shelley. Instabilities, pattern formation, and mixing in active suspensions. *Physics of Fluids*, 20(12):123304, 2008.

[40] D. L. Koch and E. S. G. Shaqfeh. The instability of a dispersion of sedimenting spheroids. *Journal of Fluid Mechanics*, 209:521–542, 1989.

[41] D. Saintillan, E. S. G. Shaqfeh, and E. Darve. The effect of stratification on the wave number selection in the instability of sedimenting spheroids. *Physics of Fluids*, 18(12):121503, 2006.

[42] Ch. Hohenegger and M. J. Shelley. Stability of active suspensions. *Physical Review E*, 81(4):046311, Apr 2010.

[43] Y. Hatwalne, S. Ramaswamy, M. Rao, and R. A. Simha. Rheology of active-particle suspensions. *Physical Review Letters*, 92(11):118101, Mar 2004.

[44] T. Ishikawa and T. J. Pedley. The rheology of a semi-dilute suspension of swimming model micro-organisms. *Journal of Fluid Mechanics*, 588:399–435, 2007.

[45] L. Berlyand B. M. Haines, I. S. Aranson and D. A. Karpeev. Effective viscosity of dilute bacterial suspensions: a two-dimensional model. *Physical Biology*, 5(4):046003, 2008.

[46] D. Saintillan. The dilute rheology of swimming suspensions: A simple kinetic model. *Experimental Mechanics*, to be published in a special issue on Locomotion, Online First 2009.

[47] D. Saintillan. Extensional rheology of active suspensions. *Physical Review E*, 81(5):056307, May 2010.

[48] J. M. Wallace. Twenty years of experimental and direct numerical simulation access to the velocity gradient tensor: What have we learned about turbulence? *Physics of Fluids*, 21(2):021301, 2009.

[49] M. M. Rogers and P. Moin. The structure of the vorticity field in homogeneous turbulent flows. *Journal of Fluid Mechanics*, 176:33–66, 1987.

[50] W. T. Ashurst, A. R. Kerstein, R. M. Kerr, and C. H. Gibson. Alignment of vorticity and scalar gradient with strain rate in simulated Navier–Stokes turbulence. *Physics of Fluids*, 30(8):2343–2353, 1987.

[51] J. Jimenez. Kinematic alignment effects in turbulent flows. *Physics of Fluids A: Fluid Dynamics*, 4(4):652–654, 1992.

[52] M. Doi and S. F. Edwards. *The Theory of Polymer Dynamics*. Oxford University Press, New York, 1986.

[53] F. P. Bretherton. The motion of rigid particles in a shear flow at low Reynolds number. *Journal of Fluid Mechanics*, 14(02):284–304, 1962.

[54] E. J. Hinch and L. G. Leal. Constitutive equations in suspension mechanics. Part 2. Approximate forms for a suspension of rigid particles affected by Brownian rotations. *Journal of Fluid Mechanics*, 76(01):187–208, 1976.

[55] G. B. Jeffery. The motion of ellipsoidal particles immersed in a viscous fluid. *Proceedings of the Royal Society of London. Series A*, 102(715):161–179, 1922.

[56] S. B. Chen and L. Jiang. Orientation distribution in a dilute suspension of fibers subject to simple shear flow. *Physics of Fluids*, 11(10):2878–2890, 1999.

[57] S. B. Chen and D. L. Koch. Rheology of dilute suspensions of charged fibers. *Physics of Fluids*, 8(11):2792–2807, 1996.

[58] H. Hasimoto. On the periodic fundamental solutions of the Stokes equations and their application to viscous flow past a cubic array of spheres. *Journal of Fluid Mechanics*, 5(02):317–328, 1959.

[59] B. D. Hoffman and E. S. G. Shaqfeh. The effect of Brownian motion on the stability of sedimenting suspensions of polarizable rods in an electric field. *Journal of Fluid Mechanics*, 624:361–388, 2009.

[60] R. S. Rogallo. Numerical experiments in homogeneous turbulence. *NASA TM*, 176:81315, 1981.

[61] J. Jeong and F. Hussain. On the identification of a vortex. *Journal of Fluid Mechanics*, 285:69–94, 1995.

[62] H. J. Lugt. *The dilemma of defining a vortex. In Recent Developments in Theoretical and Experimental Fluid Mechanics: Compressible and Incompressible Flows. (ed. U. Muller, K. G. Roesner and B. Schmidt)*. Springer, 1979.

[63] J. C. Hunt, A. A. Wray, and P. Moin. Eddies, stream, and convergence zones in turbulent flows. *Center for Turbulence Research Report*, CTR-S88:193, 1988.

[64] M. S. Chong, A. E. Perry, and B. J. Cantwell. A general classification of three-dimensional flow fields. *Physics of Fluids A: Fluid Dynamics*, 2(5):765–777, 1990.

[65] J. Zhou, R. J. Adrian, S. Balachandar, and T. M. Kendall. Mechanisms for generating coherent packets of hairpin vortices in channel flow. *Journal of Fluid Mechanics*, 387:353–396, 1999.

[66] H. M. Blackburn, N. N. Mansour, and B. J. Cantwell. Topology of fine-scale motions in turbulent channel flow. *Journal of Fluid Mechanics*, 310:269–292, 1996.

[67] J. M. Chacin and B. J. Cantwell. Dynamics of a low Reynolds number turbulent boundary layer. *Journal of Fluid Mechanics*, 404:87–115, 2000.

[68] P. Chakraborty, S. Balachandar, and R. J. Adrian. On the relationships between local vortex identification schemes. *Journal of Fluid Mechanics*, 535:189–214, 2005.

[69] J. H. Irving and J. G. Kirkwood. The statistical mechanical theory of transport processes. IV. The equations of hydrodynamics. *Journal of Chemical Physics*, 18(6):817–829, 1950.

[70] G. K. Batchelor. The stress generated in a non-dilute suspension of elongated particles by pure straining motion. *Journal of Fluid Mechanics*, 46(04):813–829, 1971.

[71] G. K. Batchelor. Transport properties of two-phase materials with random structure. *Annual Review of Fluid Mechanics*, 6(1):227–255, 1974.

[72] D. T. N. Chen, A. W. C. Lau, L. A. Hough, M. F. Islam, M. Goulian, T. C. Lubensky, and A. G. Yodh. Fluctuations and rheology in active bacterial suspensions. *Physical Review Letters*, 99(14):148302, Oct 2007.

[73] A. Sokolov and I. S. Aranson. Reduction of viscosity in suspension of swimming bacteria. *Physical Review Letters*, 103(14):148101, Sep 2009.

[74] B. M. Haines, A. Sokolov, I. S. Aranson, L. Berlyand, and D. A. Karpeev. Three-dimensional model for the effective viscosity of bacterial suspensions. *Physical Review E*, 80(4):041922, Oct 2009.

[75] E. J. Hinch and L. G. Leal. Constitutive equations in suspension mechanics. Part 1. General formulation. *Journal of Fluid Mechanics*, 71(03):481–495, 1975.

[76] L. D. Landau and E. M. Lifshitz. *Fluid Mechanics*. Butterworth-Heinemann, Oxford, 1987.